Institute of Thermoelectricity, Academy of Sciences and Ministry of Education and Science of Ukraine

Journal of THERMOELECTRICITY

International Research

Founded in December, 1993

published 6 times a year

No. 6 *2015*

Editorial Board

International Editorial Board

Founders – National Academy of Sciences, Ukraine
Institute of Thermoelectricity of National Academy of Sciences and Ministry of Education and Science of Ukraine

Certificate of state registration № КВ 15496-4068 ПР

Editorial office manager O. Pugantseva

Approved for printing by the Academic Council of Institute of Thermoelectricity of the National Academy of Sciences and Ministry of Education and Science, Ukraine

Address of editorial office:
Ukraine, 58002, Chernivtsi, General Post Office, P.O. Box 86.
Phone: +(380-372) 90 31 65.
Fax: +(380-3722) 4 19 17.
E-mail: jt@inst.cv.ua
http://www.jt.inst.cv.ua

Signed for publication 25.01.16. Format 70×108/16. Offset paper №1. Offset printing.
Printer's sheet 11.5. Publisher's signature 9.2. Circulation 400 copies. Order 5.

Printed from the layout original made by "Journal of Thermoelectricity" editorial board in the printing house of "Bukrek" publishers,
10, Radischev Str., Chernivtsi, 58000, Ukraine

CONTENTS

Vikhor L.M.

L.M.Vikhor, P.V.Gorskyi.

Institute of Thermoelectricity of the NAS and MES
of Ukraine, 1 Nauky str., Chernivtsi,
58029, Ukraine

Gorskyi P.V.

HEAT AND CHARGE TRANSPORT AT "THERMOELECTRIC MATERIAL-METAL" BOUNDARY

A physical model of heat and electric charge transport at pthermoelectric material-metal boundary is considered that takes into account phonon reflection at the boundary and the impact of potential barrier on charge carrier motion through the boundary. The methods for calculation of the boundary thermal and electric resistances and thermopower in conformity with said model are described. The values of these resistances and the Seebeck coefficient at the boundary between Bi – Te materials and Cu or Ni metals are evaluated and their temperature dependences are determined. It is shown that the boundary thermal resistance reaches the value of 10^{-8} K/W·m^2, the electric resistance is at a level of $5 \cdot 10^{-11}$ Ω·m^2, and the boundary thermopower due to emission is about 500 μV/K. Caused by the above resistances, the thermal and electric losses at thermoelectric material-metal boundary can have a considerable impact on the parameters of microminiature power converters.

Key words: boundary thermal resistance, boundary electric resistance, boundary thermopower.

Introduction

Nowadays, widespread application of thermoelectricity is essentially constrained by high power conversion unit costs. The main contributor to the cost of thermocouple converters is thermoelectric material (TEM). The specific feature of thermoelectric power conversion is independence of its maximum efficiency of hermocouple gometry. Therefore, ideally, microminiaturization might achieve cost reduction without performance degradation.

However, a major microminiaturization problem lies in growing impact of thermal and electric losses in the zone of contact between semiconductor material of thermocouple legs and metal interconnect electrodes. These losses are caused by thermal and electric resistances of transient contact layer formed between TEM and metal at interconnection of legs. Under conditions of microminiaturization the thickness of contact layer becomes commensurate with the leg height, and thermal and electric contact resistances – with the respective leg resistances. In so doing, the impact of losses in the contact layer is increased, and the efficiency of thermoelectric converter is reduced [1, 2].

Modern technologies of creating micromodules by embedding, sputtering or chemical deposition of film electrodes with anti-diffusion microlayers on the end surface of leg [3] permit to minimize contact layer thickness and obtain virtually "perfect" (without a transient layer) TEM – metal boundary. However, a drastic difference in the physical properties of semiconductor and metal affects the motion of charge carriers and phonons through TEM – metal boundary, which defines the thermal and electric resistance and thermopower of such a "perfect" boundary [4 – 6].

To determine the values of the boundary resistances and thermopower is a relevant and important task in the design of micromodule thermoelectric power converters [6, 7].

Therefore, *the purpose* of this paper is to estimate the values of thermal and electric resistances and thermopower, to determine their temperature dependences for the boundaries between conventional *Bi – Te* based thermoelectric materials and metal interconnect electrodes for their further use in the design of thermoelectric microconverters of energy.

Physical model of heat and electric charge transport at TEM-metal boundary

Fig.1 illustrates a physical model of heat and electric charge transport by phonons and charge carriers at TEM-metal boundary.

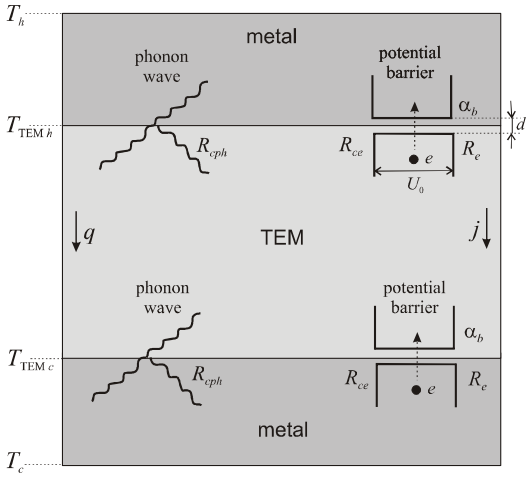

Fig. 1. Physical model of heat and charge carrier transport at TEM-metal boundary.

A perfect boundary is characterized by the mismatch of semiconductor and metal physical properties, which causes thermal and electric resistance to motion of phonons and charge carriers through the boundary.

Phonon wave carrying thermal flux partially passes through the boundary and partially is reflected. Phonon reflection is the reason for phonon component of the boundary thermal resistance R_{cph} [8, 9].

Motion of charge carriers through the boundary is prevented by potential barrier formed due to the difference in the band structures of semiconductor and metal [5]. This barrier is the reason for resistance to heat transport by carriers moving through the boundary, i.e. the electron component of thermal resistance R_{ce}.

R_{cph} and R_{ce} are the main components of the boundary thermal impedance R_c defined as follows:

$$\frac{1}{R_c} = \frac{1}{R_{c\,ph}} + \frac{1}{R_{ce}}. \qquad (1)$$

Charge carrier transport through TEM-metal boundary is accompanied by the origination of electrical boundary resistance R_e caused by their passing through potential barrier. The value of R_e depends on the barrier characteristics, i.e. its height U_0, width d and shape, as well the mechanism (tunneling or emission) of charge carrier passage through the barrier.

Potential barrier also gives rise to origination of the boundary thermopower which is characterized by the boundary coefficient [5] α_b. Note that α_b is not the difference in the Seebeck coefficients of adjacent materials.

Calculation of phonon component of the boundary thermal resistance

Thermoelectric material and metal are essentially different in sound velocities, phonon densities of states, the Debye temperatures and frequencies. A mismatch of these properties creates a resistance to phonon flux through the boundary. To estimate the value of phonon component of the boundary thermal resistance $R_{cph,}$ two models are employed [10]. The first one is called acoustic mismatch model (AMM) [11]. The main approximation of AMM is that the boundary is considered to be "absolutely flat" and phonons are reflected from it in a mirror-like fashion, i.e. there is no phonon scattering at the boundary. The second, the so-called diffuse mismatch model (DMM) [9, 10] takes into account diffuse phonon scattering on the irregularities and defects of the boundary.

The assumption that phonons are not scattered is valid only on condition of rather low temperatures whereby phonon wavelength λ is much in excess of dimension b characterizing the roughness of the boundary or its deviation from the ideal flatness. Thus, for the AMM model $\lambda/b << 1$, and for the DMM model $\lambda/b \geq 1$ [10].

The wavelength λ can be approximately estimated by the formula [12]

$$\lambda \approx \frac{\theta_D}{T} a \,, \tag{2}$$

where θ_D is the Debye temperature, a is the averaged value of the size of crystal lattice unit cell.

For thermoelectric materials based on $Bi-Te$ $\theta_D \sim 160$ K, $a \sim 20$ Å [13, 14]. Hence, for standard operating temperature ranges of thermoelements $T = 200 \div 300$ K the acoustic wavelength $\lambda = 1 \div 2$nm. Thus, for the applicability of the AMM model the roughness of the boundary should be much lower than 1 – 2nm, which is scarcely probable. Therefore, to estimate the phonon component of thermal resistance R_{cph} of TEM – metal boundary, it is generally reasonable to use the DMM model.

A method of calculation of R_{cph} in conformity with DMM is detailed in [10]. According to the results of this work it can be written:

$$R_{c\,ph} = \frac{\Delta T}{q} \,, \tag{3}$$

where $\Delta T = T_{TEM} - T_m$, T_{TEM}, T_m are the temperatures of TEM and metal, respectively. Heat flux q passing through TEM-metal boundary is related to velocities u_j of the j – th mode phonons and density-of-states function $g(\omega)$ of phonons with frequency ω by the following relationship [10, 6]:

$$q = \frac{\hbar}{4}\tau \sum_j u_{TEM,j} \int_0^\infty g(\omega)\omega \left[\frac{1}{\exp(\frac{\hbar\omega}{kT_{TEM}}) - 1} - \frac{1}{\exp(\frac{\hbar\omega}{kT_m}) - 1} \right] d\omega \,, \tag{4}$$

where k is the Boltzmann constant. Phonon transmission coefficient τ is determined as follows:

$$\tau = \frac{\sum_j u_{m,j}^{-2}}{\sum_j u_{TEM,j}^{-2} + \sum_j u_{m,j}^{-2}} \,. \tag{5}$$

Formula (5) was obtained in [10] in the approximation of $\Delta T \to 0$. In [10] it was shown that there are practically no deviations in the values of R_{cph} determined at different ΔT by formula (3), on condition of $\Delta T < 10$ K. Therefore, for calculations, R_{cph} are restricted by $\Delta T = 1$ K.

The next approximation is related to determination of phonon velocity in thermoelectric material. Due to the absence of information on the velocities of longitudinal and two transverse phonon modes in *Bi – Te* based materials, an assumption is made that these two velocities are equal [6], i.e.:

$$\sum_j u_{TEM,j}^{-2} = \frac{3}{u_{TEM}^2}. \tag{6}$$

In so doing, u_{TEM} is determined by the formula relating phonon velocity to the Debye temperature:

$$\frac{kT_D}{\hbar} = (6\pi^2 u_{TEM}^3 n)^{1/3}, \tag{7}$$

where n is the number of crystal lattice unit cells per unit volume.

For the calculation of q by formula (4) one can use the experimental density-of-states function $g(\omega)$, determined for a series of *Bi – Te* based compounds [15] or take it in the Debye approximation, i.e. in the form:

$$g_D(\omega) = \frac{\omega^2}{2\pi^2 u_{TEM}^3}. \tag{8}$$

Note that in the latter case integration in (4) is done to maximum possible value of phonon frequency, i.e. to the Debye frequency $\omega_D = kT_D/\hbar$. In [6] it is shown that the values of phonon component of resistance at TEM-metal boundary determined with the use of experimental density-of-states function and the Debye density-of-states function actually coincide.

Hence, using the ratios (3) – (8), one can determine pretty exactly the value of phonon component of TEM-metal boundary thermal resistance.

The electron component of the boundary thermal resistance, electric resistance and thermopower

As mentioned above, potential barrier accounts for the electron component of the boundary thermal resistance R_{ce} and electric boundary resistance R_e, as well as the boundary thermopower α_b. The method for calculation of these boundary impedances is proposed in [4, 5, 16]. It is based on the analogy of description of heat and electric charge transport through potential barrier and in the bulk of TEM itself.

Potential barrier at the boundary is considered to be a rectangle of height U_0 and width d. Charge carriers can overcome it by tunneling or electron emission. Maximum value of barrier width d whereby tunneling is possible is set by inequality

$$\Lambda kT \le 1, \tag{9}$$

where $\Lambda = 1/\sqrt{E_d U_0}$, $E_d = \hbar^2/2md^2$, m is electron mass in TEM. For wider barriers the mechanism of emission is involved.

The ratios for boundary impedances in case of tunnelling were obtained in [4, 5, 16]. The electric boundary resistance R_e is determined by the formula

$$\frac{1}{R_e} = \frac{e^2 mP}{2\pi^2 \Lambda \hbar^3}, \tag{10}$$

where P is probability of tunneling through the barrier, calculated as follows [17]:

$$P = \left\{1 + \frac{U_0^2 \sin h^2 [2m(U_0 - E)d^2/\hbar^2]^{1/2}}{4E(U_0 - E)}\right\}^{-1}, \tag{11}$$

where E is the energy of carriers and $E < U_0$. As a rule, one selects $E = U_0/2$.

The electron component of thermal boundary resistance R_{ce} is related to the electric resistance R_e by the Wiedemann-Franz law [16]:

$$\frac{1}{R_{ce}} = \frac{\pi^2}{3}\frac{T}{R_e}\left(\frac{k}{e}\right)^2. \tag{12}$$

The boundary Seebeck coefficient is equal to:

$$\alpha_b = \left(\frac{k}{e}\right)\frac{\pi^2}{3}\Lambda kT. \tag{13}$$

In case of emission, the impedances are determined using expressions [5, 18].

$$\frac{1}{R_e} = \frac{e}{k} AT \exp(-U_0/kT), \tag{14}$$

$$\frac{1}{R_{ce}} = 2\frac{T}{R_e}\left(\frac{k}{e}\right)^2, \tag{15}$$

$$\alpha_b = \frac{1}{eT}(U_0 + 2kT), \tag{16}$$

where $A = \dfrac{emk^2}{2\pi^2\hbar^3}$ is the Richardson constant for TEM.

In order to determine whether tunneling or emission take place in a specific case, one should know barrier characteristics, namely height U_0 and width d. In [19], the estimate for metal-semiconductor barrier heights $U_0 \le 0.1$ eV was obtained. For impedance calculation it is reasonable to use maximum value of barrier height $U_0 = 0.1$ eV, as it is accepted in [6]. Barrier width is estimated from the formula [17]:

$$d = \frac{1}{2}\left(\frac{2\varepsilon\varepsilon_0 U_0}{eN}\right)^{1/2}, \tag{17}$$

where ε is dielectric permittivity of TEM, ε_0 is dielectric constant, N is charge carrier concentration in TEM.

Thus, the ratios (10) – (17) are used to estimate the values of boundary impedances characterizing charge carrier motion through potential barrier.

Results of calculation of the resistances and thermopower at TEM – metal boundary

The values of thermal and electric resistances and thermopower were estimated for the boundaries between *n*-type $Bi_2Te_{2.7}Se_{0.3}$ and p-type $Bi_{0.5}Sb_{01.5}Te_3$ conventional thermoelectric materials and metal connecting electrodes of *Cu* or *Ni*. Parameters of TEM and metals necessary for the calculations are listed in Table 1.

Table 1

Parameters of TEM and metals

Parameter	TEM		References
	$Bi_2Te_{2.7}Se_{0.3}$ *n*-type	$Bi_{0.5}\,Sb_{01.5}Te_3$ *p*-type	
Charge carrier concentration N, m^{-3}	$3\cdot10^{25}$	$2\cdot10^{25}$	[22]
Charge carrier mass m (m_0 electron mass)	$1.25m_0$	$0.6m_0$	[13, 22]
Parameters of crystal lattice hexagonal cell a, Å c, Å	 4.35 30.2	 4.3 30.5	[14]
Debye temperature T_D, K	157	159	
Dielectric permittivity ε, $K^2/J\cdot m$	98	62	
	Metal		
	Cu	*Ni*	
Phonon velocities $\kappa_{\parallel}$, m/s $u_{\perp}$, m/s	 4760 2325	 5630 2960	[23]

The Debye temperatures (Table 1) of $0.9Bi_2Te_3 + 0.1Bi_2Se_{0.3}Se_3$ and $0.25Bi_2Te_3 + 0.75Sb_2Te_3$ solid solutions were determined by the formula:

$$T_D = \left(\frac{x_1}{T_{D1}^3} + \frac{x_2}{T_{D2}^3} \right)^{-1/3}, \qquad (18)$$

where x_i, T_{Di} is molar content and the Debye temperature of solution components (Table 2), respectively.

The dielectric permittivity of solid solutions ε was calculated by the formula:

$$\frac{\varepsilon - 1}{\varepsilon + 2} = \sum_{i=1}^{2} x_i \frac{\varepsilon_i - 1}{\varepsilon_i + 2}, \qquad (19)$$

where ε_i is the dielectric permittivity of components (Table 2).

Table 2

Parameters of components of *Bi – Te* based solid solutions

Параметр	Bi_2Te_3	Sb_2Te_3	Bi_2Se_3	Ссылки
Debye temperature T_{Di}, K	155.5	160	180	[13]
Dielectric permittivity ε_i, $K^2/J\cdot m$	100	55	80	[6.24]

Formulae (18) and (19) have been derived on the basis of formula for heat capacity of solids at low temperatures and the Clausius-Mossotti formula cited in [20].

The calculated properties of TEM necessary for estimation of thermal and electric boundary resistances are given in Table 3.

Table 3

Calculated TEM properties

Parameter	$Bi_2Te_{2.7}Se_{0.3}$ *n*-type	$Bi_{0.5}Sb_{01.5}Te_3$ *p*-type
Debye frequency ω_D, rad/s	$2.06\cdot10^{13}$	$2.08\cdot10^{13}$
Number of unit cells per unit volume n, m^{-3}	$6.1\cdot10^{27}$	$6.14\cdot10^{27}$
Phonon velocity u_{TEM}, m/s	$2.9\cdot10^{3}$	$2.91\cdot10^{3}$
Phonon transmission coefficient $\tau_{TEM\to Cu}$ $\tau_{TEM\to Ni}$	 0.537 0.421	 0.539 0.424
Potential barrier width d, nm	3.0	2.93
Λ, J^{-1}	$3.39\cdot10^{20}$	$2.29\cdot10^{20}$
$\Lambda\cdot kT$	1.4	0.95

From the data of Table 3 it follows that tunneling condition (9) for charge carriers is not met. Therefore, ultimate impedances were determined for the emission model of potential barrier. The results of calculation of phonon and electron components and thermal boundary impedance at T = 300K are presented in Table 4.

Table 4

Design values of thermal resistance of TEM – metal boundaries at T = 300K

Boundary	n-$Bi_2Te_{2.7}Se_{0.3}$/Cu	n-$Bi_2Te_{2.7}Se_{0.3}$/Ni	p-$Bi_{0.5}Sb_{01.5}Te_3$/Cu	p-$Bi_{0.5}Sb_{01.5}Te_3$/Ni
Phonon component $R_{c\,ph}$, $K\cdot m^2/W$	$1.04\cdot10^{-8}$	$1.32\cdot10^{-8}$	$1.01\cdot10^{-8}$	$1.29\cdot10^{-8}$
Electron component $R_{c\,e}$, $K\cdot m^2/W$	$0.21\cdot10^{-5}$	$0.21\cdot10^{-5}$	$0.43\cdot10^{-5}$	$0.43\cdot10^{-5}$
Thermal impedance R_c, $K\cdot m^2/W$	$1.03\cdot10^{-8}$	$1.31\cdot10^{-8}$	$1.01\cdot10^{-8}$	$1.29\cdot10^{-8}$

The temperature dependences of these resistances are shown in Figs. 2 – 5.

From the obtained data it follows that electron component which is essentially temperature dependent (Fig. 3) has little effect on thermal resistance value. As a result, thermal boundary resistance is practically independent of temperature (Fig. 4). The value of thermal resistance at TEM – copper boundary reaches the values close to 10^{-8} K·m^2/W, and at nickel boundary – $1.3 \cdot 10^{-8}$ K·m^2/W.

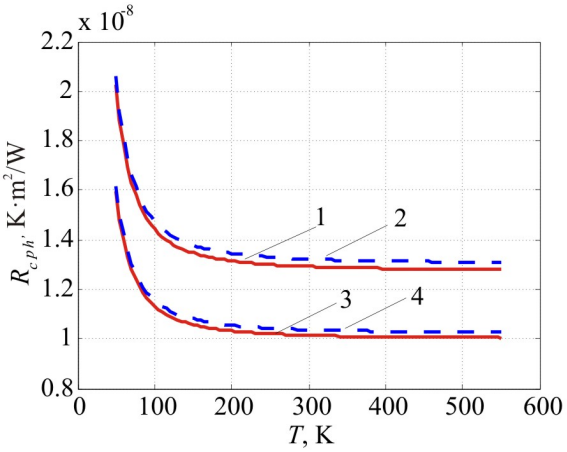

Fig. 2. Temperature dependences of the phonon component of thermal resistance at the boundaries: 1 – p-$Bi_{0.5}Sb_{1.5}Te_3$/Ni, 2 – n-$Bi_2Te_{2.7}Se_{0.3}$/Ni,3 – p-$Bi_{0.5}Sb_{1.5}Te_3$/Cu, 4 – n-$Bi_2Te_{2.7}Se_{0.3}$/Cu.

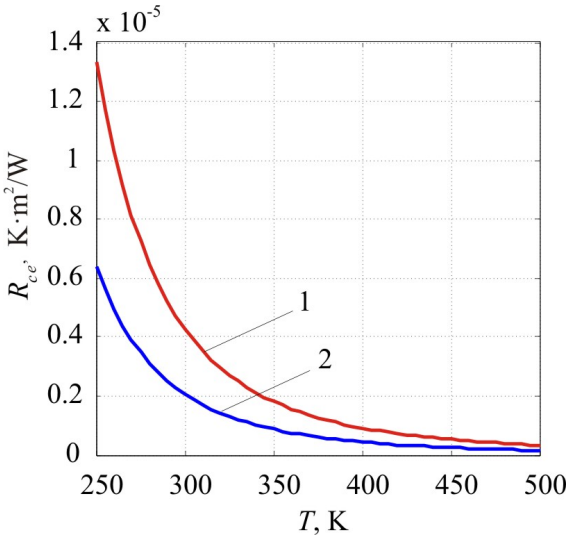

Fig. 3. Temperature dependences of the electron component of thermal resistance at TEM-metal boundaries: 1 – TEM p-$Bi_{0.5}Sb_{1.5}Te_3$, 2 – TEM n-$Bi_2Te_{2.7}Se_{0.3}$.

The calculated temperature dependences of the electric boundary resistance arising due to charge carrier emission are shown in Fig. 5. This resistance does not exceed the value of $5 \cdot 10^{-11}$ Ω·m^2, which is an order lower that the resistance of contact layer formed in case of imperfect TEM-metal boundary and, as a rule, is about $10^{-9} \div 5 \cdot 10^{-10}$ Ω·m^2 [1, 2, 21].

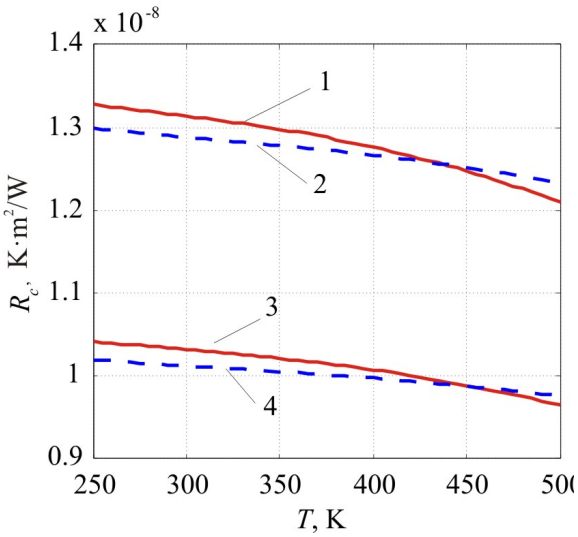

Fig.4. Temperature dependences of the thermal resistance at the boundaries:1 – n-$Bi_2Te_{2.7}Se_{0.3}$/Ni, 2 – p-$Bi_{0.5}Sb_{1.5}Te_3$/Ni, 3 – n-$Bi_2Te_{2.7}Se_{0.3}$/Cu, 4 – p-$Bi_{0.5}Sb_{1.5}Te_3$/Cu.

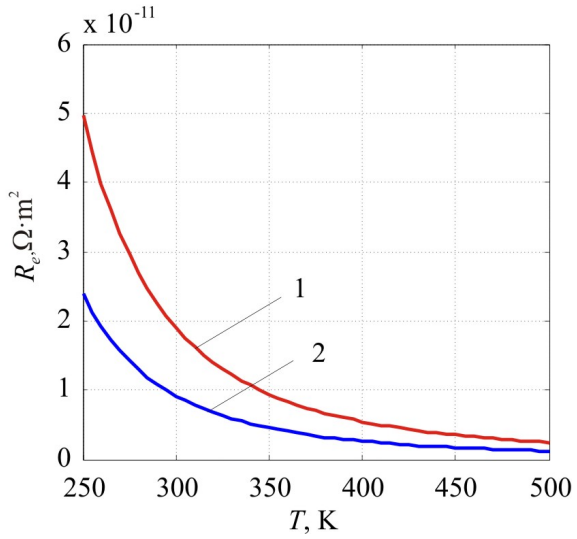

Fig. 5. Temperature dependences of the electric resistance at TEM-metal boundaries: 1– p-$Bi_{0.5}Sb_{1.5}Te_3$ TEM; 2 – n-$Bi_2Te_{2.7}Se_{0.3}$.TEM.

Apparently, such value of electric boundary resistance in thermoelements can affect the efficiency factors of microminiature modules for coolers and generators.

Temperature dependence of the boundary Seebeck coefficient $|\alpha_b|$ is shown in Fig. 6.

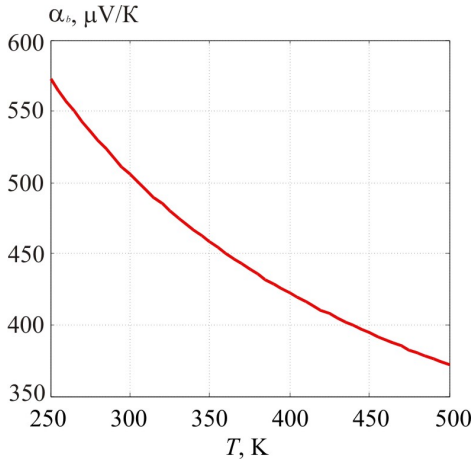

Fig.6. Temperature dependence of electron emission thermopower at TEM-metal boundary.

Note that under conditions of validity of the barrier emission model, the absolute value of the Seebeck coefficient for *n*- or *p*-type TEM – metal boundaries is the same and reaches the value of $|\alpha_b| \approx 500$ μV/K at $T = 300$ K. In [6] it is shown that for *n*-type TEM – metal boundaries α_b should be considered to be positive, and for *p*-type TEM – metal boundaries – negative.

By definition, the Seebeck coefficient of thermoelectric leg (Fig. 1) is determined as follows:

$$\alpha = \frac{\Delta\varphi}{T_h - T_c}, \tag{20}$$

where $\Delta\varphi$ is potential difference between the hot and cold sides of the leg taking into account the Seebeck effect in material of the leg itself and the thermopower of the boundaries, i.e.:

$$\Delta\varphi = \alpha_b(T_h - T_{TEM\,h}) + \alpha_{TEM}(T_{TEM\,h} - T_{TEM\,c}) + \alpha_b(T_{TEM\,c} - T_c), \tag{21}$$

where α_{TEM} is the Seebeck coefficient of TEM. Then, according to (20), we obtain:

$$\alpha = \alpha_b + (\alpha_{TEM} - \alpha_b)\frac{T_{TEM\,h} - T_{TEM\,c}}{T_h - T_c}, \tag{22}$$

From (22) it follows that $\alpha \approx \alpha_{TEM}$, as long as $T_{TEM\,h} - T_{TEM\,c} \approx T_h - T_c$. Thus, the thermopower of TEM-metal boundary has no essential impact on the thermoelement efficiency.

Conclusions

1. The methods of calculation of thermal and electric resistances and thermopower arising under heat and charge transport through TEM – metal boundary are considered. The values of thermal and electric resistances and thermopower at the boundaries between *n*-type $Bi_2Te_{2.7}Se_{0.3}$ and *p*-type $Bi_{0.5}Sb_{01.5}Te_3$ materials and *Cu* or *Ni* metals are evaluated.
2. It is established that thermal boundary resistance is about 10^{-8}K/W·m^2 and depends only slightly on temperature.

3. The electric boundary resistance is due to charge carrier emission through the boundary and its values are of the order of $5 \cdot 10^{-11}$ $\Omega \cdot m^2$.
4. It is shown that the boundary thermopower value due to emission is about 500 μV/K.

References

1. L.I.Anatychuk, R.V.Kuz, The Energy and Economic Parameters of *Bi – Te* Based Thermoelectric Generator Modules for Waste Heat Recovery, *J.Thermoelectricity* 4, 75 – 82 (2012).
2. J.-P. Fleurial, A. Borshchevsky, M.A.Ryan, W.Phillips, E.Kolawa, T. Kacisch, and R.Ewell, Thermoelectric Microcoolers for Thermal Management Applications, *Proceedings of the 16th International Conference on Thermoelectrics* (Dresden, Germany, August, IEEE, Piscataway, NJ, 1997), P. 641 – 645.
3. Harald Bottner, Joachim Nurnus, Axel Schubert, Miniaturized Thermoelectric Converters, in: *Thermoelectrics Handbook, Macro to Nano., Edited by D.M. Rowe, CRC Taylor & Francis, 2006, P.46-1 – 46 – 18.*
4. M.Bartkowiak, G.D.Mahan, Boundary Effects in Thin-Film Thermoelectrics, *Proc. of Mat. Res. Soc. Symp., 545, 1999, P.265 – 272.*
5. M.Bartkowiak, G.D.Mahan, Heat and Electricity Transport Through Interfaces, in: *Recent Trends in Thermoelectric Materials, vol. II, Semiconductors and Semimetals*, vol. 70 (Academic Press, New York, 2001), P. 245 – 271.
6. L.W.Da Silva, M.Kaviany, Microthermoelectric Cooler: Interfacial Effects on Thermal and Electrical Transport, *International Journal of Heat and Mass Transfer* **47**(10 – 11), 2417 – 2435 (2004).
7. Kong Hoon Lee, Hyunsen Kim, Ook Joong Kim, Effect of Thermoelectric and Electrical Properties on the Cooling Performance of a Micro Thermoelectric Cooler, *J.Electronic Materials* **39**(9), 1566 – 1571 (2010).
8. R.E.Peterson, A.C.Anderson, The Kapitza Thermal Boundary Resistance, *J. Low Temp. Phys*. 11, 639 – 644 (1973).
9. E.T.Swartz, R.O.Pohl, Thermal Boundary Resistance, *Rev. Mod. Phys*. **61**(3), 605 – 658 (1989).
10. P.E.Phelan, Application of Diffuse Mismatch Theory to the Prediction of Thermal Boundary Resistance in Thin-Film High-T_c Superconductors, *ASME J. Heat Transfer* 120, 37 – 43 (1998).
11. W.A.Little, The Transport of Heat between Dissimilar Solids at Low Temperatures, *Canadian J. of Phys.* 37, 334 – 339 (1959).
12. J.M.Rosenberg, *The Solid State* (3-rd ed. Oxford University Press, NY, 1988).
13. *CRC Handbook of Thermoelectrics*, edited by D.M.Rowe, CRC Press, London, New York, 1995.
14. B.M.Goltsman, V.A.Kudinov, and I.A.Smirnov, *Semiconductor Thermoelectric Materials Based on Bi_2Te_3.* (Moscow: Nauka, 1972), 320 p.
15. H.Rauh, R.Geick, H.Kohler, N.Nucker, and N.Lehner, Generalized Phonon Density of States of the Layer Compounds Bi_2Se_3, Bi_2Te_3, Sb_2Te_3 and $Bi_2(Te_{0:5}Se_{0:5})_3$, $(Bi_{0:5}Sb_{0:5})_2Te_3$, *Solid State Phys*. 14, 2705 – 2712 (1981).
16. G.D.Mahan, M.Bartkowiak, Wiedemann-Franz Law at Boundaries, *Appl. Phys. Lett*. 80, 4016 – 4020 (1998).
17. S.M.Sze, *Semiconductor Devices - Physics and Technology* (John Wiley & Sons, 1985).
18. G.D.Mahan, J.O.Sofo, and M.Bartkowiak, Multilayer Thermionic Refrigerator and Generator, *J. Appl. Phys*. 83, 4683 – 4690 (1998).

19. G.D.Mahan, L.M.Woods, Multilayer Thermionic Refrigeration, Phys. Rev. Lett. **80**(18), 4016–4019 (1998).
20. Ch.Kittel, *Introduction to Solid State Physics* (Moscow: Nat.Publ.Phys.-Mat.Lit., 1963), 696 p.
21. L.I.Anatychuk, L.M.Vikhor, Computer Design of Staged Generator Modules, *J.Thermoelectricity* 4, 19 – 27 (2002).
22. A.S.Okhotin, A.A.Yefremov, V.S.Okhotin, and A.S.Pushkarsky, *Thermoelectric Generators, Ed. by A.R.Regel* (Moscow: Atomizdat, 1971), 288 p.
23. *Physical Quantities, Reference Book*, Ed. by I.S.Grigoryev, E.Z.Meylikhov, (Moscow: Energoatomizdat, 1991), 1231 p.
24. O.Madelung, U.Rossler, and M.Schulz (ed.), *Springer Materials — The Landolt-Bornstein Database (http://www.springermaterials.com).*

Submitted 10.07.2015

Alim Ormeci and Yuri Grin

Max-Planck Institut für Chemische Physik fester Stoffe,
Nöthnitzer Str. 40, 01187 Dresden, Germany

COEXISTENCE OF IONIC AND COVALENT ATOMIC INTERACTIONS (BONDING INHOMOGENEITY) AND THERMOELECTRIC PROPERTIES OF INTERMETALLIC CLATHRATES

The influence of atomic interactions on the thermoelectric behavior of the Ba - Ge-based ternary clathrate-I phases $Ba_8T_xGe_{46-x-y}\square_y$ (T – main group element or late transition metal) has been investigated by means of quantum chemical techniques. The atomic interactions changes with the substituting element T were studied in real space by employing the electron localizability approach. Essentially two-center bonds in the framework (Ge – Ge and Ge – T) and predominantly ionic bonds between the guest and framework atoms were found. However, for T = Ag, Cd, Pt and Au, additional two-center Ba - T interactions were discovered. The type-I clathrates with such interactions are reported to have very low lattice thermal conductivity, revealing an important role of atomic interactions in the limiting of the thermal transport.

Key words: intermetallic clathrates, chemical bonding, lattice thermal conductivity, QTAIM, electron localizability approach

Introduction

Inorganic clathrates are an important group of intermetallic cage compounds. After the first report on *Na – Si* based clathrates in 1965 [1], the research activity on inorganic clathrates has steadily increased. Although there are a number of different clathrate structure types, the type-I clathrate phases have attracted most attention due to their relatively simple preparation and variability of chemical composition [2, 3, 4]. In type-I clathrate crystal structure four-coordinated atoms constitute a three-dimensional (3D) host framework with large cages that can accommodate guest atoms. Type-I clathrates crystallize in a simple cubic lattice and have the ideal composition G_8Fw_{46} with 8 guest (*G*) and 46 framework (*Fw*) atoms, Pearson symbol *cP*54. The guest atoms can typically be alkali metals (*Na*, *K*, *Rb*, *Cs*), alkaline earths (*Sr*, *Ba*) or *Eu*. The framework mainly consists of group 14 elements, *Si*, *Ge*, *Sn*, and allows substitutions by other main group p elements or by electronegative transition metals. This flexibility in framework substitutions (which may be accompanied by inserting two elements, *G* and *G'*, as guest atoms) provides invaluable opportunities to tune various physical properties.

Silicon-based clathrate-I phases drew attention when superconductivity was reported in $(Na, Ba)_xSi_{46}$ [5] and $Ba_{8-x}Si_{46}$ [6] with transition temperatures of 4 and 8 K, respectively. Germanium-based clathrate-I phases, on the other hand, have been studied mostly for their potential use in thermoelectric (TE) applications. In general, all clathrate structures with their 3D framework - guest atoms in large cages type of arrangements are promising candidates as thermoelectric materials. This can be understood by considering the requirements for efficient TE performance. The thermoelectric performance of a material is assessed by a dimensionless figure of merit, $ZT = S^2 \sigma T / \kappa$. Here, *S* is the

Seebeck coefficient or thermopower, σ is the electrical conductivity, κ the thermal conductivity and *T* is the absolute temperature. Thermal conductivity has mainly contributions from electrons, κ_e, and from the lattice, κ_L. The former is directly proportional to the electrical conductivity, as described to a good approximation in the low- and high-temperature region through the Wiedemann-Franz law. Since both thermopower and electrical conductivity depend on charge carrier concentration, all terms in the figure of merit expression but the lattice thermal conductivity are determined largely by the charge carrier concentration of the TE material. Hence, increasing *ZT* to high values can be achieved by optimizing the charge carrier concentration. In order to improve the TE performance further, however, the lattice thermal conductivity, κ_L, should be reduced as much as possible. Consequently, the challenge in TE materials research can be summarized as finding a material that has good electronic but poor thermal transport properties. G. Slack introduced the concept of phonon glass electron crystal (PGEC) to describe this challenge [7]. The PGEC concept relies on the approximation that electronic and thermal transport properties of a compound can be modified rather independently of each other. Such a decoupling may be achieved in cage compounds with separated framework and guest substructures, as in clathrates or filled skutterudites, for example [4, 8]. The covalently bonded frameworks in the clathrate compounds are very convenient for purposes of optimizing the electronic part through substitution, while the guest atoms in the cages can impede the heat transport by giving rise to avoided crossings (between the acoustical branches and the guest-atom derived flat optical modes), however the actual mechanism is still debated [9, 10, 11, 12], in particular after inelastic scattering experiments revealing no evidence for an interpretation in terms of an isolated oscillator and showing rather coherent modes of guest and host substructures [10, 13].

The type-I clathrates obtained by substitution in the binary $Ba_8Ge_{43}\Upsilon_3$ are among the most intensely investigated clathrate phases. *ZT* values larger than 1.0 were reported at high temperatures (≥ 900 K) for $Ba_8Ga_{16}Ge_{30}$ (single crystal) [14] and $Ba_8Ni_{0.31}Zn_{0.52}Ga_{13.06}Ge_{32.2}$ [15], while polycrystalline $Ba_8Au_{5.3}Ge_{40.7}$ attains a *ZT* value of 0.9 at 680 K [16]. So far various ternary clathrate-I phases with a general composition $Ba_8T_xGe_{46-x-y}\Upsilon_y$ (where Υ stands for vacancy and *T* for the third element) were studied both experimentally and computationally in order to find compounds suitable for further improvement: *T* = *Ni* [17, 18, 19], *Cu* [17, 20, 21, 22], *Zn* [23, 24, 25, 26, 27], *Rh* [28], *Pd* [17, 29], *Ag* [17, 30], *Cd* [27, 31, 32], *Ir* [33], *Pt* [17, 34] and *Au* [16, 17, 35] as well as *Al* [36] and *Ga* [37, 38]. The homogeneity ranges vary greatly with the substituting element *T,* up to $x \approx 16$ for *Ga* [37], $x \approx 4.2$ for *Ni* [18] and $x \approx 0.4$ for *Ir* [33]. The binary clathrate-I phase in the *Ba* – *Ge* system ($x = 0$) has the composition $Ba_8Ge_{43}\Upsilon_3$ with three framework vacancies [39, 40]. The framework vacancies ($y \neq 0$) are also observed in ternary phases for small values of *x*. This large variation in chemical composition and the substituting elements give rise to a rich spectrum of physical properties. Electrical conductivity can be metallic or semiconducting; transitions from *n*- to *p*-type conduction are reported for the phases with *T* = *Ni* [19] and *Au* [16]; relatively low lattice thermal conductivities were observed for *T* = *Cu*, *Ag*, *Cd*, *Pt* and *Au*. Consequently, understanding the nature of this observed richness in respect of atomic interactions (chemical bonding) is of current interest.

The Zintl – Klemm concept is very useful in understanding the general features of the atomic interactions in clathrates. According to this concept the electropositive elements occupying the guest positions transfer their valence electrons to the framework so that the guest-framework interactions are mainly of ionic nature, and in the framework essentially two center-two electron ($2c – 2e$) covalent bonds are formed. In the case of complete electron balance, the number of available electrons matching the required number for all 92 ($2c – 2e$) framework bonds, a semiconducting behavior is expected. The case of excess electrons (electron deficiency) leads to *n*-type (*p*-type) electrical

conductivity. However, the discovery of covalent interactions between the guest atoms and some of the substitutions (see, for example, reference [16] for *Ba* ← *Au* dative bonds) clearly indicates that quantum mechanics-based analytic tools are needed for a deeper understanding.

The atomic interactions in crystalline solids are usually studied by using quantities expressed in the reciprocal space, such as electron energy dispersions (bands and/or fat bands) and the electronic density of states (DOS). Recently this type of analysis is augmented by a real or direct space analysis, as well [41]. The electron localizability approach allows study of chemical bonding in real space using first-principles quantum mechanical calculations. This concept is in particular successful for intermetallic compounds. The real space analysis based on the electron localizability indicator (ELI [42]) resolves the shell structures of free atoms. Hence, when applied to a molecule or solid the core and valence regions are separated. The core electrons that do not participate in chemical bonding show spherically symmetric ELI distribution. The atomic interactions mostly take place in the valence region, and consequently the ELI distribution in this region is highly structured implying two- or multi-center bonds, or lone-pair-like features. In cases involving transition metal atoms a frequently encountered situation is the participation of the penultimate-shell electrons in chemical bonding which is manifested in the deviation of the ELI distribution in the penultimate shell from spherical symmetry [43, 49].

The electron localizability approach employs the topological analysis methods that play a central role also in the quantum theory of atoms in molecules (QTAIM) [44]. In QTAIM, the local maxima of the electron density usually occur at nuclear sites and the respective basins (QTAIM basins) are recognized as atoms in the crystal structure (molecule). The local ELI maxima, on the other hand, identify the inner electronic shells (core region) and the bonding interactions (valence region). Integrating the electron density inside the corresponding basins yields their electron populations. For the QTAIM or atomic basins the result will be the total number of electrons (Q_A) that an atom A has in the given compound (molecule). For the basins of the ELI, number of core electrons for each atom and/or the electron populations of each bonding basin will be obtained. Whether a bonding basin represents a two- or multi-centered, or lone-pair-like interaction, can be determined by applying the basin intersection technique [45]. In this technique the bonding basin is intersected with the atomic basins and the number of electrons contributed to the bond by each atom can be found by integrating the electron density in each intersection region. For obtaining a more general picture of the atomic interactions, it is sometimes reasonable to ignore contributions less than some small fraction (e.g., 10%) of the bond population [46]. Furthermore, the basin intersection technique enables us to quantify bond polarity and explore its relation to electronegativity differences [47, 48]. Another useful feature of the ELI formulation is the possibility of decomposing it into partial contributions [49]. Partial ELI, denoted as pELI, can be obtained in terms of either energy windows (crystalline solids) or molecular orbital contributions (molecules).

In this study we investigate the chemical bonding in ternary clathrate-I compounds $Ba_8T_6Ge_{40}$ by combining the topological analysis of the electron density (ED) and the ELI in its ELI-D representation. The features of electronic DOS are used for discussion.

Crystal Structure

The type-I clathrate structure consists of three framework and two guest atom positions (Fig. 1). These Wyckoff positions are 6*c*, 16*i*, 24*k* and 2*a*, 6*d*, respectively, in the space group $Pm-3n$ (no. 223). Only the 16*i* (*x x x*) and 24*k* (0 *y z*) positions have free parameters, others' coordinates are fixed by symmetry. In the context of $Ba_8T_6Ge_{40}$ clathrate phases the framework positions can be labeled as 6*c* = *Ge*1, 16*i* = *Ge*2 and 24*k* = *Ge*3. The *Ge*2 and *Ge*3 sites form two 20 – atom cages per unit cell,

while all framework atoms participate to form six 24 – atom cages per unit cell. The former are centered by the guest atoms at 2*a* and the latter at 6*d* positions. Each framework atom is four-coordinated by other framework atoms. This structural feature yields 24 × *Ge*1 – *Ge*3, 8 × *Ge*2 – Ge2, 12 × *Ge*3 – *Ge*3 and 48 × *Ge*2 – *Ge*3 contacts per formula unit. Hence, in total the framework contains 92 two-center two-electron bonds requiring 184 valence electrons per unit cell. The diamond structure is also generated by four-coordinated atoms, however the less dense clathrate-I framework differs from it significantly by the presence of three planar hexagons per unit cell. These hexagons are formed by two *Ge*1 and four *Ge*3 atoms. In the plane of the hexagons the *Ge*3 – *Ge*3 – *Ge*1 angles usually vary around 125 degrees deviating strongly from the tetrahedral value of 109.47 degrees. In addition, the hexagons along a crystallographic axis alternate between being "horizontal" and "vertical" so that two neighboring hexagons meet at the common *Ge*1 (6*c*) sites. Therefore, these sites are expected to behave differently in comparison to the other two framework sites. In fact, point defects, especially at relatively low concentrations, are observed to involve mostly the 6*c* Wyckoff position. In particular, in the binary clathrate-I compound $Ba_8Ge_{43}\square_3$ only half of the 6*c* sites are occupied by the *Ge* atoms [39]. The vacancies can be taken, to a good approximation, as fully ordered so that a 2 × 2 × 2 supercell in space group *Ia* – 3*d* (no. 230) with Pearson symbol *cI408* results [39, 40].

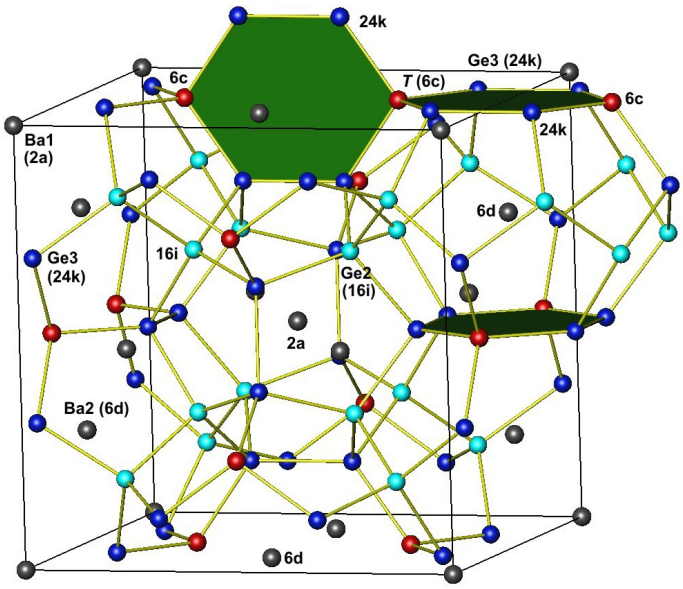

Figure 1. Crystal structure of clathrate-I $Ba_8T_6Ge_{40}$.

In the ternary clathrate-I compounds $Ba_8T_xGe_{46-x-y}\square_y$, the *T* atoms are usually located at the 6*c* sites for $x < 6$. Moreover, the vacancies are found exclusively at the *6c* sites (reminiscent of the binary clathrate $Ba_8Ge_{43}\square_3$). Consequently, almost all $Ba_8T_xGe_{46-x-y}\square_y$ phases are structurally disordered resulting in complex crystal structures. However, the main purpose of this study is to investigate chemical bonding in ternary type-I clathrate compounds in real space with emphasis on *Ba* – *T* and *T* – *Ge* interactions and the effects of these interactions on the *Ge* – *Ge* bonds. The complications due to the crystal structure were avoided by employing a simplified structural model with all 6*c* sites occupied by *T* atoms. The corresponding fully-ordered crystal structure model has the composition $Ba_8T_6Ge_{40}$. We consider the cases *T* = *Li*, *Mg*, *Al*, *Ga* and the late transition metals belonging to groups 9 – 12 of the Periodic Table. For comparison, the empty ($\square_8Ge_{46}$) and the binary ($Ba_8Ge_{43}\square_3$) clathrates as well as the hypothetical Ba_8Ge_{46} were included in the study.

Quantum chemical techniques

Electronic structure calculations were performed by using the all-electron, full-potential local orbital (FPLO) method [50] (version 9.01). All main results were obtained within the local density approximation (LDA) to the density functional theory through the Perdew-Wang parametrization for the exchange-correlation effects [51]. Some of the results were compared to those obtained by the generalized gradient approximation (GGA) [52] and no significant differences were found. In the FPLO method a scalar relativistic Hamiltonian is applied to the semi-core and valence electrons, while the core electrons are treated in a fully-relativistic way. Chemical bonding analysis is based on the combined analysis of electron density (ED) and electron localizability indicator (ELI). ELI [42] was calculated in the ELI-D representation [53, 54] by a module implemented into FPLO software [55]. Topological analysis of the ED and the ELI-D were carried out by the program DGrid [56].

The crystal structures of the type-I clathrates Υ_8Ge_{46}, Ba_8Ge_{46} and $Ba_8T_6Ge_{40}$ were fully optimized within LDA using a Brillioun zone (BZ) mesh of 8 × 8 × 8 and placing all *T* atoms at the 6*c* Wyckoff position of the space group $Pm-3n$ (no. 223). The maximum orbital angular momentum number was set to 12 for electron density expansion. The maximum force criterion was 5 meV $Å^{-1}$ and the equilibrium volume determination process was stopped when the estimated change in the lattice parameter was less than ~ 0.004 Å (corresponds to a volume ratio of ~0.1 %). For $Ba_8Ge_{43}\Upsilon_3$ the vacancy-ordered 2 × 2 × 2 superstructure model [39] was used without atomic position or unit cell volume optimization. The ELI-D and DOS calculations at the minimum-energy structures utilized a BZ mesh of 10 × 10 × 10.

Results and Discussion

The optimized values of the crystal structure parameters for Ba_8Ge_{46} and $Ba_8T_6Ge_{40}$ where *T* = *Li*, *Mg*, *Al*, *Ga* and transition metals of groups 9 – 12 are listed in Table I.

Table 1.

Optimized lattice parameters and atomic coordinates of *Ge*2 (16*i* site) and *Ge*3 (24*k* site) in the model $Ba_8T_6Ge_{40}$ structures.

Composition	*a* (Å)	*x* (16*i*)	*y* (24*k*)	*z* (24*k*)
$Ba_8Li_6Ge_{40}$	10.7126	0.1827	0.3118	0.1153
$Ba_8Mg_6Ge_{40}$	10.8433	0.1836	0.3040	0.1139
$Ba_8Al_6Ge_{40}$	10.7602	0.1843	0.3086	0.1184
$Ba_8Ga_6Ge_{40}$	10.7612	0.1845	0.3092	0.1186
$Ba_8Ge_6Ge_{40}$	10.8964	0.1847	0.3074	0.1183
$Ba_8Co_6Ge_{40}$	10.5064	0.1829	0.3255	0.1263
$Ba_8Ni_6Ge_{40}$	10.5098	0.1829	0.3233	0.1245
$Ba_8Cu_6Ge_{40}$	10.5643	0.1830	0.3180	0.1198
$Ba_8Zn_6Ge_{40}$	10.6500	0.1837	0.3118	0.1183
$Ba_8Rh_6Ge_{40}$	10.6380	0.1831	0.3185	0.1216
$Ba_8Pd_6Ge_{40}$	10.6624	0.1830	0.3146	0.1187
$Ba_8Ag_6Ge_{40}$	10.7484	0.1830	0.3085	0.1157
$Ba_8Cd_6Ge_{40}$	10.8410	0.1838	0.3028	0.1149
$Ba_8Ir_6Ge_{40}$	10.6539	0.1832	0.3178	0.1219
$Ba_8Pt_6Ge_{40}$	10.6631	0.1831	0.3148	0.1202
$Ba_8Au_6Ge_{40}$	10.7238	0.1832	0.3093	0.1169
$Ba_8Hg_6Ge_{40}$	10.8454	0.1837	0.3024	0.1155

Electronic structure

Since, each framework atom is four-coordinated by other framework atoms in an approximately tetrahedral environment, an empty clathrate such as Υ_8Ge_{46}, in analogy to the diamond structure, is expected to have an energy band gap [57]. Indeed, we obtained a band gap of 1.22 eV for the fully-optimized Υ_8Ge_{46} structure. The corresponding electronic density of states (DOS) is presented in Figure 2, upper panel. In $Ba_8Ge_{43}\Upsilon_3$, there are 16 extra electrons from the *Ba* atoms, but due to the missing three *Ge* atoms at the 6*c* position the net number of the excess electrons is four: $(Ba^{2+})_8[(3b)Ge^-]_{12}[(4b)Ge^0]_{31}\cdot 4e^-$, where (*3b*) and (*4b*) denote three- and four-bonded *Ge*, respectively. The calculated electronic structure of $Ba_8Ge_{43}\Upsilon_3$ [58] shows that the band gap of Υ_8Ge_{46} is preserved although its width is reduced to about 0.2 eV, and top of the gap lies 0.5 eV below the Fermi energy (E_F, Fig. 2, middle panel). The number of electrons occupying the states between -0.5 eV and Fermi energy (set to 0 eV) is exactly four, in agreement with the above simple electron counting. For the hypothetical binary clathrate-I Ba_8Ge_{46} the net number of the excess electrons is 16 and therefore top of the gap lies further below the E_F, at about -0.85 eV (Fig. 2, lower panel). The width of the gap is ~0.6 eV. The preservation of the gap implies that the *Ba* states, mainly *5d*, hybridize only weakly with those of the *Ge* framework in the region below the gap.

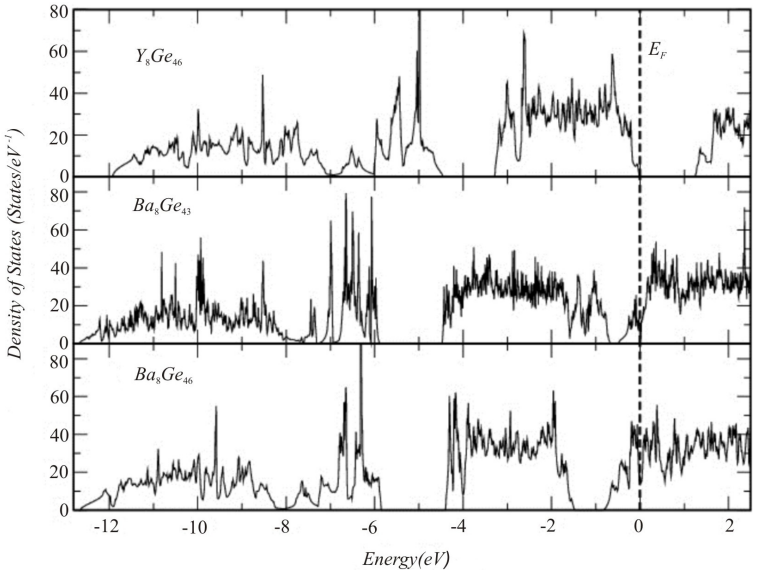

Fig. 2. Calculated electronic density of states for Υ_8Ge_{46}, $Ba_8Ge_{43}\Upsilon_3$, and Ba_8Ge_{46}.

An important question is what happens to the gap when atoms of a third element are introduced to the clathrate-I structure. In the case of *Ba – T – Si* type-I clathrate phases for *T = Ni* [59] and *Rh* [60], the rather strong hybridization between the *d* electrons of *T* and the *p* electrons of Si results in the closing of the gap (reminiscent of the empty Υ_8Si_{46} clathrate). In contrast, we find for the case of $Ba_8T_6Ge_{40}$, that the band gap persists even when six atoms of the element *T = Li*, *Mg*, *Al*, *Ga* (Fig. 3) or a transition metal from groups 9 through 12 (Fig. 4) replace the *Ge* atoms at the *6c* position. The Fermi energy lies above or below the gap depending on the ability of the *T* elements to a accommodate valence electrons of *Ba* with respect to the empty clathrate Υ_8Ge_{46}. According to the Zintl-Klemm concept each *T* atom would need four electrons for forming four two-electron two-center bonds with the neighboring *Ge* atoms. The difference between four and the number of valence electrons *v* of the *T* atom yields its accommodation ability of *T*. The comparison of the accommodation ability of six *T* atoms with the 16 electrons transferred from *Ba* determines the location of the gap with respect to E_F:

if the accommodation ability of six *T* is less than 16, the gap is below the Fermi level and *vice versa*. The DOS results to be presented below show the validity of this argumentation providing support for the applicability of the Zintl-Klemm concept to the ternary clathrate-I phases $Ba_8T_6Ge_{40}$.

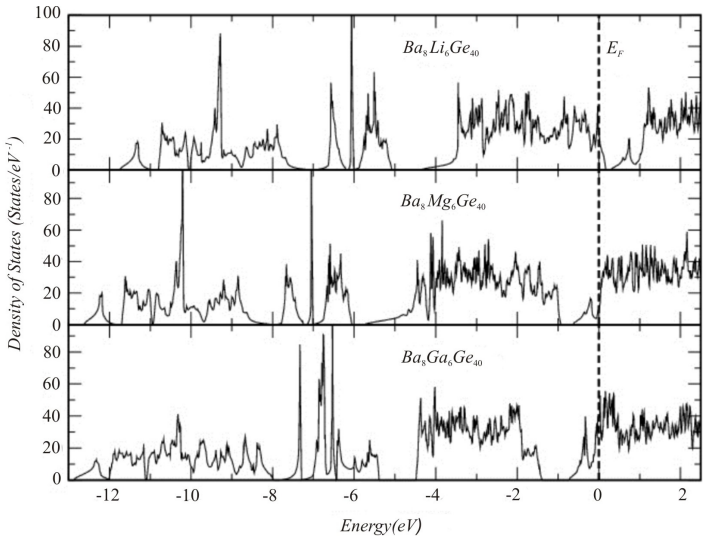

Fig. 3. Calculated electronic density of states for $Ba_8T_6Ge_{40}$ with T = Li, Mg, Ga.

Lithium has one valence electron, therefore in $Ba_8Li_6Ge_{40}$ there are two electrons less compared to Y_8Ge_{46}: $(Ba^{2+})_8[(LiGe_4)^{3-}]_6[(4b)Ge^0]_{16}\cdot 2e^+$, where e^+ stands for a hole. Hence, the gap is above E_F (Fig. 3 upper panel) and the integrated DOS between E_F and bottom of the gap reveals two electrons as expected. Similar count for *Mg* and *Ga* (two and three valence electrons, respectively) yields 4 and 10 extra electrons – $(Ba^{2+})_8[(MgGe_4)^{2-}]_6[(4b)Ge^0]_{16}\cdot 4e^-$ and $(Ba^{2+})_8[(GaGe_4)^{1-}]_6[(4b)Ge^0]_{16}\cdot 10e^-$, respectively – so that E_F ends up above the gap (Fig. 3 middle and lower panels). In these cases also the integrated DOS between top of the gap and E_F gives the expected electron numbers.

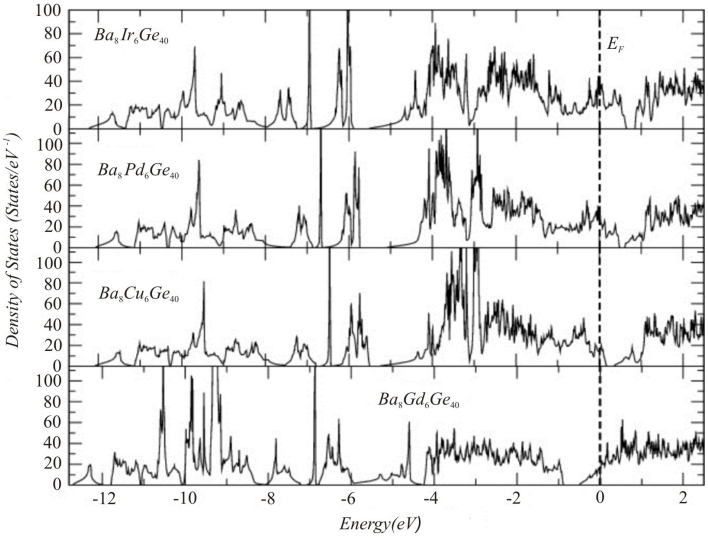

Fig. 4. Calculated electronic density of states for $Ba_8T_6Ge_{40}$ with T = Ir, Pd, Cu and Cd.

By comparing Figs. 3 and 4, we deduce similar behavior for *T* = *Li*, *Cu*, *Ag*, *Au* and for *T* = *Mg*, *Zn*, *Cd*, *Hg* sets showing DOS consistent with the picture for *T* having one or two valence electron(s). Recent experimental and theoretical work on $Ba_8Au_xSi_{46-x}$ [61] and $Ba_8Au_xGe_{46-x}$ [16] phases have revealed that as *x* is varied from below 5.33 to above 5.33 the nature of the charge carrier transport in the corresponding compounds changes from *n*-type (electron-rich case) to *p*-type (electron-poor case).

This transition can be explained if *Au* atoms act as having one valence electron so that each of them needs three electrons from the *Ba* atoms to make two-electron bonds with *Ge* neighbors. The critical value of $x = 16/3 = 5.33$ to match the number of available electrons to the electron demand is simply the number of *Au* atoms that can accommodate all 16 electrons available from *Ba*. Group 10 elements have one electron less than their group 11 neighbors, thus they are expected to behave as if they have zero valence electrons. With ν set to 0 we obtain accommodation ability of 24 for 6 *Pd* atoms. With 16 available electrons of 8 *Ba* species, it places the E_F below the gap. The computed DOS (Fig. 4, *T* = *Pd*) is in agreement with this expectation, and the integrated DOS from E_F to the bottom of the gap yields 8 electrons as expected. The electron balance for *T* = *Ni* can be – similarly to the *Pd* case - expressed as $(Ba^{2+})_8[(NiGe_4)^{4-}]_6[(4b)Ge^0]_{16}\cdot 8e^+$. Experimental evidence for the electronic state of *Ni* exists for $Ba_8Ni_xGe_{46-x-y}\square_y$ [19] and $Ba_8Ni_xSi_{46-x-y}\square_y$ phases [63], for which X-ray absorption studies carried out on *Ni* sites suggest an oxidation state close to that of elemental *Ni*. In the case of group 9 elements, one electron less than in group 10, one would set ν to -1, e.g., $(Ba^{2+})_8[(CoGe_4)^{5-}]_6[(4b)Ge^0]_{16}\cdot 14e^+$, so that E_F falls further below the gap (Fig. 4, top panel). For all group 9 elements the states between E_F and the bottom of the gap are found to accommodate 14 electrons.

The electron balances derived from the Zintl model of atomic interactions in clathrates and their correlation with the electronic density of states allow description of the electronic transport in this family of thermoelectric materials for any values of *x* within the experimentally found homogeneity ranges of the phases $Ba_8T_xGe_{46-x-y}\square_y$. Analysis of the thermal transport behavior reveals that the lattice thermal conductivity does not follow the changes in the electronic structure [10] and shows for the case of *T* = *Au* some influence of the distinct atomic interactions in the crystal structure [16]. A systematic analysis of such interactions is made by real-space quantum chemical techniques.

Chemical bonding in real space

The QTAIM basins and their electron populations were obtained for the $Ba_8T_6Ge_{40}$ clathrates by applying the topological analysis to the electron density. The shapes of QTAIM basins are shown in Fig. 5 for $Ba_8Cu_6Ge_{40}$. One notices that both *Ba*1 and *Ba*2 basins have highly spherical shapes. This implies that *Ba* atoms act mainly as cations: the atomic basin of an ideal cation should consist only of the core electron shells whose electron density would have a spherical distribution. The QTAIM basins of the *Ge* and *Cu* atoms, on the other hand, are far from being spherical indicating the presence of more directional interactions (in comparison with the ionic ones).

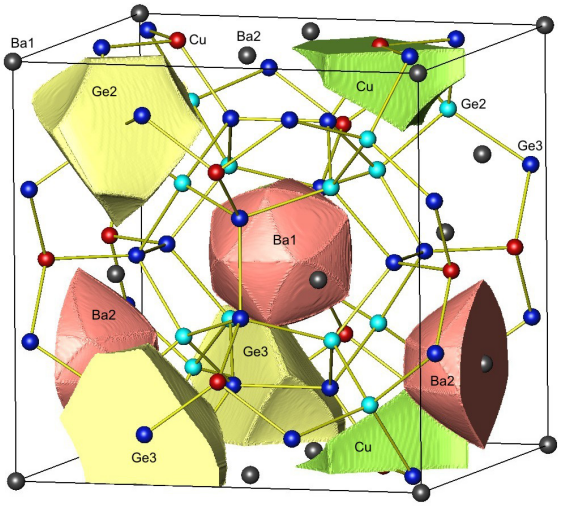

Fig. 5. QTAIM atoms in $Ba_8T_6Ge_{40}$ by the example of T = Cu.

The effective charge of an atom within the electron localizability approach is defined as the difference between the atomic number Z and the electron population of the atomic basin Q. Fig. 6 shows the calculated effective charges ($Z - Q$) of the T atoms in relation to their position in the Periodic Table. Due to the similarity of the electronic DOS, *Li* and *Mg* are assigned to groups 11 and 12, respectively, for plotting purposes. Large positive effective charges are observed for the main group elements *Li*, *Mg* and *Al*. Normalizing the effective charges for one formal valence one obtains +0.80, +0.65 and +0.47, respectively, correctly reproducing the order of increasing electronegativity (*EN*) within one row. The main group element of the next row – gallium – has a smaller positive effective charge than aluminum being also in agreement with the electronegativity of the elements of group 13 ($EN(Ga) > EN(Al)$). There are two general remarks in regard to the transition metals: the effective charges (i) get more negative within each group as period number increases, (ii) get less negative within each period as group number increases. Both observations are in line with the general tendency of how electronegativity changes across the Periodic Table. *Ge*3 atoms are the nearest neighbors of the *T* ones; therefore their effective charges vary in a wide range. One limit corresponds to the case of electropositive elements $(Z - Q)_{Ge3} \approx -0.60$ for $T = Mg$ and *Al*, and the other to *Ir* and *Pt* with $(Z - Q)_{Ge3} \approx -0.05$. *Ba*2 and *Ge*2 effective charges show a variation of approximately the same width: (1.2 ÷ 1.4) for *Ba*2 and (-0.3 ÷ -0.1) for *Ge*2. Since the *Ba*1 – *T* and *Ba* – *Ge* distances (> 0.559 times the lattice parameter) are the longest among the host-guest distances, *Ba*1 effective charges change very little, they lie between 1.1 and 1.2.

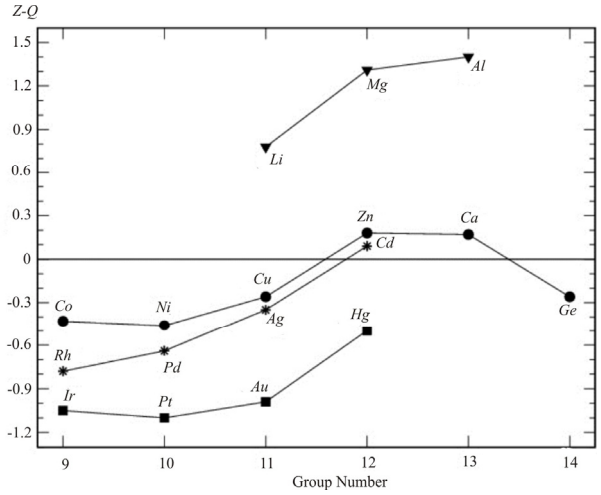

Fig. 6. Effective charges for QTAIM atoms in $Ba_8T_6Ge_{40}$.

More insight about how $Ge - T$ and $Ge - Ge$ interactions are affected as T is changed was gained by performing the topological analysis of the ELI-D. The ELI-D distributions at $x = a/2$ for some representative cases are shown in Figure 7. Apart from the *Ge*2 – *Ge*2 and *Ge*2 – *Ge*3 bonds all other bonding situations of interest are present in this plane. The *Ge*3 – *Ge*3 attractors are off the bond line, but usually very close to it. Electron populations of bond basins are calculated by integrating the ED inside the valence-region ELI-D basins. Basin intersection technique is used to determine how many electrons are contributed by which atoms. In general the $Ge - Ge$ bonds have a two-center character with *Ba* contributions always being less than ~ 2% of the bond population. In the empty clathrate Υ_8Ge_{46} there are, as expected, only two-center two-electron $Ge - Ge$ bonds. In Ba_8Ge_{43}, due to the vacancies at the 6*c* site, the basins of the former *Ge*1 – *Ge*3 bonds have contact only to one *Ge*3 core, i.e., they represent lone pairs at *Ge*3 atoms [64]. The bond populations are as follows: for *Ge*2 – *Ge*2 bond – 2.25 e^-, for *Ge*3 – *Ge*3 bond – 1.95 e^-, for *Ge*1 – *Ge*3 bond – 2.17 e^-, for *Ge*3 lone pair – 2.52 e^-

and for *Ge*2 – *Ge*3 bond – 2.10 e^- (when *Ge*3 has a *Ge*1 neighbor), 1.92 e^- (for *Ge*2 at 32*e* position) and 2.05 e^- (when *Ge*2 is at 96*h* position and *Ge*3 has a lone pair). These values are essentially independent of whether LDA or GGA is used in the calculation.

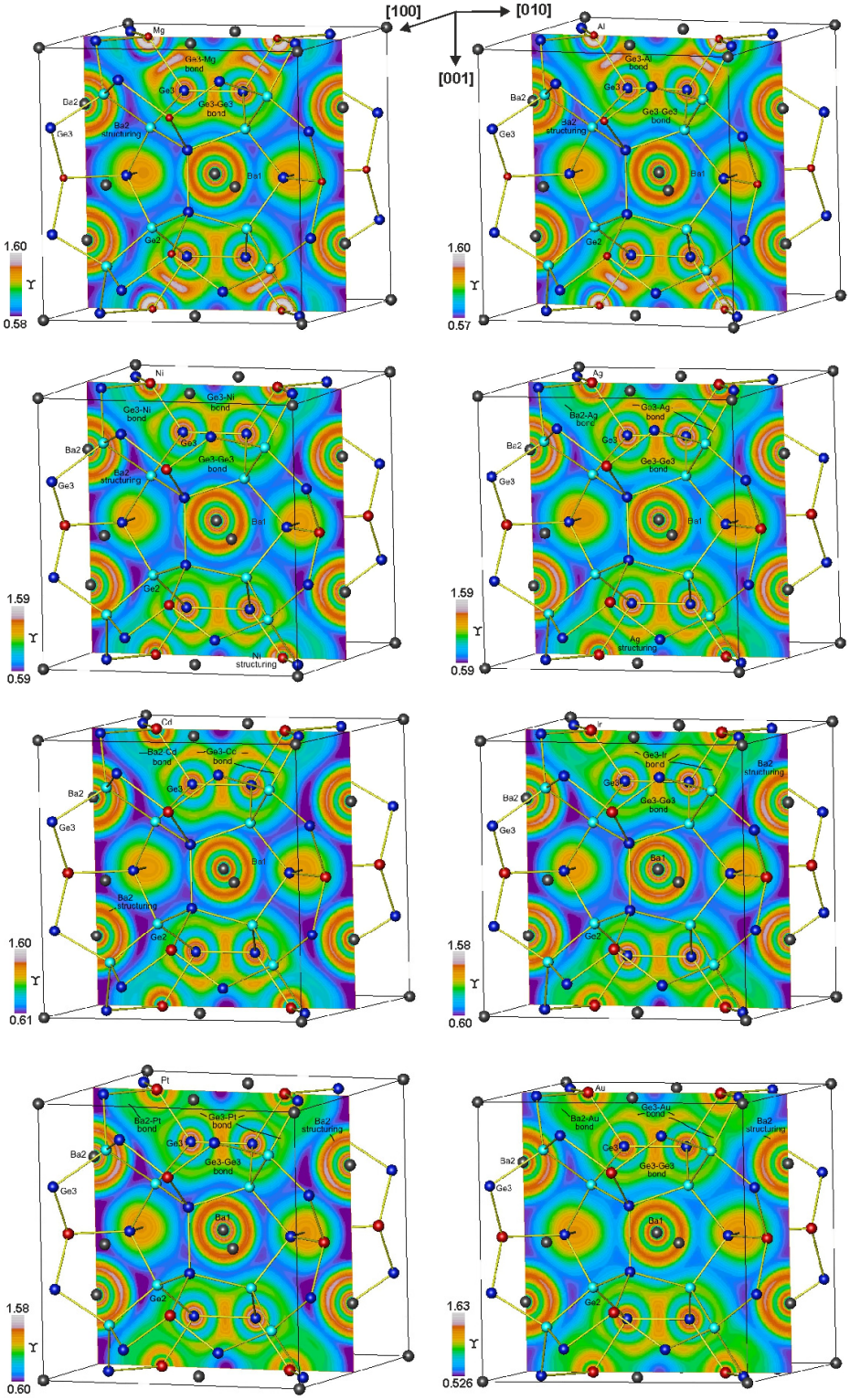

Fig. 7. ELI-D distribution in $Ba_8T_6Ge_{40}$ at x = 0.5 for T = Mg, Al, Ni, Ag, Cd, Ir, Pt, Au.

The *Ge* – *Ge* bond populations are plotted against *Ge* – *Ge* distances in the studied $Ba_8T_6Ge_{40}$ clathrates in Fig. 8. The *Ge*2 – *Ge*2 bonds are the least affected by *T* due to the rather long *Ge*2 – *T*

contacts of about 4 Å. Their bond populations vary between 2.2 and 2.3 electrons and the *Ge*2 – *Ge*2 distances lie between 2.44 and 2.50 Å. The *Ge*2 – *Ge*3 distances vary in a narrow range, 2.48 – 2.53 Å, but the bond populations show a wider variation: 1.88 to 2.15 electrons. As expected, the *Ge*3 – *Ge*3 values are spread over considerably wider ranges of [1.7, 2.05] e^- and [2.47, 2.66] Å for bond population and bond distance, respectively. In the *Ge*2 – *Ge*2 and *Ge*3 – *Ge*3 bonds, *Ge* atom contributions are equal, but the *Ge*2 – *Ge*3 bonds are slightly polar (similar to the *Ge*3 – *Ge*1 case above) due to different local environments [66].

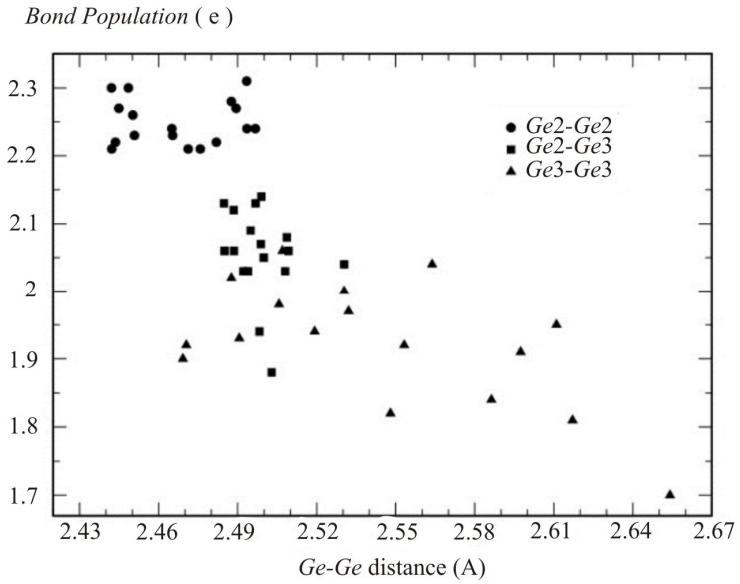

Fig. 8. Ge - Ge bond populations versus Ge - Ge bond distances in $Ba_8T_6Ge_{40}$.

The *Ge*3 – *T* bond attractors have in the isolated *GeT* molecules usually ring characteristics [43, 49]. In the $Ba_8T_6Ge_{40}$ clathrates, due to the non-cylindrical symmetry of the *Ge* – *T* bond environment they are split into two for all transition metals (Fig. 7). In addition, the structuring of the penultimate shell is observed for most transition metals, e.g. for the 3rd and 4th shells for *Ni* and *Ag*, respectively, it is noted in Fig. 7. The structuring of the penultimate shell of the *T* species is very weak for group 12 atoms and is missed in the case of main group elements. The bond polarity of the *Ge* – *T* bonds is a consequence of the different atomic charges of the participating atoms.

Information on *Ba* – framework interactions can be inferred from the structuring of *Ba* atoms' penultimate (5th) shell. In all cases the structuring of *Ba*2 penultimate shell is significant enough to be noticed in two-dimensional plots of the ELI-D distribution (Fig. 7). In contrast, *Ba*1 structuring is comparatively very small, it is noticeable only for *T* = *Pt*. In the ELI-D representation of the *Ba* atom, the 5*p* states contribute also to the valence region. i.e., they may as well be participating in atomic interactions. An interesting finding is the detection of two-center *Ba*2 ← *T* dative bonds for *T* = *Ag*, *Cd*, *Pt* and *Au* manifested by the dedicated ELI-D attractor (Fig. 7). Covalent *Ba*2 – *Au* bonds were reported in a previous study which employed the tight-binding linear-muffin-tin orbital (TB-LMTO) method [16]. This result is confirmed in the present FPLO calculations by applying either LDA or GGA techniques. Additionally, three new cases are found. Bond populations are 0.10, 0.06, 0.16 and 0.27 electrons for *Ag*, *Cd*, *Pt* and *Au*, respectively. These bonds are strongly polar with the bond fraction [48] of *Ba*2 atoms being 0.05 – 0.06. Because some of the *Pt* or *Au* electrons are used for forming the according dative *Ba*2 – *T* bonds, the low values of bond populations of the *Ge*3 – *Pt* and *Ge*3 – *Au* bonds are partly understandable. The partial ELI-D analysis based on the energy window

decomposition confirms the *T*(*d*) participation for *T* = *Ag*, *Pt* and *Au*. Here, the *Ba*2 – *T* ELI-D attractors show up when the lower limit of the energy window is chosen above the energy ranges dominated by the *T*(*d*) states. The upper limit is taken as the Fermi energy. The lower limits for the chosen energy windows are -4.15, -2.88 and -3.95 eV for *Ag*, *Pt* and *Au*, respectively. In these energy ranges *Ba 5d* contributions start to rise and transition metal *d* contribution remain below 10 states eV^{-1}. However, for *T* = *Cd* similar analysis failed to isolate an energy window where *Ba*2 – *Cd* ELI-D bond attractors occur. Here, the *Ba* – *Cd* bonding attractor results from the contributions of the whole valence manifold of *Cd*.

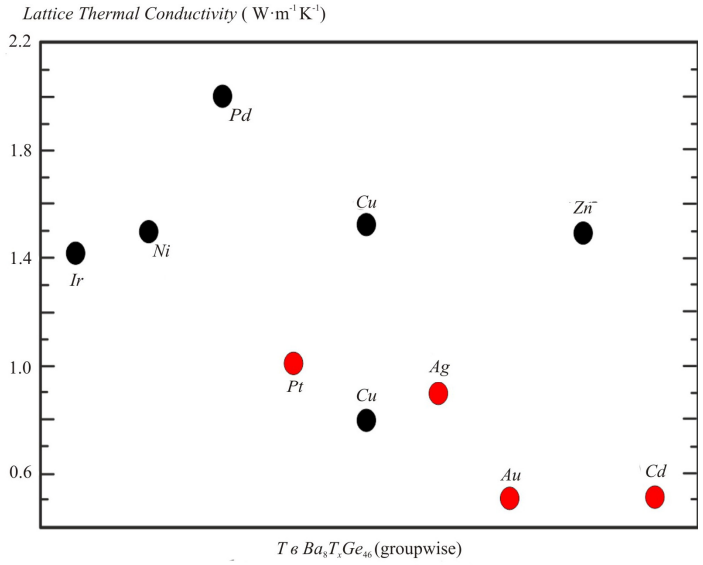

Fig. 9. Experimental minimum lattice thermal conductivity values at temperatures above 200 K for the $Ba_8T_xGe_{46-x}$ phases (100 K for T = Ir). Red points mark the T elements forming Ba – T bonds (cf. text).

Analysis of the lattice thermal conductivity κ_L of the ternary type-I clathrates $Ba_8T_xGe_{46-x-y}\square_y$ reported in the literature reveals strongly reduced values for all compounds having *Ba*2 – *T* bonds (Fig. 9). The κ_L is around 0.9 and 1.0 W m^{-1} K^{-1} for *Ag* and *Pt* [30, 34], respectively; it varies between 0.5 – 1.5 and 0.5 – 1.0 W m^{-1} K^{-1} for *Cd* and *Au* [16, 31, 65], respectively. As a comparison, κ_L values are above 1.4 – 1.5 W m^{-1} K^{-1} for *Ir* [66], *Ni* [18, 19] and *Zn* [23], and above 2.0 W m^{-1} K^{-1} for *Pd* [29]. Moreover, the κ_L values for the $Rb_{7.88}Au_{2.47}Ge_{43.53}$ clathrate are higher than 1.5 W m^{-1} K^{-1}, and the ELI-D analysis on $Rb_8Au_6Ge_{40}$ found no dedicated maxima on the *Rb* – *Au* contacts [67]. The exceptional case is that of *T* = Cu: the minimum value of κ_L is reported to be around 0.8 W m^{-1} K^{-1} [68], but the ELI-D analysis finds no *Ba*2 – *Cu* interaction with an dedicated attractor. Usually the low lattice thermal conductivities obtained for heavier *T* elements are explained as a mass effect, however the systematic investigation of the $Ba_8Au_xGe_{46-x}$ clathrate in very narrow range of $5.25 \le x \le 5.50$ revealed the change of κ_l from 0.55 to 0.9 W m^{-1} K^{-1} confirming rather the role of the *Ba* – *Au* bonding [65]. Furthermore, the iridium-containing clathrate with heavy *T* component does not show reduced lattice thermal conductivity, being in agreement with the absence of *Ba* – *Ir* interaction [66]. However, a role of the covalent *Ba*2 – *T* interactions deserves further investigation. In particular, further experimental work on *Hg* – and *Cu* – containing clathrates will be illuminating, because mercury is heavy and no *Ba*2 – *T* bonds were detected in the ELI-D analysis, and the *vice versa* case represents *T* = *Cu*, whereby the experimental data differ quite strongly from 0.8 to 1.5 W m^{-1} K^{-1} [21, 68] (Fig. 9).

Summary

The chemical bonding in ternary *Ba – Ge* - based clathrate-I phases is investigated by applying the QTAIM and electron localizability approach. The composition $Ba_8T_6Ge_{40}$ is used for the quantum chemical calculations where *T* atoms occupy the 6*c* Wyckoff position. The QTAIM analysis of the electron density shows that *Ba* atoms transfer about 1.2 – 1.3 electrons to the $[T_6Ge_{40}]$ framework. The *Ge*2 atoms coordinated only by germanium receive 0.1 – 0.2 electrons. The *Ge*3 atoms have *T* atoms in the first coordination sphere; thus, the effective charges of *Ge*3 vary more strongly from -0.05 to -0.60 depending on the polarity of the *Ge*3 – *T* bond. The *Ge – T* interactions are found to be essentially of two-center character with negligible *Ba*2 contributions. *Ba* – framework interactions are mostly ionic as expected from the Zintl-Klemm concept. However, the electrons in the 5th (penultimate) shell of *Ba* atoms do participate in atomic interactions with the framework atoms as judged from the non-spherical ELI-D distribution in these shells (structuring) and from the electronic DOS. Moreover, for *T* = *Cd*, *Ag*, *Pt* and *Au*, there are dedicated ELI-D bond attractors indicating two-center *Ba*2 – *T* interactions. Coexistence of different types of bonding in the clathrates $Ba_8T_6Ge_{40}$ is named as bonding inhomogeneity. The lattice thermal conductivity of the clathrate-I phases with these *Ba*2 – *T* bonds were reported to be lower in comparison with the phases without *Ba*2 – *T* bonding suggesting that such bonds play a role in heat transfer reduction.

References

1. J.S. Kasper, P. Hagenmuller, M. Pouchard, and C. Cros, Clathrate Structure of Silicon Na_8Si_{46} and Na_xSi_{136} (x < 11), *Science* 150, 1713 – 1714 (1965).
2. M. Christensen, S. Johnsen, and B.B. Iversen, Thermoelectric Clathrates of Type I*, Dalton Trans*. 39, 978 – 992 (2010).
3. S. Stefanoski, M. Beekmann, and G.S. Nolas, Inorganic Clathrates for Thermoelectric Applications in *The Physics and Chemistry of Inorganic Clathrates*, ed. G. S. Nolas (Springer, Dordrecht, Heidelberg, New York, London, 2014), p. 169 – 191.
4. T. Takabatake, K. Suekuni, T. Nakayama, and E. Kaneshita, Phonon-Glass Electron-Crystal Thermoelectric Clathrates: Experiments and Theory, *Rev. Mod. Physics* 86, 669 – 716 (2014).
5. H. Kawaji, H. Horie, S. Yamanaka, and M. Ishikawa, Superconductivity in the Silicon Clathrate Compound $(Na, Ba)_xSi_{46}$, *Phys. Rev. Lett*. 74, 1427 – 1429 (1995).
6. S. Yamanaka, E. Enishi, H. Fukuoka, and M. Yasukawa, High-Pressure Synthesis of a New Silicon Clathrate Superconductor, Ba_8Si_{46}, *Inorg. Chem*. 39, 56 – 58 (2000).
7. Slack, G. New Materials and Performance Limits for Thermoelectric Cooling in *CRC Handbook of Thermoelectrics, ed. D. M. Rowe* (CRC Press, Boca Raton, 1995), 407 – 440.
8. L. Zhang, A. Grytsiv, M. Kerber, P. Rogl, E. Bauer, and M. Zehebauer, Thermoelectric Performance of Mischmetal Skutterudites $Mm_yFe_{4-x}Co_xSb_{12}$ at Elevated Temperatures*, J. Alloys Compd.* 490, 19 – 25(2010).
9. M. Christensen, A.B. Abrahamsen, N.B. Christensen, F. Juranyi, N.H. Andersen, K. Lefmann, J. Andreasson, C.R.H. Bahl, and B.B. Iversen, Avoided Crossing of Rattler Modes in Thermoelectric Materials, *Nat. Mater.* 7, 811 – 815 (2008).
10. H. Euchner, S. Pailhès, L.T.K. Nguyen, W. Assmus, F. Ritter, A. Haghighirad, Yu. Grin, S. Paschen, and M. de Boissieu, Phononic Filter Effect of Rattling Phonons in the Thermoelectric Clathrate $Ba_8Ge_{40+x}Ni_{6-x}$,*Phys. Rev. B* 86, 224303 (2012).
11. S. Pailhès, H. Euchner, V.M. Giordano, R. Debord, A. Assy, S. Gomès, A. Bosak, D. Machon, S. Paschen, M.de Boissieu, Localization of Propagative Phonons in a Perfectly Crystalline Solid.

Phys. Rev. Lett. 113, 025506 (2014)**.**
12. T. Tadano, Y. Gohda, and S. Tsuneyuki, Impact of Rattlers on Thermal Conductivity of a Thermoelectric Clathrate: A First-Principles Study*, Phys. Rev. Lett*. 114, 095501 (2015).
13. M.M. Koza, A. Leithe-Jasper, H. Rosner, W. Schnelle, H. Mutka, M.R. Johnson, M. Krisch, L. Capogna, and Yu. Grin, Vibrational Dynamics of the Filled Skutterudites $M_{1-x}Fe_4Sb_{12}$ (M = *Ca*, *Sr*, *Ba*, and *Yb*): Temperature Response, Dispersion Relation, and Material Properties, *Phys. Rev. B* 84, 014306 (2011).
14. A. Saramat, G. Svensson, A.E.C. Palmqvist, C. Stiewe, E. Mueller, D. Platzek, S.G.K. Williams, D.M. Rowe, J.D. Bryan, and G.D. Stucky, Large Thermoelectric Figure of Merit at High Temperature in Czochralski-Grown Clathrate $Ba_8Ga_{16}Ge_{30,}$ *J. Appl. Phys*. 99, 023708 (2006).
15. X. Shi, J. Yang, S. Bai, J. Yang, H. Wang, V. Chi, J.R. Salvador, W. Zhang, L. Chen, and W. Wong-Ng,, On the Design of High-Efficiency Thermoelectric Clathrates through a Systematic Cross-Substitution of Framework Elements*, Adv. Funct. Mater*. 20, 755 – 763 (2010).
16. H. Zhang, H. Borrmann, N. Oeschler, C. Candolfi, W. Schnelle, M. Schmidt, U. Burkhardt, M. Baitinger, J.-T. Zhao, and Yu. Grin, Atomic Interactions in the *p*-Type Clathrate I $Ba_8Au_{5.3}Ge_{40.7}$, *Inorg. Chem*. 50, 1250 – 1257 (2011).
17. G.Cordier, P.Woll, Neue ternäre intermetallische Verbindungen mit Clathratstruktur: $Ba_8(T, Si)_6Si_{40}$ und $Ba_6(T, Ge)_6Ge_{40}$ mit T ≡ *Ni*, *Pd*, *Pt*, *Cu*, *Ag*, *Au*, *J. Less-Common Met*., 169, 291-302 (1991).
18. U. Aydemir, C. Candolfi, A. Ormeci, M. Baitinger, N. Oeschler, F. Steglich, and Yu. Grin, High Temperature Thermoelectric Properties of the Type-I Clathrate $Ba_8Ni_xGe_{46-x-y}\Upsilon_y$, *J. Phys. Cond. Mat*. 26, 485801 (2014).
19. U. Aydemir, C. Candolfi, A. Ormeci, M. Baitinger, U. Burkhardt, N. Oeschler, F. Steglich, and Yu. Grin, Electronic Band Structure and Low-Temperature Transport Properties of the Type-I Clathrate $Ba_8Ni_xGe_{46-x-y}\Upsilon_y$, *Dalton Trans*. 44, 7524 – 7537 (2015).
20. Y. Li, Y. Liu, N. Chen, G. Cao, Z. Feng, and J. H. Ross Jr., Vacancy and Copper-Doping Effect on Superconductivity for Clathrate Materials, *Phys. Lett*. A345, 398 – 408 (2005).
21. H. Zhang, J.-T.Zhao, M.-B.Tang, Z.-Y.Man, H.-H.Chen, and X.-X. Yang, Structure and Low Temperature Physical Properties of $Ba_8Cu_6Ge_{40}$, *J. Alloys Compd*. 476, 1 – 4 (2009).
22. N. Melnychenko-Koblyuk, A. Grytsiv, P. Rogl, H. Schmid, and G. Giester, The Clathrate $Ba_8Cu_xGe_{46-x-y}\Upsilon_y$: Phase Equilibria and Crystal Structure, *J. Solid State Chem*. 182, 1754 – 1760 (2009).
23. N. Melnychenko-Koblyuk, A. Grytsiv, L. Fornasari, H. Kaldarar, H. Michor, F. Rohrbacher, M. Koza, E. Royanian, E. Bauer, P. Rogl, M. Rotter, H. Schmid, F. Marabelli, A. Devishvili, M. Doerr, and G. Giester, Ternary Clathrates *Ba – Zn – Ge*: Phase Equilibria, Crystal Chemistry and Physical Properties, *J. Phys. Cond. Mat.* 19, 216223 (2007).
24. E. Alleno, G. Maillet, O. Rouleau, E. Leroy, C. Godart, W. Carrillo-Cabrera, P. Simon, and Yu. Grin, Germanium Vacancies and Charge Transport Properties in $Ba_8Zn_xGe_{46-x-y}\Upsilon_{y,}$ *Chem. Mater.* 21, 1485 – 1493 (2009).
25. T. Eto, K. Kishimoto, K. Koga, K. Akai, T. Koyanagi, H. Anno, T. Tanaka, H. Kurisu, S. Yamamoto, and M. Matsuura, Study of Zn-Substituted Germanium Clathrates as High Performance Thermoelectric Materials Assisted by First-Principles Electronic Structure Calculation, *Mat. Trans*. 50, 631 – 639 (2009).
26. N.A. Borshch, N.S. Pereslavtseva, and S.I. Kurganskii, Electronic Structure of Zn-substituted Germanium Clathrates*, Semiconductors* 43, 563 – 567 (2009).

27. B.Kuhl, A. Czybulka, H.-U. Schuster, Neue ternäre Käfigverbindungen aus den Systemen Barium–Indium/Zink/Cadmium–Germanium: Zintl-Verbindungen mit Phasenbreite? *Z. Anorg. Allg. Chem.* 621, 1 – 6 (1995).
28. M. Falmbigl, F. Kneidinger, M. Chen, A. Grytsiv, H. Michor, E. Royanian, E. Bauer, H. Effenberger, R. Podloucky, and P. Rogl, Cage-Forming Compounds in the *Ba – Rh – Ge* System: From Thermoelectrics to Superconductivity, *Inorg. Chem*. 52, 931 – 943 (2013).
29. N. Melnychenko-Koblyuk, A. Grytsiv, P. Rogl, M. Rotter, E. Bauer, G. Durand, H. Kaldarar, R. Lackner, H. Michor, E. Royanian, M. Koza, and G. Giester, Clathrate Formation in the *Ba – Pd – Ge* System: Phase Equilibria, Crystal Structure, and Physical Properties, *Phys. Rev*. B76, 144118 (2007).
30. I. Zeiringer, M.X. Chen, I. Bednar, E. Royanian, E. Bauer, R. Podloucky, A. Grytsiv, P. Rogl, H. Effenberger, Phase Equilibria, Crystal Chemistry, Electronic Structure and Physical Properties of *Ag – Ba – Ge* Clathrates, *Acta Mater*. 59, 2368 – 2384 (2011).
31. N. Melnychenko-Koblyuk, A. Grytsiv, S. Berger, H. Kaldarar, H. Michor, F.Rohrbacher, E. Royanian, E. Bauer, P. Rogl, H. Schmid, and G. Giester, Ternary Clathrates *Ba – Cd – Ge*: Phase Equilibria, Crystal Chemistry and Physical Properties, *J. Phys. Cond. Mat*. 19, 046203 (2007).
32. N.A.Borshch, N.S.Pereslavtseva, S.I.Kurganskii, Electron Structure and Spectral Characteristics of Cd-substituted Ge-based Clathrates, *Semiconductors* 44, 987 – 992 (2010).
33. M. Falmbigl, A. Grytsiv, P. Rogl, and G. Giester, Clathrate Formation in the Systems *Ba – Ir* – e and *Ba* – {*Rh*, *Ir*} – *Si*: Crystal Chemistry and Phase Relations, *Intermetallics* 36, 61 – 72 (2013).
34. N. Melnychenko-Koblyuk, A. Grytsiv, P. Rogl, M. Rotter, R. Lackner, E. Bauer, L. Fornasari, F.Marabelli, and G. Giester, Structure and Physical Properties of Type-I Clathrate Solid-Solution $Ba_8Pt_xGe_{46-x-y}\Upsilon_y$ (Υ=vacancy), *Phys.Rev.B* 76, 195124 (2007).
35. I. Zeiringer, N. Melnychenko-Koblyuk, A. Grytsiv, E. Bauer, G. Giester, and P. Rogl, *Phase* Equilibria, Crystal Chemistry and Physical Properties of Au-Ba-Ge Clathrates, *J. Phase Eq. Diff*. 32, 115 – 127 (2011).
36. S.Y. Rodriguez, L. Saribaev, J.H. Ross Jr., Zintl Behavior and Vacancy Formation in Type-I *Ba – Al – Ge* Clathrates, *Phys. Rev. B* 82, 064111 (2010).
37. N.L. Okamoto, K. Kishida, K. Tanaka, and H. Inui, Crystal Structure and Thermoelectric Properties of Type-I Clathrate Compounds in the *Ba – Ga – Ge* System, *J. Appl. Phys*. 100, 073504 (2006).
38. W. Carrillo-Cabrera, R. Cardoso Gil, S. Paschen, and Yu. Grin, Crystal Structure of $Ba_8Ga_{4.44}Ge_{39.14}\Upsilon_{2.42}$, $Ba_8Ga_{8.62}Ge_{36}\Upsilon_{1.38}$, and $Ba_8Ga_{12.35}Ge_{33.27}\Upsilon_{0.38}$, Three Clathrate-I Variants, *Z. Kristallog. NCS* 217, 183 – 185 (2002).
39. W. Carrillo-Cabrera, S. Budnyk, Y. Prots, and Yu. Grin, Ba_8Ge_{43} Revisited: a 2a'×2a'×2a' Superstructure of the Clathrate-I Type with Full Vacancy Ordering, *Z. Anorg. Allg. Chem*. 630, 2267 – 2276 (2004).
40. U. Aydemir, C. Candolfi, H. Borrmann, M. Baitinger, A. Ormeci, W. Carrillo-Cabrera, C.Chubilleau, B. Lenoir, A. Dauscher, N. Oeschler, F. Steglich,, and Yu. Grin, Crystal Structure and Transport Properties of $Ba_8Ge_{43}\Upsilon_3$ *, Dalton Trans*. 39, 1078 – 1088 (2010).
41. Yu. Grin, A. Savin, and B. Silvi, *The ELF Perspective of Chemical Bonding*. in *The Chemical Bond: Chemical Bonding Across the Periodic Table*, eds. G. Frenking, S. Shaik, Wiley-VCH, 2014, p. 1 – 53.
42. M. Kohout, A. Measure of Electron Localizability, *Int. J. Quantum Chem*. 97, 651 – 658 (2004).
43. Kohout, M., Wagner, F. R., Grin, Yu. *Electron localization function for transition-metal compounds*. Theor. Chem. Acc. 108, 2002, 150 – 156.

44. R.F.W. Bader, *Atoms in Molecules, A Quantum Theory* (Clarendon Press, Oxford, 1995).
45. S. Raub, G. Jansen, A Quantitative Measure of Bond Polarity from the Electron Localization Function and the Theory of Atoms in Molecules*, Theor. Chem. Acc*. 106, 223 – 232 (2001).
46. A.Ormeci, Yu. Grin, Chemical Bonding in Al_5Co_2: The Electron Localizability - Electron Density Approach*, Isr. J. Chem*. 51, 1349 – 1354 (2011).
47. D. Bende, Yu. Grin, and F.R. Wagner, Covalence and Ionicity in *MgAgAs*-Type Compounds, *Chem. Eur. J.* 20, 9702 – 9708 (2014).
48. D. Bende, F.R. Wagner, and Yu. Grin, 8-N Rule and Chemical Bonding in Main-Group *MgAgAs*-type Compounds, *Inorg. Chem*. 54, 3970 – 3978 (2015).
49. F.R. Wagner, V. Bezugly, M. Kohout, and Yu. Grin, Charge Decomposition Analysis of the Electron Localizability Indicator: A Bridge between the Orbital and Direct Space Representation of the Chemical Bond, *Chem. Eur. J*. 13, 5724 – 5741 (2007).
50. K. Koepernik, H. Eschrig, Full-Potential Nonorthogonal Local-Orbital Minimum-Basis Band-Structure Scheme, *Phys. Rev. B*59, 743 – 1757 (1999).
51. J.P. Perdew, Y. Wang, Accurate and Simple Analytic Representation of the Electron-Gas Correlation Energy, *Phys. Rev. B* 45, 13244 – 13249 (1992).
52. J.P. Perdew, K. Burke, and M. Ernzerhof, Generalized Gradient Approximation Made Simple*, Phys. Rev. Lett*. 77, 3865 – 3868 (1996).
53. M. Kohout, F.R. Wagner, and Yu. Grin, Atomic Shells From the Electron Localizability in Momentum Space*, Int. J. Quantum Chem*. 106, 1499 – 1507 (2006).
54. M. Kohout, Bonding Indicators from Electron Pair Density Functionals*, Faraday Discuss.* 135, 43 – 54 (2007).
55. A. Ormeci, H. Rosner, F.R. Wagner, M. Kohout, and Yu. Grin, Electron Localization Function in Full-Potential Representation for Crystalline Materials, *J. Phys. Chem*. A110, 1100 – 1105 (2006).
56.M. Kohout, *Program DGRID, version 4.6*, Radebeul, Germany, 2011.
57. J. Zhao, A.Buldum, J.P.Lu, Structural and Electronic Properties of Germanium Clathrates Ge_{46} and $K_8Ge_{46,}$, *Phys. Rev. B* 60, 14177 (1999).
58. C. Candolfi, A. Ormeci, U. Aydemir, M. Baitinger, N. Oeschler, Yu. Grin, and F. Steglich, Multiband Conduction in the Type-I Clathrate $Ba_8Ge_{43}\Upsilon_3$, *Phys. Rev. B* 84, 205118 (2011).
59. C. Candolfi, U. Aydemir, A. Ormeci, M. Baitinger, N. Oeschler, F. Steglich, and Yu. Grin, Low-Temperature Magnetic, Galvanomagnetic, and Thermoelectric Properties of the Type-I Clathrates $Ba_8Ni_xSi_{46-x}$, *Phys. Rev. B* 83, 205102 (2011).
60. W. Jung,, H. Kessens, A. Ormeci, W. Schnelle, U. Burkhardt, H. Borrmann, H.D. Nguyen, M.Baitinger, and Yu. Grin, Synthesis,Crystal Structure and Physical Properties of the Clathrate-I Phase $Ba_8Rh_xSi_{46-x-y}\Upsilon_y$ *, Dalton Trans*. 41, 13960 – 13968 (2012).
61. U. Aydemir, C. Candolfi, A. Ormeci, Y. Oztan, M.Baitinger, N. Oeschler, F. Steglich, and Yu. Grin, Low-Temperature Thermoelectric, Galvanomagnetic, and Thermodynamic Properties of the Type-I Clathrate $Ba_8Au_xSi_{46-x}$, *Phys. Rev. B* 84, 195137 (2011).
62. P. Tomeš, M. Ikeda, A. Sidorenko, S. Paschen, C. Candolfi, M. Baitinger, H.D. Nguyen, L. D.K.Nguyen, and Yu. Grin, Structural and physical properties of the clathrate-I phase $Ba_8Ir_xGe_{46-x-y}\ \Upsilon_y$ (x<0.4). 2016, submitted.
63. U. Aydemir, C. Candolfi, A. Ormeci, H. Borrmann, U. Burkhardt, Y. Oztan, N. Oeschler, M.Baitinger, F. Steglich, and Yu. Grin, Synthesis, Crystal Structure, and Physical Properties of the Type-I Clathrate $Ba_{8-\delta}Ni_x\Upsilon_ySi_{46-x-y}$, *Inorg. Chem*. 51, 4730 – 4741 (2012).

64. M. Baitinger, B. Boehme, A. Ormeci, and Yu. Grin, Solid State Chemistry of Clathrate Phases: Crystal Structure, Chemical Bonding and Preparation Routes. In: *The Physics and Chemistry of Inorganic Clathrates*, ed. G. S. Nolas (Springer, Dordrecht, Heidelberg, New York, London, 2014), pp. 35 – 64.
65. H.D. Nguyen, I. Antonyshyn, K. Meier-Kirchner, I. Veremchuk, W. Schnelle, U.Burkhardt, R. Carodoso Gil, B. Böhme, M. Baitinger, and Yu. Grin, Thermoelectric Characterization of the p-type Clathrate-I $Ba_8Au_{5.2+x}Ge_{40.8-x-y}\Upsilon_y$, 2016, submitted.
66. A. Ormeci, A. Simon, and Yu. Grin, *Structural Topology and Chemical Bonding in Laves Phases, Angew. Chem. Int. Ed*. 49, 8997 – 9001 (2010).
67. H. Zhang, M. Baitinger, L. Fang, W. Schnelle, H. Borrmann, U. Burkhardt, A. Ormeci, J.-T. Zhao, and Yu. Grin, Synthesis and Properties of Type-I Clathrate Phases $Rb_{8-x-t}K_x\Upsilon_tAu_yGe_{46-y}$. *Inorg. Chem*. 52, 9720 – 9726 (2013).
68. X. Yan, E. Bauer, P. Rogl, and S. Paschen, Structural and Thermoelectric Properties of $Ba_8Cu_5Si_xGe_{41-x}$ Clathrates*, Phys. Rev. B* 87, 115206 (2013).

Submitted 08.01.2016

Gaidar G.P.

G.P.Gaidar[1], P.I.Baranskii[2]

[1]Institute for Nuclear Research, NAS Ukraine,
47, Nauky Ave., Kyiv, 03680, Ukraine
[2]V.E. Lashkaryov Institute of Semiconductor Physics,
NAS Ukraine, 45, Nauky Ave., Kyiv, 03028,
Ukraine;

Baranskii P.I.

SOME PECULIARITIES OF THERMOPOWER ANISOTROPY IN UNDEFORMED AND ELASTICALLY DEFORMED *n - Si* AND *n - Ge* SINGLE CRYSTALS

In the framework of anisotropic scattering theory the mechanisms of origination of thermopower anisotropy in multi-valley undeformed and directionally deformed semiconductors (n -Si and n -Ge) in the presence of temperature gradient were analyzed in detail. Based on the use of the generalized Ohm's law the thermopower tensor was defined under $\nabla T \neq 0$.

Keywords: germanium, silicon, anisotropic scattering theory, thermopower anisotropy, thermopower tensor.

Introduction

Electrophysical properties of semiconductors are essentially dependent not only on the anisotropy of dispersion law and the mechanisms of charge carrier scattering on phonons and impurity centres, phonon-phonon scattering, etc. (i.e. on microlevel anisotropy), but also on the reduced (for instance, by means of directional elastic deformation) anisotropy of the entire crystal [1 – 3]. A deeper insight into the mechanisms of origination of thermopower anisotropy, peculiarities of the energy spectrum of charge carriers is promoted by studies of thermoelectric properties of uniaxially elastically deformed semiconductors that are important from the standpoint of not only basic, but also applied science [4]. Practical importance of such studies is related to the possibility of creating (or increasing) by means of directional deformation of semiconductors the thermopower anisotropy which is used in the anisotropic thermoelements, eddy and galvanothermomagnetic energy converters [5]. It is exactly the efficiency of thermoelectric energy converters that are commonly referred to as modules that governs the possibilities of practical applications of thermoelectricity [6].

An essential drawback of thermoelectrically anisotropic materials used for industry is their low thermoelectric figure of merit. As long as one of the methods for improving the latter is to increase thermopower anisotropy, creation of high thermopower anisotropy by deformation will assure the possibility of designing artificial high-sensitivity anisotropic devices with higher efficiency.

The purpose of this work was to establish specific features of thermopower anisotropy in undeformed and elastically deformed *n – Si* and *n – Ge* single crystals, as well as to determine thermopower tensor in the presence of temperature gradient.

Anisotropic electron scattering in multi-valley n-type semiconductors *Ge* and *Si*

An appropriate idea of anisotropic electron scattering in a crystal appears when solving a kinetic Boltzmann-Lorentz equation for charge carriers in solids. This equation for steady-state conditions can be written as [7]:

$$\hat{D}\, n_{\vec{k}} + \sum_{\vec{k}'} W_{\vec{k}\vec{k}'} \left(n_{\vec{k}'} - n'_{\vec{k}} \right) = 0 , \tag{1}$$

where $n_{\vec{k}}$ is equilibrium electron distribution function; $\hat{D}\, n_{\vec{k}} = \frac{1}{kT} \frac{dn^0_{\vec{k}}}{dx_{\vec{k}}} \left(\upsilon_{\vec{k}}, \nabla\overline{\mu} + x_{\vec{k}} \nabla kT \right)$ is the so-called field term; $\nabla\overline{\mu} = \nabla\mu - e_0 E = \nabla\left(\mu + e_0\psi\right)$; ψ is electric field potential; e_0 is electron charge; $n'_{\vec{k}}$ is the nonequilibrium addition to distribution function; $W_{\vec{k}\vec{k}'}$ is probability of electron scattering from the state with quasi-pulse $\vec{k}$ to the state with quasi-pulse $\vec{k}'$.

Hereinafter we shall consider only elastic scattering whereby it can be considered that quasi-pulses $\vec{k}$ and $\vec{k}'$ are on the same constant-energy surface. In this case, scattering probability is a function of several values:

$$W_{\vec{k}\vec{k}'} = W\left(\varepsilon; \vartheta, \varphi, \vartheta', \varphi' \right) \tag{2}$$

where ϑ, φ are spherical angles characterizing quasi-pulse direction prior to scattering, and ϑ', φ' – after scattering. In so doing, ε enters (2) as a parameter, since electron energy at scattering is not changed. Therefore, in the following the value of ε will not be entered into the notation of W function.

Let us first assume that scattering probability depends only on scattering angle θ:

$$W_{\vec{k}\vec{k}'} = W\left(\cos\theta \right), \tag{3}$$

in which case

$$\cos\theta = \cos\vartheta \cos\vartheta' + \sin\vartheta \sin\vartheta' \cos\left(\varphi - \varphi' \right), \tag{4}$$

It means that scattering probability does not depend on the way the angle formed by pulses $\vec{k}$ and $\vec{k}'$ is oriented inside a crystal (Fig. 1). Exactly such scattering is commonly referred to as isotopic. It is noteworthy that sometimes isotropic scattering shall mean the case when $W_{\vec{k}\vec{k}'}$ does not depend on θ at all. However, in reality this case is just a variety of isotropic scattering.

Anisotropic scattering shall mean the case when $W_{\vec{k}\vec{k}'}$ depends on the angles ϑ, φ, ϑ', φ' in any way different from dependence (3). Hereinafter we shall also assume that constant-energy surface is square-shaped (sphere, ellipsoid). It also includes the Kane nonparabolicity. Then carrier velocity components $\upsilon_x \sim \sin\vartheta\cos\varphi$; $\upsilon_y \sim \sin\vartheta\sin\varphi$; $\upsilon_z \sim \cos\vartheta$ linearly depend on first-order spherical harmonics. Solution of the kinetic equation for isotropic scattering is of dissimilar nature than for the case of anisotropic scattering.

With the isotropic scattering $W\left(\cos\theta\right)$ can be expanded into a series in the Legendre polynomials:

$$W\left(\cos\theta \right) = \sum_l W_l \, P_l\left(\cos\theta \right). \tag{5}$$

And then, using known theory of summation of spherical functions

$$P_l(\cos\theta) = \sum_m Y_{lm}(\vartheta,\varphi)\, Y^*_{lm}(\vartheta',\varphi'), \tag{6}$$

Eq.(5) can be represented as

$$W(\cos\theta) = \sum_{lm} W_l\, Y_{lm}(\vartheta,\varphi)\, Y^*_{lm}(\vartheta',\varphi'). \tag{7}$$

Solution of the kinetic equation in this case should be sought for in the form of a series in spherical harmonics:

$$n'_{\vec{k}} = \sum_{lm} X_{lm}(\varepsilon)\, Y_{lm}(\vartheta,\varphi), \tag{8}$$

in so doing, $X_{lm}(\varepsilon)$ need to be defined. One can make sure that substitution of Eq. (8) into Eq. (1) yields the following relationship for X_{lm}:

$$L_l\, X_{lm}(\varepsilon) = D_m\, \delta_{l1}, \tag{9}$$

where L_l is in a definite way calculated through coefficients W_l. It follows from here that all $X_{lm}(\varepsilon)$, except for $X_{1m}(\varepsilon)$, are equal to zero, which yields known solution of the kinetic equation with the isotropic scattering.

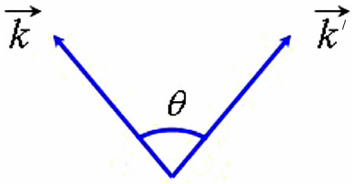

Fig. 1. Angle formed by quasi-pulses $\vec{k}$ and $\vec{k}'$.

In the case of the anisotropic scattering the expansion of $W_{\vec{k}\vec{k}'}$ in spherical harmonics is of the form

$$W_{\vec{k}\vec{k}'} = \sum_{ll'mm'} W_{ll'}^{mm'}\, Y_{lm}(\vartheta,\varphi)\; Y^*_{l'm'}(\vartheta',\varphi'). \tag{10}$$

And, hence, the fundamental difference between the anisotropic and isotropic scattering is that in the case of the anisotropic scattering the expansion coefficients of $W_{ll'}^{mm'}$, first, depend on *m* and, second, are non-diagonal both in *l* and in *m*. As a result, with the anisotropic scattering for unknown functions $X_{lm}(\varepsilon)$ we obtain a system of coupled equations, rather than an autonomous equation

$$\sum_{l'm'} L_{ll'}^{mm'}\, X_{l'm'}(\varepsilon) = D_m\, \delta_{l1}. \tag{11}$$

And to calculate the kinetic coefficients, one need not know the entire distribution function assigned by series (8), but only the so-called abbreviated function

$$\bar{n}'_{\vec{k}} = \sum_m X_{1m}(\varepsilon)\; Y_{1m}(\vartheta,\varphi), \tag{12}$$

since, due to the foregoing, for charge carriers with a quadratic constant-energy surface charge carrier velocities are proportional to first-order spherical harmonics.

In terms of mathematics, construction of anisotropic scattering theory comes down exactly to development of methods for determination of $X_{1m}(\varepsilon)$ from system (11) [8, 9], and the difference

between the anisotropic and isotropic scattering in conceptual sense reduces to the fact that in the case of anisotropic scattering the relaxation properties of carrier system are determined not by one coefficient L_1, but by certain combinations of the entire collection of expansion coefficients $L_{ll'}^{mm'}$. Exactly for this reason instead of the relaxation time one should introduce the relaxation time tensor. Naturally, this changes the temperature and concentration dependences of the kinetic coefficients, their dependences on the magnetic field intensity and other external influence.

Scattering anisotropy in multi-valley semiconductors can be due to different reasons, namely scattering potential anisotropy (piezoelectric semiconductors, scattering on ions with dielectric constant anisotropy), phonon spectrum anisotropy, carrier energy spectrum anisotropy. In the latter case charge carrier scattering is described by a series of parameters, for instance, not by deformation potential constant (like in the case of isotropic scattering), but by the tensor of deformation potential constants, not by effective mass value, but by components of effective mass tensor, etc. Anisotropic scattering theory offers the possibility to find a dependence of experimentally measured values on the above parameters, which cannot be achieved through use of isotropic scattering theory.

Determination of the thermopower tensor

The Seebeck effect (or thermoelectric effect) discovered in 1823 consists in the origination in a semiconductor in the presence of temperature difference of electric field which in this case is called thermoelectric.

The generalized Ω law relating the tensors of current density vector $\vec{j}$ and electric field intensity $\vec{\varepsilon}$ in the presence of temperature gradient *grad* $T \equiv \nabla T$, for the anisotropic media can be written as [9]:

$$\vec{j} = \hat{\sigma}\vec{\varepsilon} - \hat{\sigma}\hat{\alpha}\nabla T, \tag{13}$$

where $\hat{\sigma}$ and $\hat{\alpha}$ are second-rank tensors of electric conductivity and thermopower, respectively. If we introduce notation

$$\hat{b} = \hat{\sigma}\hat{\alpha}, \tag{14}$$

Eq.(13) can be written as follows:

$$\vec{j} = \hat{\sigma}\vec{\varepsilon} - \hat{b}\nabla T, \tag{15}$$

or in components

$$j_i = \sigma_{ik}\varepsilon_k - b_{il}\nabla_l T, \tag{16}$$

where

$$b_{il} = \sigma_{im}\alpha_{ml}. \tag{17}$$

Thermoelectric field intensity is found in the absence of electric current. On entering $\vec{j} = 0$ into (13), we obtain the following expression for thermoelectric field intensity:

$$\vec{\varepsilon} = \hat{\alpha}\nabla T, \tag{18}$$

or in components

$$\varepsilon_i = \alpha_{ik}\nabla_k T. \tag{19}$$

Formula (18) giving a linear dependence of thermoelectric field intensity on temperature gradient is the first term of the expansion of $\vec{\varepsilon}$ in ∇T and defines thermoelectric effect in the framework of linear in ∇T theory, valid at low temperature gradients, when one can ignore expansion terms with higher powers.

Based on (14), the Seebeck coefficient tensor is determined as follows:

$$\hat{\alpha} = \hat{\sigma}^{-1}\,\hat{b}\,, \tag{20}$$

On the other hand, based on the kinetic theory, current density can be represented as

$$\vec{j} = e\int_0^{\infty} \psi_1(E)\,\vec{\upsilon}\; g(E_k)\,dE_k\,, \tag{21}$$

where e is electron charge, $\vec{\upsilon}$ is group carrier velocity, $g(E_k)$ is the density of states, E is full carrier energy, E_k is kinetic carrier density, ψ_1 is addition to equilibrium distribution function in the presence of disturbing fields, that is:

$$\psi = \psi_0 + \psi_1\,. \tag{22}$$

From the kinetic Boltzmann equation

$$\frac{\partial\psi}{\partial t} = \left(\frac{\partial\psi}{\partial t}\right)_{field} + \left(\frac{\partial\psi}{\partial t}\right)_{collision} \tag{23}$$

for the steady-state conditions and in the relaxation time approximation for ψ_1 (in conformity with [10]) we obtain

$$\psi_1 = -\tau\,\frac{\partial\psi_0}{\partial E}\left[\frac{\mu - E}{T}\,\nabla T - \nabla\left(\mu + eV\right)\vec{\upsilon}\right], \tag{24}$$

whereτ is relaxation time, μ is chemical potential, T is absolute temperature, V is electric potential. In formula (23) $\left(\frac{\partial\psi}{\partial t}\right)_{field}$ is a field term that defines the velocity of change in ψ distribution function as a result of continuous electron motion in normal (geometric) space and in velocity space, $\left(\frac{\partial\psi}{\partial t}\right)_{collision}$ is a collision term that defines the velocity of change in ψ as a result of electron collision (scattering).

Substituting (24) into (21) and comparing the resulting expression to formula (15) written for the isotropic case, when b and σ are scalars, we shall find their (b and σ), and on the basis of (20) in the isotropic case for the Seebeck coefficient we shall find the relationship:

$$\alpha = \frac{k_0}{e}\left[\frac{\int_0^{\infty}\tau(E_k)\,\frac{\partial\psi_0}{\partial E}\,E\;\vec{\upsilon}^2\;g(E_k)\,dE_k}{k_0 T\int_0^{\infty}\tau(E_k)\;\frac{\partial\psi_0}{\partial E}\;\vec{\upsilon}^2\;g(E_k)\,dE_k} - \mu^*\right], \tag{25}$$

or

$$\alpha = \frac{k_0}{e}\left[\frac{\iiint_{-\infty}^{\infty}\;\tau\;\frac{\partial\psi_0}{\partial E}\;E\;\vec{\upsilon}^2\,d^3\vec{k}}{k_0 T\iiint_{-\infty}^{\infty}\;\tau\;\frac{\partial\psi_0}{\partial E}\;\vec{\upsilon}^2\,d^3\vec{k}} - \mu^*\right], \tag{26}$$

where k_0 is the Boltzmann constant, $\mu^* = \frac{\mu}{k_0 T}$ is reduced chemical potential. In (26) integrals are taken over quasi-pulse space.

In the general case of nonspherical surfaces of charge carrier energy constant, the relaxation time is a second-rank tensor. Having written (15) and (21) in the main axes of the inverse effective

mass tensor, for the components of thermopower tensor of electrons belonging to one minimum we obtain the following expression:

$$\alpha_{ii} = \frac{k_0}{e}\left[\frac{\iiint_{-\infty}^{\infty} \tau_{ii}\,\frac{\partial\psi_0}{\partial E}\,E\,\upsilon_i^2\,d^3\vec{k}}{k_0\,T\iiint_{-\infty}^{\infty} \tau_{ii}\,\frac{\partial\psi_0}{\partial E}\,\upsilon_i^2\,d^3\vec{k}} - \mu^*\right]. \qquad (27)$$

Mechanisms of origination of thermopower anisotropy

The anisotropy of electric conductivity, thermal conductivity and a number of other physical properties is typical (to a varying degree) of all noncubic crystals. However, thermopower anisotropy is a rather rare phenomenon, as long as for its manifestation a series of specific conditions must be met. For the electric conductivity anisotropy, for instance, it is sufficient to have either anisotropic energy spectrum or anisotropic scattering law, or both.

The situation is different with thermopower anisotropy. According to anisotropic scattering theory based on the method for solution of kinetic equation [8], the effect of scattering anisotropy on the kinetic coefficients for such most common scattering mechanisms as scattering on acoustic and optical phonons, on the ionized and neutral impurities (dipoles), is taken into account by the relaxation time tensor given below:

$$\tau_{ii} = \lambda_{ii} E_k^r . \qquad (28)$$

In so doing, the tensor character of relaxation time is described by coefficients λ_{ii} that do not depend on energy, but are the functions of the effective mass anisotropy. Power exponent *r* depends on the type of charge carrier scattering in a crystal. At scattering on acoustic lattice vibrations and optical vibrations at higher than the Debye temperatures (θ) $r = -\frac{1}{2}$, at scattering on optical vibrations at $< \theta$ $r = 0$, at scattering on ionized impurities $r = \frac{3}{2}$.

On substituting (28) into (27), coefficient λ_{ii} will reduce, and for α_{ii} we obtain a scalar expression. Thus, if there is one type of charge carriers and one scattering mechanism, the thermopower will be isotropic, whatever strong is the anisotropy of charge carrier effective mass. This result was used by the authors of [11] in the consideration of a multi-valley model. It is acceptable both for the isotropic dispersion law $E\left(\vec{k}\right)$ and for the anisotropic parabolic and nonparabolic ellipsoidal law (the Kane model). Most likely, exactly this accounts for the fact that thermopower anisotropy is less common than the electric conductivity anisotropy.

If $E\left(k_i\right)$ is characterized by different dependence along different directions (nonparabolic and nonellipsoidal dispersion law), in this case (even with one type of carriers and one scattering mechanism) the thermopower anisotropy can be observed, as mentioned in [12].

It should be noted that at scattering on impurity ions the relaxation time in the form of (28) is some approximation. According to [8], coefficients λ_{ii}^u are energy dependent, this dependence being different for different directions in a crystal. On substituting (28) into (27), $\lambda_{ii}^u\left(E\right)$ in this case will not be reduced, and owing to the fact that that they are different for different directions, α_{ii} for

different *i* will differ from each other. That is, thermopower anisotropy will be observed in this case. This mechanism of thermopower anisotropy origination is typical of heavily doped semiconductors.

In the case of one type of carriers and two scattering mechanisms described by relaxation times $\tau_{ii}^{(1)} = \lambda_{ii}^{(1)} E^{r_1}$ and $\tau_{ii}^{(2)} = \lambda_{ii}^{(2)} E^{r_2}$, summation of inverse relaxation times will yield

$$\tau_{ii} = \frac{\lambda_{ii}^{(1)} \lambda_{ii}^{(2)} E^{r_1+r_2}}{\lambda_{ii}^{(1)} E^{r_1} + \lambda_{ii}^{(2)} E^{r_2}}. \tag{29}$$

Substitution of (29) into (27) will result in the expression

$$\alpha_{ii} = \frac{\int \frac{E^{r_1+r_2}}{\lambda_{ii}^{(1)} E^{r_1} + \lambda_{ii}^{(2)} E^{r_2}} \frac{\partial \psi_0}{\partial E} \upsilon_i^2 \left(E - \mu\right) d^3 \vec{k}}{eT \int \frac{E^{r_1+r_2}}{\lambda_{ii}^{(1)} E^{r_1} + \lambda_{ii}^{(2)} E^{r_2}} \frac{\partial \psi_0}{\partial E} \upsilon_i^2 \, d^3 \vec{k}}. \tag{30}$$

In this case the thermopower tensor does not reduce to a scalar and thermopower will be anisotropic. Thus, one of the reasons for origination of thermopower anisotropy can be the availability of two (or several) anisotropic scattering mechanisms. However, thermopower anisotropy caused by joint action of several scattering mechanisms is low and at scattering on phonons and ions, ions and dipoles, phonons, ions and dipoles is 0.1 ÷ 25.0 μV/degree.

Another reason for thermopower anisotropy can be the presence of two (or greater number) charge carrier types with one scattering mechanism, if at least one group of carriers is characterized by anisotropic electric conductivity and their partial Seebeck coefficients are different. This is due to the fact that thermopower, unlike electric conductivity, is not an additive value. Really, let us denote through $j_i^{(1)}$ and $j_i^{(2)}$ current densities of "1" and "2" type carriers and write for them the generalized Ohm's law (16):

$$\left.\begin{aligned} j_i^{(1)} &= \sigma_{ii}^{(1)} \varepsilon_i - b_{ii}^{(1)} \frac{\partial T}{\partial x_i}, \\ j_i^{(2)} &= \sigma_{ii}^{(2)} \varepsilon_i - b_{ii}^{2} \frac{\partial T}{\partial x_i}. \end{aligned}\right\} \tag{31}$$

Total current density equals:

$$j_i = j_i^{(1)} + j_i^{(2)} = \left(\sigma_{ii}^{(1)} + \sigma_{ii}^{(2)}\right) \varepsilon_i - \left(b_{ii}^{(1)} + b_{ii}^{(2)}\right) \frac{\partial T}{\partial x_i} = \sigma_{ii} \varepsilon_i - b_{ii} \frac{\partial T}{\partial x_i}. \tag{32}$$

From condition of $j_i = 0$ for the thermoelectric field we have the expression

$$\varepsilon_i = \frac{b_{ii}}{\sigma_{ii}} \frac{\partial T}{\partial x_i} = \frac{b_{ii}^{(1)} + b_{ii}^{(2)}}{\sigma_{ii}^{(1)} + \sigma_{ii}^{(2)}} \frac{\partial T}{\partial x_i}. \tag{33}$$

Whence for the thermopower tensor we shall have the relationship:

$$\alpha_{ii} = \frac{b_{ii}^{(1)} + b_{ii}^{(2)}}{\sigma_{ii}^{(1)} + \sigma_{ii}^{(2)}}. \tag{34}$$

On substituting b_{ii} based on (17) and taking into account that thermopower of one group of carriers with one scattering mechanism is isotropic, we finally obtain:

$$\alpha_{ii} = \frac{\alpha^{(1)}\sigma_{ii}^{(1)} + \alpha^{(2)}\sigma_{ii}^{(2)}}{\sigma_{ii}^{(1)} + \sigma_{ii}^{(2)}}, \tag{35}$$

and the difference in two components of the thermopower tensor $\hat{\alpha}$ in this case is expressed by the formula

$$\Delta\alpha = \alpha_{11} - \alpha_{22} = \frac{\left(\sigma_{11}^{(1)}\sigma_{22}^{(1)} - \sigma_{11}^{(2)}\sigma_{22}^{(2)}\right)\left(\alpha^{(1)} - \alpha^{(2)}\right)}{\left(\sigma_{11}^{(1)} + \sigma_{11}^{(2)}\right)\left(\sigma_{22}^{(1)} + \sigma_{22}^{(2)}\right)}. \tag{36}$$

Eq.(36) suggests that even with the isotropic partial Seebeck coefficients the thermopower of the entire semiconductor can be anisotropic, if the electric conductivity of each carrier type, or at least one of them, is of anisotropic nature. In so doing, naturally, partial thermopowers must be different. This mechanism of thermopower anisotropy is apparently realized in semiconductors of orthorhombic syngony *CdSb* and *ZnSb* and in pure *Bi* in the area of mixed conductivity. The value of $\Delta\alpha$ in this case can reach ~ 300 μV/degree.

Thermopower anisotropy caused by the presence of several groups of charge carriers with different thermoelectric properties and anisotropic electric conductivities can be artificially created by directional deformation of multi-valley semiconductors of *n -Ge* and *n -Si* type. Really, directional elastic deformation of such crystals (except for directions $\vec{X} \,//\, \vec{J} \,//\, [100]$ in *n -Ge* and $\vec{X} \,//\, \vec{J} \,//\, [111]$ in *n -Si*) will lead to inequality of energy minima [13] and redistribution of electrons between the minima. As long as the kinetic properties of electrons belonging to different valleys (energy minima) are now different because of their different population, and the electric conductivity of each of these groups is strongly anisotropic, according to (35) the thermopower of the entire crystal will become anisotropic. The emergence of particularly high anisotropy can be expected in the area of mixed conductivity, as long as uniaxial deformation of *Ge* and *Si* leads to removed degeneration of the zones of light and heavy holes at point $\vec{k} = 0$ of quasi-pulse space and to the emergence of considerable electric conductivity anisotropy of holes. Thus, uniaxial elastic deformation can cause the emergence of thermopower anisotropy even in materials which in the undeformed state are fully isotropic thermoelectrically.

There is another mechanism of thermopower anisotropy origination related to the manifestation of the electron-phonon drag effect. With the anisotropic nature of charge carrier energy spectrum, the phonon thermopower is anisotropic. In so doing, thermopower anisotropy can occur even with one type (variation) of carriers and one scattering mechanism, unlike the diffusion thermopower that has been analyzed above.

Conclusions

1. The ways of using anisotropic scattering theory for the analysis of the kinetic effects in the presence and absence of temperature gradient on *n -Ge* and *n -Si* crystals under study were considered.
2. Based on the use of the generalized Ohm's law the thermopower tensor was defined under crystal conditions $\nabla T \neq 0$.

3. The most important mechanisms of thermopower anisotropy origination were analyzed in detail, and emphasis was placed on the peculiarities of this anisotropy in multi-valley semiconductors (*n -Ge* and *n -Si*) with their directional (uniaxial) elastic deformation.

References

1. G.P.Gaidar, Mechanisms of Formation of the Anisotropy of Thermoelectric and Thermomagnetic Effects in Multi-Valley Semiconductors, *Physics and Chemistry of the Solid State* **14**(1), 7 – 20 (2013).
2. G.P.Gaidar, *Kinetics of Electron Processes in Si and Ge in Externally Applied Fields. Monograph* (Saarbrücken, Deutschland: LAP LAMBERT Academic Publishing, 2015), 268 p.
3. P.I.Baranskii, I.S.Buda, and V.V.Savyak, *Thermoelectric and Thermomagnetic Effects in Multi-Valley Semiconductors* (Naukova Dumka, Kyiv, 1992).
4. G.Gaidar, P.Baranskii, Optimization of the Thermoelectric Figure of Merit in the Transmutation-Doped and Ordinary *n* -Si Crystals, *Phys. Status Solidi A* **212**(10), 2146 – 2153 (2015).
5. L.I.Anatychuk, *Thermoelements and Thermoelectric Devices. Reference Book* (Kyiv: Naukova Dumka, 1979), 767 p.
6. L.I.Anatychuk, L.N.Vikhor, *Thermoelectricity, Vol. IV, Functionally-Graded Thermoelectric Materials* (Kyiv-Chernivtsi: Institute of Thermoelectricity, 2012), 180 p.
7. P.I. Baranskii, I.S. Buda, I.D. Dakhovsky, and V.V. Kolomoyets, *Electric and Galvanomagnetic Effects in Anisotropic Semiconductors* (Kyiv: Naukova Dumka, 1977), 270 p.
8. A.G.Samoilovich, I.S.Buda, and I.V.Dakhovsky, Theory of Anisotropic Scattering, *Semiconductors* 7(4), 859 (1973).
9. P.I.Baranskii, I.S.Buda and I.V.Dakhovskii, *Theory of Thermoelectric and Thermomagnetic Effects in Anisotropic Semiconductors* (Naukova Dumka, Kyiv, 1987)
10. A.I.Anselm, *Introduction to Theory of Semiconductors* (Nauka, Moscow, 1978), 616p.
11. A.G.Samoilovich, M.V.Nitsovich, and V.M.Nitsovich, On the Theory of Anisotropic Thermoelectric Power in Semiconductors, *Phys. Status Solidi B* **16**(2), 459 – 465 (1966).
12. V.I.Kaidanov, V.A.Tselischev, A.P.Usov, L.D.Dudkin, V.K.Voronov, and N.N.Trusova, Anisotropy of the Kinetic Coefficients in Chromium Disilicide, *Semiconductors* **4**(7), 1338 – 1345 (1970).
13. P.I.Baranskii. O.E.Belyayev, G.P.Gaidar, V.P.Klad'ko, and A.V.Kuchuk, *The Problems of Diagnostics of Real Semiconductor Crystals* (Kyiv:Naukova Dumka, 2014), 462 p.

Submitted 10.01.2016

V.A.Romaka[1,2], P.F.Rogl[3], L.P.Romaka[4], V.Ya.Krayovskyy[2], Yu.V.Stadnyk[4], D.Kaczorowski[5], A.M.Horyn[4]

[1]Ya. Pidstryhach Institute for Applied Problems of Mechanics and Mathematics, the National Academy of Sciences of Ukraine, 3-b, Naukova Str., Lviv, 79060, Ukraine;
[2]National University "Lvivska Politechnika", 12, S. Bandera Str., Lviv, 79013, Ukraine;
[3]Universität Wien, 42, Währinger Str., Wien, A-1090, Österreich;
[4]Ivan Franko National University of Lviv, 6, Kyryla and Mefodiya Str., Lviv, 79005, Ukraine;
[5]W. Trzebiatowski Institute of Low Temperature and Structure Research, Polish Academy of Sciences, 2, Okolna Str., Wroclaw, 50 – 422, Poland

RESEARCH ON THE FEATURES OF CONDUCTION MECHANISMS IN $Hf_{1-x}Tm_xNiSn$ THERMOELECTRIC MATERIAL

The crystal and electronic structures, the temperature and concentration dependencies of resistivity and the Seebeck coefficient of $Hf_{1-x}Tm_xNiSn$ thermoelectric material were studied in the range $T = 80 \div 400$ K, $x = 0.01 \div 0.30$. The mechanisms for the simultaneous generation in a crystal of the acceptor and donor structural defects which change the compensation ratio of semiconductor material and determine conduction mechanisms in $Hf_{1-x}Tm_xNiSn$ were established.
***Keywords**: electronic structure, resistivity, the Seebeck coefficient.*

Introduction

This paper presents the results of research on $Hf_{1-x}Tm_xNiSn$ thermoelectric material obtained by heavy doping of *n - HfNiSn* semiconductor with the atoms of rare-earth *Tm* metal introduced by *Hf* substitution. Doping was performed for optimization of thermoelectric material parameters in order to obtain maximum values of thermoelectric figure of merit Z ($Z = \alpha^2 \cdot \sigma/\kappa$, where α is the Seebeck coefficient, σ is electric conductivity, κ is thermal conductivity) [1]. This motivated a research on the effect of *Tm* doping impurity on the change in structural, energy and kinetic characteristics of $Hf_{1-x}Tm_xNiSn$ thermoelectric material that allowed revealing the features of its conduction mechanisms.

The interest in thermoelectric materials based on intermetallic semiconductors, in particular, *n - HfNiSn, n - ZrNiSn* and *n - TiNiSn*, is aroused by the high values of electric conductivity and the Seebeck coefficient [2, 3], as well as by reproducibility of characteristics up to $T \approx 1300$ K [4], assuring high efficiency of thermal into electric energy conversion in a wide temperature range. All the above mentioned makes intermetallic semiconductors one of the most extensively studied and promising thermoelectric materials [5 – 8].

Investigation procedures

The object to be investigated included crystalline structure, electronic density distribution (DOS), the electrokinetic and energy characteristics of $Hf_{1-x}Tm_xNiSn$. The samples were synthesized in the laboratory of Institute for Physical Chemistry, Vienna University. The X-ray structural

analysis (powder method) was used to obtain the data arrays (diffractometer Guinier-Huber image plate system, $CuK\alpha_1$), and Fullprof program [9] was employed for the calculation of structural characteristics. The chemical and phase compositions of the samples were controlled by microprobe analyzer (EPMA, energy-dispersive X-ray analyzer). The electronic structure calculations were performed by the Korringa-Kohn-Rostoker (KKR) method in coherent potential approximation (CPA) and local density approximation (LDA) [10] with the use of Moruzzi-Janak-Williams exchange-correlation potential [11]. The accuracy of calculating the position of the Fermi level ε_F is ± 8 meV. The temperature and concentration dependences of the electrical resistivity (ρ) and the Seebeck coefficient (α) were measured with respect to copper in the temperature range $T = 80 \div 400$ K, in the samples of $Hf_{1-x}Tm_xNiSn$, $x = 0.01 \div 0.10$ ($N_A^{Tm} \approx 1.9 \cdot 10^{20}$ см$^{-3} \div 1.9 \cdot 10^{21}$ см$^{-3}$).

Research on the crystalline and electronic structures of $Hf_{1-x}Tm_xNiSn$

A microprobe analysis of the concentration of atoms on the surface of $Hf_{1-x}Tm_xNiSn$, $x = 0 \div 0.10$, samples has shown their conformity to the initial charge compositions, and X-ray phase and structural analyses have revealed no traces of other phases in the samples. Refinement of $Hf_{1-x}Tm_xNiSn$ crystalline structure by the powder method has confirmed the result of [8] as regards crystal structure disorder of *n - HfNiSn*, the key point of which lies in a partial, up to ~1%, occupancy by *Ni* atoms of the crystallographic position 4*a* of *Hf* atoms, and the semiconductor formula can be written as $(Hf_{1-y}Ni_y)NiSn$, $y \le 0.01$. If it is remembered that *Ni* ($3d^8 4s^2$) atom possesses a larger number of *d*-electrons than *Hf* ($5d^2 6s^2$) atom, a structural defect of the donor nature is created in a crystal ("a priori" doping with donors [3]), and electrons are the majority carriers.

On the other hand, crystalline structure refinement of $Hf_{1-x}Tm_xNiSn$, $x = 0.01 \div 0.10$, samples has shown that introduction of *Tm* atoms puts into order crystalline structure ("heals" structural defects), and *Ni* atoms leave the position of *Hf* (4*a*) atoms. Ordering of $Hf_{1-x}Tm_xNiSn$ structure makes it resistant, and the kinetic characteristics become reproducible during thermocycling. Besides, ordering contributes to the redistribution of the electronic density of states. If in *n - HfNiSn* there exist structural defects of the donor nature as a result of displacement of up to ~1% of *Hf* atoms by *Ni* atoms [8], then ordering of $Hf_{1-x}Tm_xNiSn$ structure is accompanied by the reduction in the number of donors, as long as *Ni* atoms leave the position of *Hf* atoms. On the other hand, as long as *Tm* ($4f^{13}5d^0 6s^2$) atom has two 5*d* – electrons less than *Hf* atom, structural defects of the acceptor nature are generated in the crystal.

Thus, in $Hf_{1-x}Tm_xNiSn$, $x = 0 \div 0.01$, there is a simultaneous reduction of the number of donors (*Ni* atoms leave position 4*a* of *Hf* atoms) and increase in the number of acceptors (*Tm* atoms occupy the position of *Hf* atoms). In this case, doping of n - *HfNiSn* semiconductor with the lowest concentrations of acceptor impurity ($0 < x \le 0.02$) will increase the compensation ratio (the ratio between donors and acceptors) [3, 12]. With concentrations of $x > 0.01$, when *Ni* atoms will leave position 4*a* of *Hf* atoms, the concentration of acceptors in a crystal will increase, the type of majority carriers must change and the compensation ratio will decrease. [2, 3].

The electronic structure of $Hf_{1-x}Tm_xNiSn$, $x = 0 \div 0.01$, was calculated for simulation of electric conductivity mechanisms, the Fermi level behaviour, the energy gap of semiconductor. As long as doping of *n - HfNiSn* with *Tm* atoms puts into order crystalline structure, calculation of the electronic density of states was done for the case of ordered structure version (Fig. 1*a*).

On introducing into *n-HfNiSn* of minimum attainable in experiment concentrations of *Tm* impurity, the Fermi level ε_F starts drifting from the conduction band ε_C, spaced ~ 81.3 meV from it [8], to the midgap ε_g (dashed line in Fig. 1*a*) at $x \approx 0.02$ and then to the valence band, to cross it at $x \approx 0.04$.

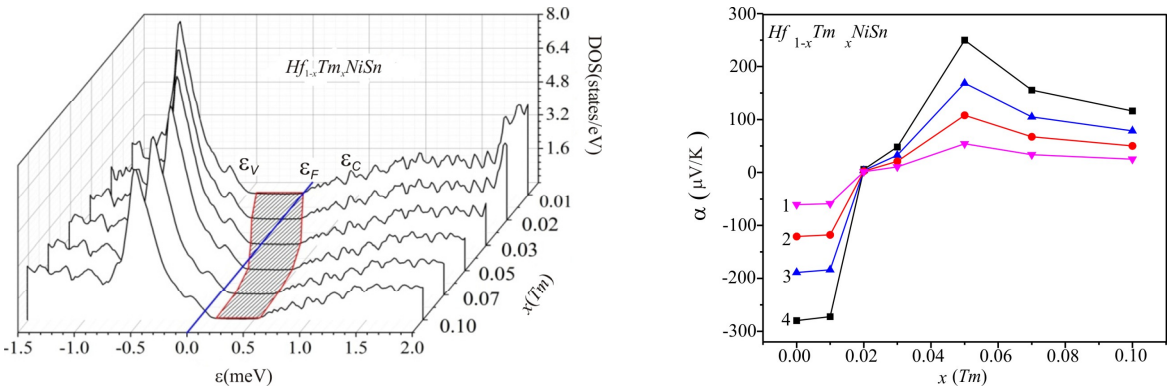

Fig. 1. Calculation of the electronic density of states DOS (a) and a change in the values of the Seebeck coefficient (b) of $Hf_{1-x}Tm_xNiSn$ at the temperatures: 1 – 80; 2 – 160; 3 – 250; 4 – 380 K

The drift of ε_F from the conduction band edge ε_C to the valence band ε_V also means a change in the ratio of $Hf_{1-x}Tm_xNiSn$ majority carriers. Thus, for the concentrations of $Hf_{1-x}Tm_xNiSn$, $x < 0.02$, when the Fermi level ε_F is between the conduction band ε_C and the midgap ε_g, electrons are the majority carriers. Conversely, at $x > 0.02$ and right up to crossing by the Fermi level of the valence band, holes are the majority carriers. Besides, crossing of the valence band by the Fermi level ε_F will also cause a change from the activation to metal conduction mechanism (the dielectric-metal transition which is referred to as the Anderson transition [12]).

Calculation of $Hf_{1-x}Tm_xNiSn$ electronic structure allows predicting the kinetic characteristics of thermoelectric material, in particular, the behaviour of the Seebeck coefficient $\alpha(x,T)$ at different temperatures (Fig. 1*b*). Below is given the working formula used for the calculation of $\alpha(x,T)$ [12]:

$$\alpha(x,T) = \frac{2\pi^2}{3}\frac{k_B^2 T}{e}\left(\frac{d}{d\varepsilon}\ln g(\varepsilon_F)\right),$$

where $g(\varepsilon_F)$ is density of states at the Fermi level. From Fig. 1*b* it is seen that at different concentrations of *Tm* one can obtain in thermoelectric material high values of the Seebeck coefficient of both signs, as well as of the electric conductivity, assuring high values of thermoelectric figure of merit [1].

Thus, the results of calculation of the electronic density of states of $Hf_{1-x}Tm_xNiSn$, based on structural research data, prove only the acceptor nature of structural defects generated in a crystal. The results of research on the kinetic characteristics of $Hf_{1-x}Tm_xNiSn$ will show the degree of conformity of such calculations to real processes occurring in material.

Research on the electrokinetic and energy characteristics of $Hf_{1-x}Tm_xNiSn$

The temperature dependences of resistivity $\ln\rho(1/T)$ and the Seebeck coefficient $\alpha(1/T)$ for $Hf_{1-x}Tm_xNiSn$, $x = 0 \div 0.10$, presented in Fig. 2, are typical for heavily doped and compensated semiconductors with several activation areas, which is indicative of several conduction mechanisms [12]. From the high-temperature activation areas of $\ln\rho(1/T)$ dependences the activation energy from the Fermi level ε_F to the bands of continuous energies ε_1^ρ was calculated, and from the same

$\alpha(1/T)$ dependences – the activation energies ε_1^{α} yielding the value of modulation amplitude of continuous energy bands for heavily doped compensated semiconductors [3, 12].

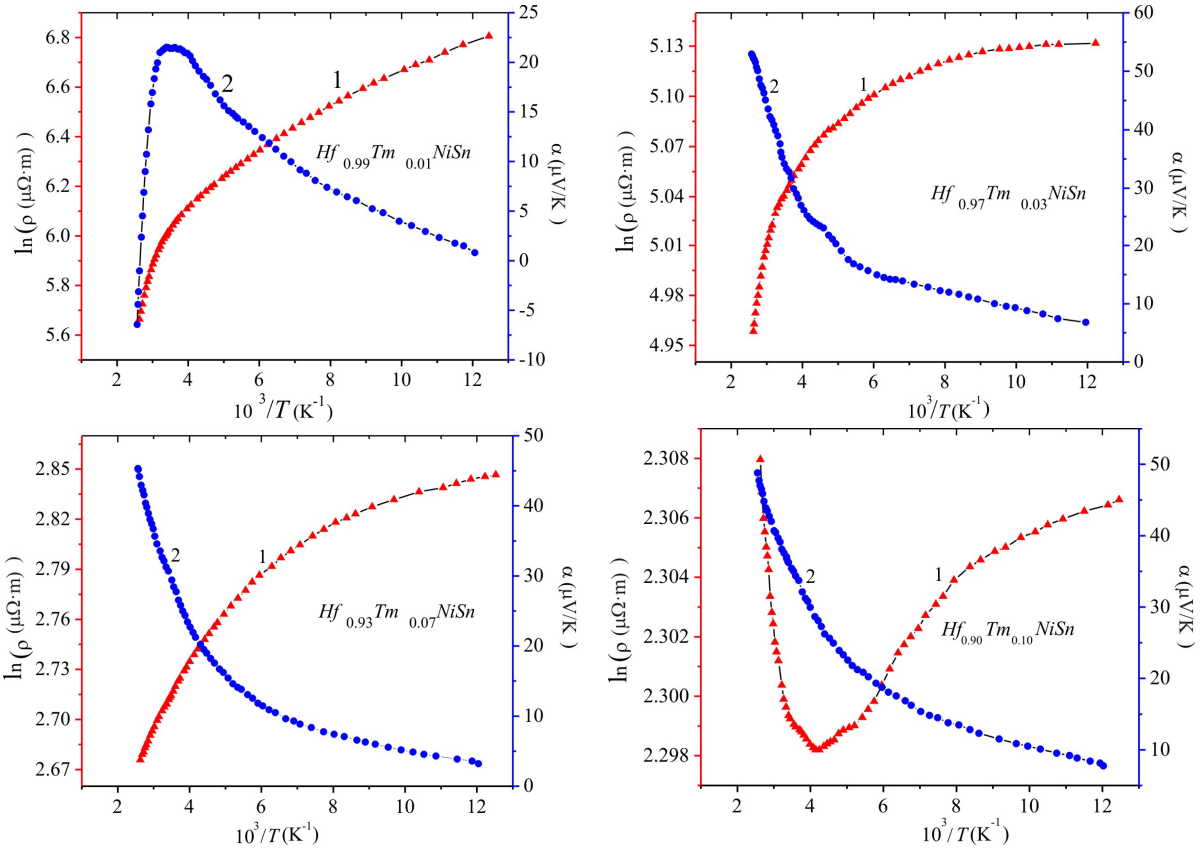

Fig. 2. Temperature dependences of the electric resistivity and the Seebeck coefficient of $Hf_{1-x}Tm_xNiSn$

The presence on the dependences $\ln\rho(1/T)$ for $Hf_{1-x}Tm_xNiSn$, $x = 0 \div 0.07$, of high-temperature activation areas points to the arrangement of the Fermi level ε_F in the energy gap. The result obtained contradicts to the results of calculations of DOS (Fig. 1*a*) which predicted crossing by the Fermi level ε_F of the valence band at concentration *Tm* $x \approx 0.04$ and the dielectric-metal conduction transition [12].For $Hf_{1-x}Tm_xNiSn$, $x = 0.10$ the activation area on $\ln\rho(1/T)$ is present only at low temperatures, pointing to hopping conduction mechanism in the impurity acceptor band.

The negative values of the Seebeck coefficient of *n - HfNiSn* are understandable and related to "a priori doping" of base *n - HfNiSn* semiconductor with donors (position of *Hf* atoms up to ~1% is occupied with *Ni* atoms) [8]. Whereas in the sample of $Hf_{1-x}Tm_xNiSn$, $x = 0.01$, the concentration of *Tm* acceptor impurity corresponds to concentration of donors available in *n - HfNiSn* ("a priori doping" [3]) and the state close to full compensation is realized, when the Fermi level must be located near the midgap ε_g. Thus, the positive values of the Seebeck coefficient at low temperatures (Fig. 2, 3) indicate that concentration of generated acceptors with substitution of *Hf* atoms by *Tm* atoms exceeds the number of defects caused by disordered structure of *HfNiSn*, hence the Fermi level ε_F is fixed by impurity acceptor band (close to the valence band). However, at $T = 380$ K the sign of the Seebeck coefficient of $Hf_{1-x}Tm_xNiSn$, $x = 0.01$ (Fig. 3*b*) remains negative: $\alpha(x = 0.01) = -3.13$ μVK^{-1}. Obviously, the number of ionized donors and acceptors changes with temperature [13]. An extreme point on $\alpha(1/T)$ dependence for the sample of $Hf_{1-x}Tm_xNiSn$, $x = 0.01$, at $T \approx 270$ K reflects

crossing by the Fermi level of the midgap and a drift back to conduction band. It turns out that in $Hf_{1-x}Tm_xNiSn$, $x = 0.01$, the concentration of donors exceeds that of acceptors, though they have to be equal. It can be assumed that donors are also generated in a crystal by the mechanism which is yet unknown.

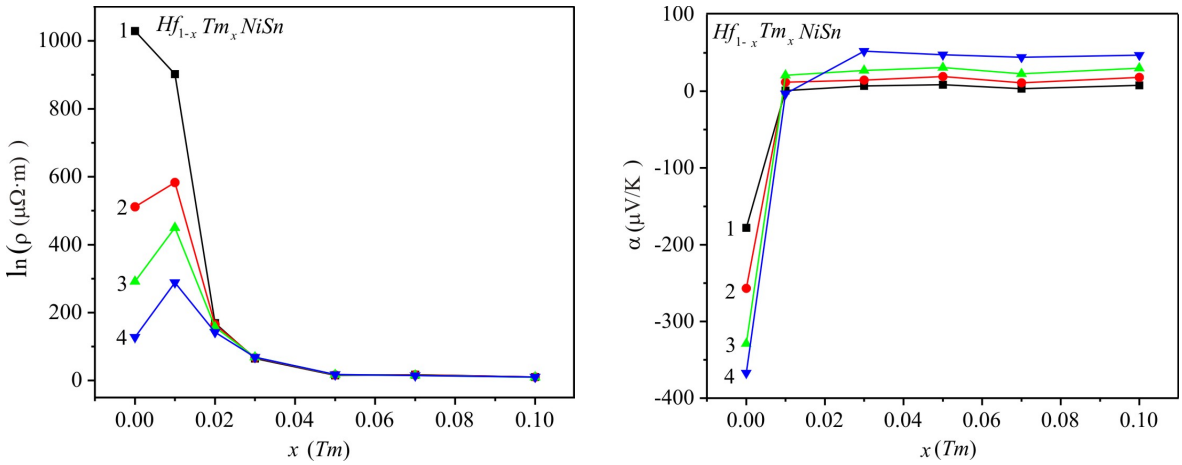

Fig. 3. Change in the values of electric resistivity $\rho(x)$ *(a) and the Seebeck coefficient* $\alpha(x)$ *(b) of* $Hf_{1-x}Tm_xNiSn$ *at the temperatures: 1 – 80; 2 – 160; 3 – 250; 4 – 380 K*

From the character of change in the values of resistivity $\rho(x)$ $Hf_{1-x}Tm_xNiSn$, $x = 0 \div 0.01$, at different temperatures (Fig. 3*a*) one can see the above described structural feature of semiconductor which accounts for a simultaneous reduction of free electrons by two mechanisms: (1) – decreasing the number of donors, when *Ni* atoms leave position 4*a* of *Hf* atoms("healing" of donor-nature defects) and (2) – freezing out of free electrons to acceptor band generated at occupation by *Tm* atoms of the position of *Hf* atoms. Thus, introduction of the lowest concentration of *Tm* ($x = 0.01$) at the temperature of 80 K is accompanied by a reduction in the electric resistivity values from $\rho(x=0) = 1029.1$ μΩ·m до $\rho(x=0.01) = 902.32$ μΩ·m and $\rho(x=0.03) = 169.31$ μΩ·m. With a lower concentration of introduced acceptors or a larger concentration of free electrons we would have observed growth of $\rho(x)$ values due to a reduction in the number of free electrons in *n* - type semiconductor at doping with acceptors. We however immediately get a *p* - type semiconductor. On the other hand, a maximum on dependence $\rho(x)$ of $Hf_{1-x}Tm_xNiSn$, $x \geq 0.01$, at temperatures $T \geq 160$ K (Fig. 3*a*) shows that the Fermi level ε_F drifts to the midgap ε_g, which is accompanied by a reduction in the number of free electrons by the hitherto unknown mechanism that changes the semiconductor compensation ratio.

For the cases of $Hf_{1-x}Tm_xNiSn$, $x = 0.02 \div 0.10$, the positive values of the Seebeck coefficient at low temperatures indicate that the concentration of acceptor defects generated in a crystal is greater than that of donor defects, and the Fermi level ε_F is fixed on the impurity acceptor band. The proof of the fact that the Fermi level ε_F drifts in the direction of $Hf_{1-x}Tm_xNiSn$ valence band is the behaviour of the Seebeck coefficient $\alpha(x)$ (Fig. 3*b*). Thus, the Seebeck coefficient at 80 K changes from the values of $\alpha(x=0) = -178.1$ μVK^{-1} to $\alpha(x=0.01) = 0.82$ μVK^{-1} and $\alpha(x=0.03) = 6.82$ μVK^{-1}, which testifies to a change in the type of majority carriers from electrons, at $x = 0$, to holes, at $x \geq 0.01$.

Now, the high-temperature activation area on dependences $\ln\rho(1/T)$ of $Hf_{1-x}Tm_xNiSn$, $x = 0.02 \div 0.10$ (Fig. 2) is a manifestation of thermal flow of holes from the Fermi level which is fixed by acceptor band to the valence band, increasing the number of free holes. Instead, the

metallic dependence $\ln\rho(1/T)$ at high temperatures and the positive values of the Seebeck coefficient for $Hf_{1-x}Tm_xNiSn$, $x = 0.10$, testify that the Fermi level ε_F has crossed the valence band ceiling, i.e. the dielectric–metal conduction transition has taken place [12]. In so doing, at $T < 250$ K, the hopping conduction mechanism shows that the Fermi level ε_F leaves the valence band for the energy gap. This is possible only on condition of donors appearing in a semiconductor by the hitherto unknown mechanism which compensate the introduced acceptors and force the Fermi level ε_F to leave the valence band.

In this context it is interesting to trace the character of change in the energy characteristics of $Hf_{1-x}Tm_xNiSn$ obtained from the experimental investigations. From Fig. 4 it is seen that in $Hf_{1-x}Tm_xNiSn$ with increasing concentration of acceptors there is a reduction in the values of activation energy $\varepsilon_1^{\rho}(x)$. It is important to explain that the value of energy $\varepsilon_1^{\rho}(x)$ for the undoped semiconductor *n-HfNiSn* represents the energy gap between the position of the Fermi level ε_F and the conduction band edge. At the same time, the values of activation energy $\varepsilon_1^{\rho}(x)$ for the lowest and all subsequent concentrations of *Tm* atoms represent the energy gap between ε_F and the valence band edge. The fact that the value of activation energy $\varepsilon_1^{\rho}(x=0)$ falls on dependence $\varepsilon_1^{\rho}(x)$ is quite accidental.

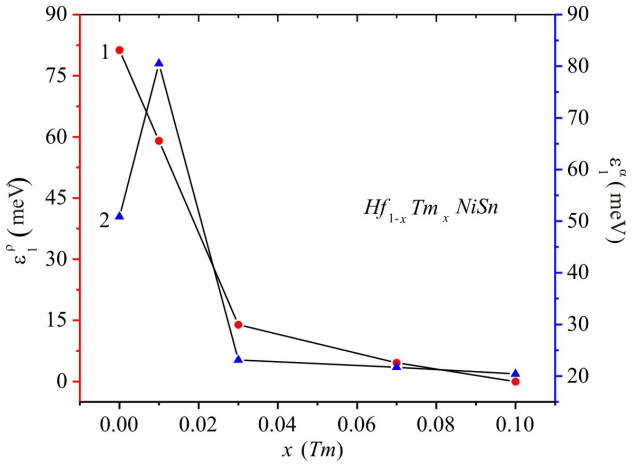

Fig. 4. Change in the values of activation energy $\varepsilon_1^{\rho}(x)$ (1) and $\varepsilon_1^{\alpha}(x)$ (2) of $Hf_{1-x}Tm_xNiSn$

An assumption of the simultaneous generation in $Hf_{1-x}Tm_xNiSn$, in addition to acceptors, of unknown structural defects of the donor nature is substantiated when analyzing the drift rate of the Fermi level. If we compare the drift rate of the Fermi level ε_F to the valence band, obtained both from the calculations of DOS (Fig. 1*a*), when only acceptor structural defects are generated in a crystal, and from the experimental investigations (Fig. 4), in the experiment it is less by a factor of ~ 2.5. What might "impede" this drift?

As long as the position of the Fermi level ε_F determines the ratio between donors and acceptors (compensation ratio), an obvious conclusion offers itself again that in $Hf_{1-x}Tm_xNiSn$ not only acceptor structural defects are generated, but also donors of unknown mechanism which "impede" the drift of the Fermi level ε_F towards the valence band.

Moreover, from the behaviour of $\varepsilon_1^{\rho}(x)$ (Fig. 4) it is obvious that in the area of *Tm* impurity concentration $x = 0 \div 0.03$ the drift rate of the Fermi level ε_F to the valence band edge is $\Delta\varepsilon_F / \Delta x = 22.6$ meV/% *Tm*, and in the area of $x = 0.03 \div 0.10$ – $\Delta\varepsilon_F / \Delta x = 2.3$ meV/% *Tm*.

At first sight, the result obtained seems to be illogical. As long as the concentration of *Tm* acceptor impurity is increased according to linear law, structural defects of the acceptor nature would have to be generated in a crystal in similar fashion. In such a case, why the Fermi level does not drift to the valence band edge according to the same law? What is it that again "impedes" this motion, reducing the drift rate of the Fermi level ε_F? This can occur only on condition when in $Hf_{1-x}Tm_xNiSn$, in addition to acceptors, there are donors generated by unknown mechanism, their generation rate increasing with *Tm* concentration growth.

The simultaneous generation in a crystal of the donor and acceptor structural defects with different rate is accompanied by a change in the compensation ratio, as well a change in the modulation amplitude of continuous energy bands of heavily doped compensated semiconductors [3, 12] according to the law reflecting the ratio between ionized acceptors and donors. Fig. 4 shows a change in the values of activation energy $\varepsilon_1^{\alpha}(x)$, proportional to the modulation amplitude of continuous energy bands of $Hf_{1-x}Tm_xNiSn$. It can be seen that in the case of *n* - *HfNiSn* the modulation amplitude is $\varepsilon_1^{\alpha}(x=0)=50.9$ meV. Introduction into *n*-type semiconductor of the least in the experiment concentration of *Tm* impurity corresponding to composition $x = 0.01$, is accompanied by a drastic increase in the compensation ratio, as indicated by the modulation amplitude $\varepsilon_1^{\alpha}(x=0.01)=80.5$ meV. Moreover, at concentration $x = 0.01$ the type of semiconductor conduction is changed, i.e. holes become the majority carriers.

Doping of now semiconductor *p* - $Hf_{1-x}Tm_xNiSn$, $x = 0.01$ with *Tm* acceptor impurity reduces the compensation degree, that is, the difference in the number of ionized acceptors and donors will increase, which is manifested in the reduction of modulation amplitude values $\varepsilon_1^{\alpha}(x=0.03)=23.1$ meV, and on the dependence $\varepsilon_1^{\alpha}(x)$ there will appear a maximum. It is clear that further doping of *p*-type semiconductor with acceptor impurity will only reduce the compensation ratio, and the values of modulation amplitude of continuous energy bands will be reduced as well (Fig. 4). Taking into account that in experiment the concentration of acceptors is linearly increased in a semiconductor where holes are majority carriers, it would be logical to expect the same reduction in the modulation amplitude values of $Hf_{1-x}Tm_xNiSn$ continuous energy bands. However, a change in the values of dependence $\varepsilon_1^{\alpha}(x)$ (Fig. 4) for the cases of $x > 0.01$ reminds a change in the values of $\varepsilon_1^{\rho}(x)$, which can testify to the simultaneous generation in a crystal of acceptors and donors by unknown mechanism.

Thus, the results of kinetic investigations of $Hf_{1-x}Tm_xNiSn$ enable us to speak of a complicated mechanism for the simultaneous generation in a crystal of the acceptor and donor structural defects on introducing the atoms of rare-earth *Tm* metal into the structure of *HfNiSn* compound by substitution of *Hf* atoms. Note that no such defects have been revealed by structural investigations, as long as their concentration is beyond the accuracy of X-ray investigation methods.

For the identification of defects that determine conduction mechanism of $Hf_{1-x}Tm_xNiSn$ thermoelectric material, the following method proposed in [3] was employed. The electronic structure of $Hf_{1-x}Tm_xNiSn$ was calculated for different variants of atoms arrangement in the unit cell sites and for a different degree of occupancy of crystallographic positions of all atoms by proper or foreign atoms. In so doing, the drift rate of the Fermi level ε_F was "tied" to the numerical values of activation energy ε_1^{ρ} from the Fermi level ε_F to the valence band edge of $Hf_{1-x}Tm_xNiSn$, and the compensation ratio was sought for to assure the experimentally established drift rate of the Fermi level (Fig. 4, curve 1). It turned out that the most acceptable version of atoms arrangement provides

for the emergence of vacancies in position (4*b*) of *Sn* atoms, whose concentration grows with increase in the number of *Tm* atoms. Based on the new results of the spatial arrangement of atoms in $Hf_{1-x}Tm_xNiSn$ crystalline structure, more refined calculations were made of the electronic density of states distribution and, specifically, the density of states at the Fermi level $g(\varepsilon_F)$, as well as the Seebeck coefficient at different temperatures (Fig. 5) that are in complete agreement with the results of experimental investigations.

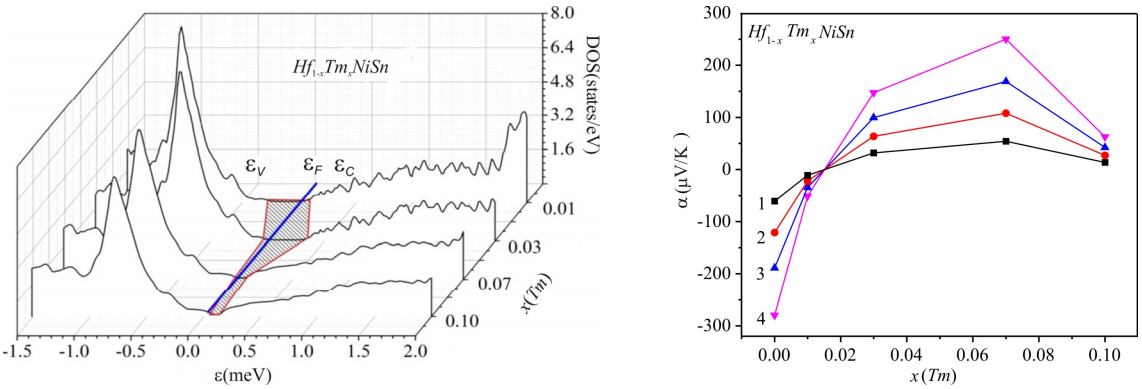

Fig. 5. Refined calculation of the electronic density of states DOS (a) and a change in the values of the Seebeck coefficient (b) of $Hf_{1-x}Tm_xNiSn$ at the temperatures: 1 – 80; 2 – 160; 3 – 250; 4 – 380 K

Conclusions

Thus, as a result of integrated research on the structural, energy and kinetic characteristics of *n* - *HfNiSn* intermetallic semiconductor heavily doped with the atoms of rare-earth *Tm* metal, the mechanisms for the simultaneous generation in a crystal of structural defects of the acceptor and donor nature have been revealed that change the compensation ratio of thermoelectric material and determine the electric conduction mechanisms.

The work was performed in the framework of grants of the National Academy of Sciences and Ministry of Education and Science of Ukraine, № 0113U007687 and № 0114U005464.

References

1. L.I.Anatychuk, *Thermoelements and Thermoelectric Devices* (Kyiv: Naukova Dumka, 1979), 768 p.
2. V.A.Romaka, P.Rogl, V.V.Romaka, D.Kaczorowski, Yu.V.Stadnyk, R.O.Korzh, V.Ya.Krajovskii, and T.M.Kovbasyuk, Features of the Band Structure and Conduction Mechanisms of *n* - HfNiSn Semiconductor Heavily Lu-Doped, *Semiconductors* **49**(3), 290 – 297 (2014).
3. V.V.Romaka, L.P.Romaka, V.Ya.Krajovskii., and Yu.V.Stadnyk, *Rare-Earth and Transient Metal Stannides* (Lviv:Lvivska Polytechnika, 2015), 224 p.
4. V.A.Romaka, V.V.Romaka, and Yu.V.Stadnyk, *Intermetallic Semiconductors: Properties and Application* (Lviv:Lvivska Polytechnika, 2011), 488 p.
5. T.M.Tritt, M.A.Sabramanian, Thermoelectric Materials, Phenomena, and Applications: A Bird's Eye View, *MRS Bulletin* **31**(3), 188 – 198 (2006).
6. G.S.Nolas, J.Poon, and M.Kanatzidis, Recent Developments in Bulk Thermoelectric Materials, MRS Bulletin **31**(3), 199 – 205 (2006).
7. S.R.Culp, S.J.Poon, N.Hickman, T.M.Tritt, and J.Blumm, Effect of Substitutions on the

Thermoelectric Figure of Merit of Half-Heusler Phases at 800^0 C, *Appl. Phys. Letters* **88**(16), 042106 – 1 – 3 (2006).

8. V.V.Romaka, P.Rogl, L.Romaka, Yu.Stadnyk, A.Grytsiv, O.Lakh, and V.Krayovsky, Peculiarites of Structural disorder in Zr- and Hf- Containing Heusler and Half-Heusler Stannides, *Intermetallics* 35, 45 – 52 (2013).
9. T.Roisnel, J.Rodriguez-Carvajal, WinPLOTR: a Windows Tool for Powder Diffraction Patterns Analysis, *Mater. Sci. Forum, Proc. EPDIC7* 378-381, 118 – 123 (2001).
10. M.Schruter, H.Ebert, H.Akai, P.Entel, E.Hoffmann, and G.G.Reddy, First-Principles Investigations of Atomic Disorder Effects on Magnetic and Structural Instabilities in Transition-Metal Alloys, *Phys. Rev. B* **52**, 188 – 209 (1995).
11. V.L.Moruzzi, J.F.Janak, and A.R.Williams, *Calculated Electronic Properties of Metals* (NY: Pergamon Press, 1978), 348 p.
12. B.I.Shklovsky, *Electron Properties of Doped Semiconductors* (Moscow: Nauka, 1979), 416 p.

Submitted 27.12.2015.

L.I.Anatychuk[1,2], A.V.Prybyla[1]

[1]Institute of Thermoelectricity of the
NAS and MES of Ukraine, 1, Nauky str.,
Chernivtsi, 58029, Ukraine
[2]Yu. Fedkovych Chernivtsi National University, 2,
Kotsyubinsky str., Chernivtsi, 58000, Ukraine

L.I. Anatychuk

A.V. Prybyla

OPTIMIZATION OF POWER SUPPLY SYSTEM OF THERMOELECTRIC LIQUID-LIQUID HEAT PUMP

The paper presents the results of computer simulation of liquid-liquid thermoelectric heat pump. The most rational variants of power supply to heat pump have been considered. Multi-parameter computer optimization has been used to determine parameters of power supply system of thermoelectric heat pump making possible to increase its heating coeffciient by 15%.

Key words: thermoelectric heat pump, computer simulation, water recovery system.

Introduction

General characterization of the problem. The use of thermoelectric heat pumps (THP) in air and liquid conditioning systems, special-purpose evaporators is related to their unique properties [1 – 5].

An example of efficient application of thermoelectric heat pumps is provided by systems of water recovery from liquid biowaste on board of manned spacecrafts (urine, atmosphere humidity condensate, sanitary-hygiene water) [4, 5].

Paper [8] presents the results of computer simulation of liquid-liquid thermoelectric heat pump. Multi - parameter computer optimization has been used to determine design parameters of the arrangement of thermoelectric modules and heat exchangers of thermoelectric heat pump. The next step of this work is computer optimization of the parameters of power supply system of thermoelectric heat pump, making possible its further efficiency increase.

The purpose of this work is to increase the efficiency of power supply system of thermoelectric heat pump by means of multiparameter computer simulation and optimization.

Physical model of THP

A physical model of thermoelectric heat pump is represented in Fig. 1. It comprises a liquid heat exchange system assuring passage of heat flux Q_c through the cold side of thermoelectric modules *1*, thermoelectric modules *2* consisting of semiconductor n - and p – type legs and a liquid heat exchange system *3* assuring passage of heat flux Q_h through their hot side.

Heat carrier (urine, atmospheric humidity condensate, sanitary-hygiene water) circulates in liquid heat exchange system at a rate of G ml/s. Two variants of heat carrier connection were considered. In the first case heat carriers in the hot *3* and cold *1* heat exchange system move in the same direction (1.1 → 1.2; 2.1 → 2.2), and in the second case – opposite to each other (1.1 →1.2; 2.2 → 2.1).

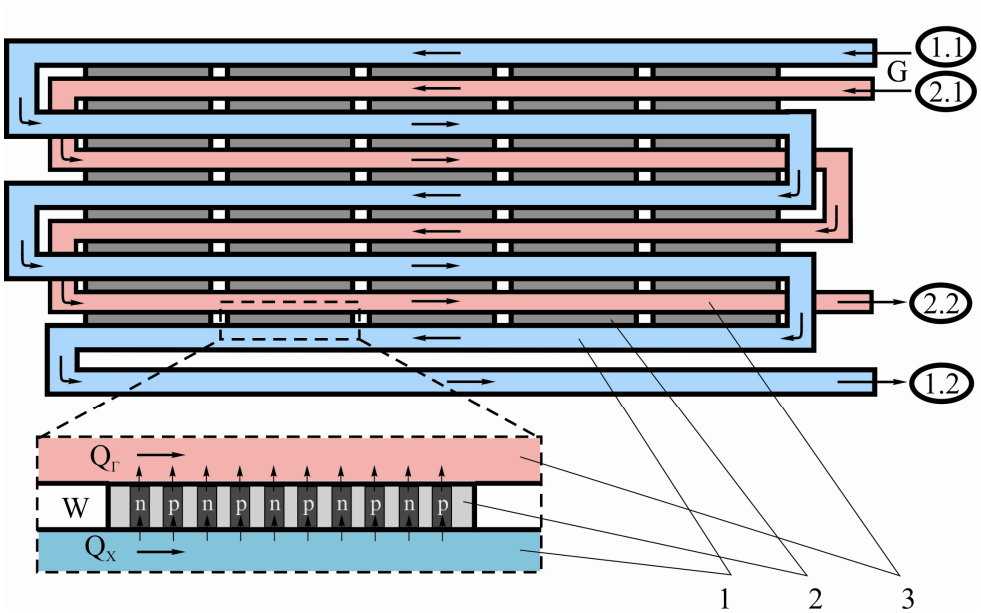

Fig. 1. Physical model of thermoelectric heat pump.

Moreover, various variants of power supply W to thermoelectric modules 2 were considered:
1) all the modules are powered by the same current and voltage, optimal for the entire heat pump;
2) the modules are grouped into sections with individually optimized power supply;
3) power supply to all thermoelectric modules is done individually.

Mathematical and computer description of the model

To describe heat and current fluxes, let us use the laws of conservation of energy

$$div\vec{E} = 0 \tag{1}$$

and electric charge

$$div\vec{\mathrm{j}} = 0, \tag{2}$$

where

$$\vec{E} = \vec{q} + U\vec{\mathrm{j}}, \tag{3}$$

$$\vec{q} = \kappa\nabla T + \alpha T\vec{j}, \tag{4}$$

$$\vec{\mathrm{j}} = -\sigma\nabla U - \sigma\alpha\nabla T. \tag{5}$$

Here $\vec{E}$ is energy flux density, $\vec{q}$ is thermal flux density, $\vec{j}$ is electric current density, U is electric potential, T is temperature, α, σ, κ are the Seebeck coefficient, electric conductivity and thermal conductivity.
With regard to (3) – (5), one can obtain

$$\vec{E} = -(\kappa + \alpha^2\sigma T + \alpha U\sigma)\nabla T - (\alpha\sigma T + U\sigma)\nabla U. \tag{6}$$

Then the laws of conservation (1), (2) will acquire the form:

$$-\nabla\left[(\kappa + \alpha^2\sigma T + \alpha U\sigma)\nabla T\right] - \nabla\left[(\alpha\sigma T + U\sigma)\nabla U\right] = 0, \tag{7}$$

$$-\nabla(\sigma\alpha\nabla T) - \nabla(\sigma\nabla U) = 0. \tag{8}$$

These nonlinear differential equations of second order in partial derivatives (7) and (8) determine the distribution of temperature T and potential U in thermoelements.

An equation describing the process of heat transport in the walls of heat exchangers in the

steady-state case is written as follows:

$$\nabla(-k_1 \cdot \nabla T_1) = Q_1, \tag{9}$$

where k_1 is thermal conductivity of heat exchanger walls, ∇T_1 is temperature gradient, Q_1 is heat flux.

The processes of heat-and-mass transfer in heat exchanger channels in the steady-state case are described by equations [9]

$$-\Delta p - f_D \frac{\rho}{2d_h} v|\vec{v}| + \vec{F} = 0, \tag{10}$$

$$\nabla(A\rho\vec{v}) = 0, \tag{11}$$

$$\rho A C_p \vec{v} \cdot \nabla T_2 = \nabla \cdot A k_2 \nabla T_2 + f_D \frac{\rho A}{d_h} |\vec{v}|^3 + Q_2 + Q_{wall}, \tag{12}$$

where p is pressure, ρ is heat carrier density, A is cross-section of the tube, $\vec{F}$ is the sum of all forces, C_p is heat carrier heat capacity, T_2 is temperature, $\vec{v}$ is velocity vector, k_2 is heat carrier thermal conductivity, f_D is the Darcy coefficient, $d = \frac{4A}{Z}$ is effective diameter, Z is perimeter of tube wall, Q_2 is heat which is released due to viscous friction [W/m] (from the unit length of heat exchanger), Q_{wall} is heat flux coming from the heat carrier to tube walls [W/m]

$$Q_{wall} = h \cdot Z \cdot (T_1 - T_2), \tag{13}$$

where h is heat exchange coefficient which is found from equation

$$h = \frac{Nu \cdot k_2}{d}. \tag{14}$$

The Nusselt number is determined with the use of the Gnielinski equation ($3000 < Re < 6 \cdot 10^6$, $0.5 < Pr < 2000$)

$$Nu = \frac{\left(\frac{f_d}{8}\right)(Re - 1000)Pr}{1 + 12.7\left(\frac{f_d}{8}\right)^{\frac{1}{2}}\left(Pr^{\frac{2}{3}} - 1\right)}, \tag{15}$$

where $Pr = \frac{C_p \mu}{k_2}$ is the Prandtl number, μ is dynamic viscosity, $Re = \frac{\rho v d}{\mu}$ is the Reynolds number.

To determine the Darcy coefficient f_D we will use the Churchill equation for the entire spectrum of the Reynolds number and all values of e / d (e is roughness of wall surface)

$$f_D = 8\left[\left(\frac{8}{Re}\right)^{12} + (A + B)^{-1.5}\right]^{1/12}, \tag{16}$$

where $A = \left[-2.457 \cdot \ln\left(\left(\frac{7}{Re}\right)^{0.9} + 0.27(e/d)\right)\right]^{16}$, $B = \left(\frac{37530}{Re}\right)^{16}$.

Solving Eqs.(7) – (12), we obtain the distributions of temperatures, electric potential (for thermoelements), velocities and pressure (for heat carrier).

The above differential equations with the respective boundary conditions were solved using Comsol Multiphysics package of applied programs. It was used to perform a multiparameter

optimization of thermoelectric heat pump design and to determine the electric and thermal parameters for the achievement of boundary values of its heating coefficient when assuring the possibility of THP operation under severe conditions of manned space missions.

Computer simulation results

The external appearance of thermoelectric heat pump is represented in Fig. 2.

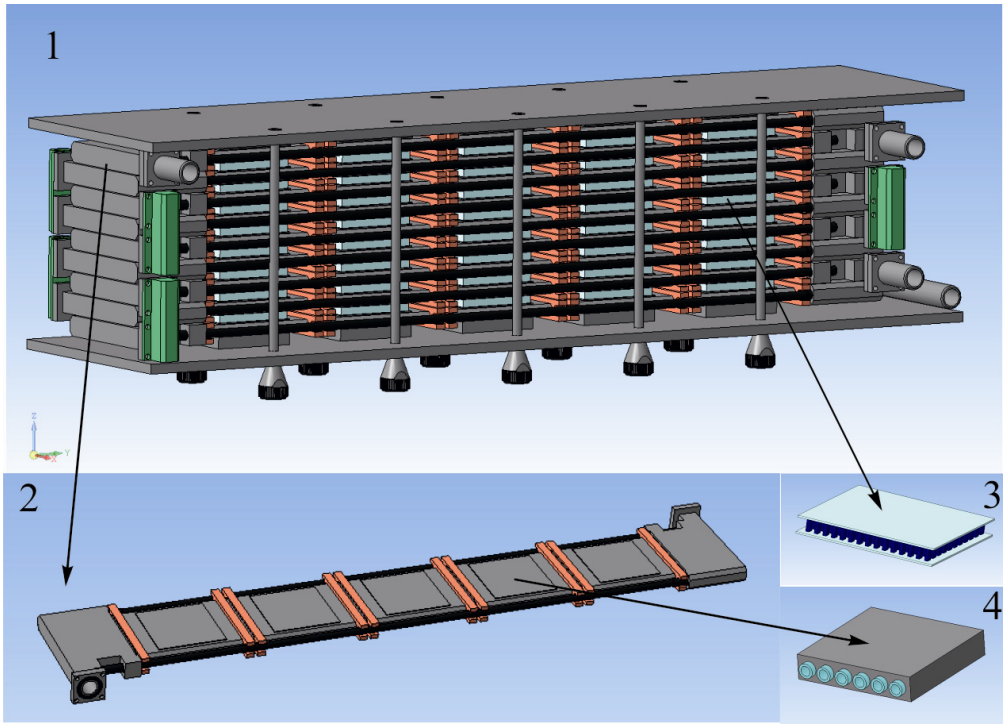

Fig. 2. Thermoelectric heat pump:
1 – external appearance, 2 – schematic of connection of
one row of heat exchangers 4, 3 – thermoelectric modules.

Below are given the results of optimization of the parameters of electric power supply to thermoelectric modules (according to model in item 1) for real thermal and temperature operating conditions of the heat pump. The results of computer investigations of thermoelectric module design, as well as heat exchange system are very important and will be presented in detail in the next work.

The initial data:

electric power supply to thermoelectric modules – 300 W;
the number of thermoelectric modules – 80 pcs;
heat carrier temperature at inlet to hot heat transfer loop – 36ºC;
heat carrier temperature at inlet to cold heat transfer loop – 31.5ºC;
hydraulic resistance of each heat-transfer loop – not more than 0.07 atm;
heat carrier flow rate in each loop – not more than 22 ml/s.

Thus, the values of integral heating coefficient were calculated for different variants of electric power supply to thermoelectric modules:

1) all the modules are powered by the same current and voltage, optimal for the entire heat pump;
2) the modules are grouped into two sections with individually optimized power supply;
3) the modules are grouped into four sections with individually optimized power supply;
4) all thermoelectric modules are powered by optimal current individually (80 conventional sections).

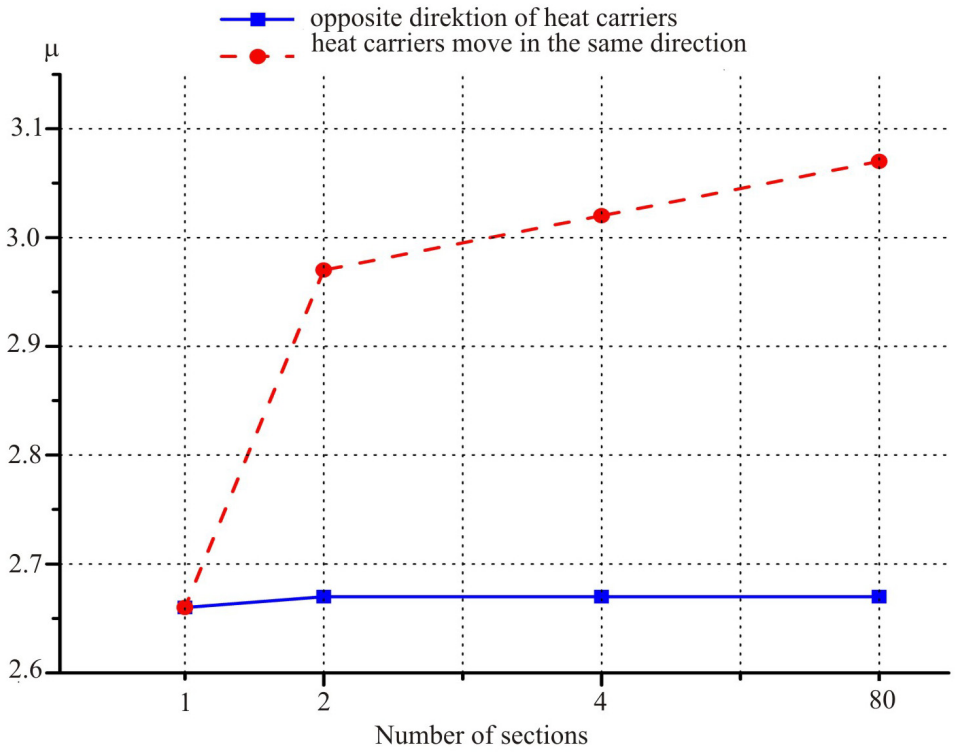

Fig. 3. Heating coefficient of thermoelectric heat pump versus the number of sections for two different hydraulic connections of heat carriers.

According to the results of simulation (Fig. 3), with such a hydraulic connection of the hot and cold heat exchange loops, when both heat carriers move in the opposite directions (direction 1.1 →1.2; 2.2 → 2.1 in Fig. 1), the heating coefficient of the heat pump is essentially independent of the number of sections and is at the level of ~ 2.6 ÷ 2.7. However, in the case when heat carriers move in the same direction (direction 1.1 →1.2; 2.1 → 2.2 in Fig. 1), increasing the number of sections with individual optimal power supply leads to heating coefficient growth to ~ 3.0 ÷ 3.1. The increase in heating coefficient of thermoelectric heat pump by 15% for such conditions is due to the fact that dependence of heating coefficient of thermoelectric modules on temperature difference and supply current in each section is nonlinear. In this case the use of several independent sections allows most efficient realization of all the advantages of thermoelectric power conversion in each temperature range.

Conclusions

1. The method of multiparameter computer optimization of thermoelectric heat pumps has been developed.
2. The optimal energy parameters of thermoelectric heat pump have been calculated for real conditions of its operation.
3. It has been established that increasing the number of sections of thermoelectric heat pump with individual electric power supply to each section results in the growth of integral heating coefficient by 15%.
4. It has been shown that the most efficient hydraulic connection of the hot and cold heat exchange loops is the case when both heat carriers move in the same direction.

References

1. Yu.Yu.Rozver, Thermoelectric Air-Conditioner for Vehicles, *J.Thermoelectricity* 2, 52 – 56 (2003).
2. L.I.Anatychuk, L.M.Vikhor, and Yu.Yu.Rozver, Investigation on Performance of Thermoelectric Cooler of Liquid or Gas Flows, *J.Thermoelectricity* 1, 73 – 80 (2004).
3. L.I.Anatychuk, N.Suzuki, and Yu.Yu.Rozver, Indoor Thermoelectric Air-Conditioner, *J.Thermoelectricity* 3, 53 – 56 (2005).
4. V.G.Rifert, V.I.Usenko, P.A.Barabash at al., Development and Test of Water Regeneration System from Liquid Biowaste on Board of Manned Spacecrafts with the Use of Thermoelectric Heat Pump *J.Thermoelectricity* 2, 63 – 74 (2011).
5. L.I.Anatychuk, P.A.Barabash, V.G.Rifert, Yu.Yu.Rozver, V.I.Usenko, and R.G.Cherkez, Thermoelectric Heat Pump as a Means of Improving Efficiency of Water Purification Systems for Biological Needs on Space Missions, *J.Thermoelectricity* 6, 78 – 83 (2013).
6. L.I.Anatychuk, Rational Areas of Thermoelectric Research and Applications, *J.Thermoelectricity* 1, 3 – 14 (2001).
7. L.I. Anatychuk, Current Status and Some Prospects of Thermoelectricity, *J.Thermoelectricity* №2, 7 – 20 (2007).
8. L.I.Anatychuk, A.V.Prybyla, On the Effect of Arrangement of Thermoelectric Modules and Heat Exchangers on the Efficiency of Liquid-Liquid Heat Pump, *J.Thermoelectricity* №4, p. 44 – 49 (2015).

Submitted 10.12.2015

R.R. Kobylianskyi

R. R. Kobylianskyi[1,2], I. A. Moskalyk[1]

[1]Institute of Thermoelectricity of the NAS and MES of Ukraine, 1, Nauky str.,Chernivtsi, 58029, Ukraine;
[2]Yu. Fedkovych Chernivtsi National University, 2, Kotsyubinsky str., Chernivtsi, 58012, Ukraine.

I.A. Moskalyk

COMPUTER SIMULATION OF LOCAL THERMAL EFFECT ON BIOLOGICAL TISSUE

The physical, mathematical and computer models of local thermal effects on biological tissue are constructed in this paper. The thermal effect of thermoelectric device work instrument on biological tissue for destruction of cancer tumours is investigated by computer simulation. Temperature distributions in biological tissue and work instrument in cooling and heating modes are determined. The obtained results make it possible to optimize device design to achieve the required depth of biological tissue freezing, and the maximum effect at destruction of cancer tumours.

***Keywords**: thermoelectric cooling, cryodestruction, hyperthermia, biological tissue, computer simulation.*

Introduction

It is known that the use of cooling in surgery [2] promotes the reduction of blood loss, weakens pain severity and duration, and prevents microbial contamination and metastasis spread. A deeper cooling (to -60 °C), followed by destruction of biological tissue structure, is also used in medical practice for cryodestruction [2 – 11]. In so doing, blood circulation, oxygen delivery, nutrient enrichment, tissue respiration and all biochemical processes are completely stopped. As a result, the death of cells, wherein all vital processes have been continuously paralyzed, occurs. A similar effect with using elevated temperatures - hyperthermia (+39 ÷ +45 °C) for the destruction of benign neoplasms is observed, which leads to thermal damage and destruction of cancer cells, while healthy cells remain undamaged.

The above mechanisms of thermal effect on biological tissue show that thermoelectric cooling and heating have good prospects for surgery. It is due to their advantages, namely possibility of setting precisely the required temperature of work instrument surface, the duration of temperature effect on the corresponding part of human body, and a cyclic change of cooling and heating modes [12, 13]. However, the use of reduced and elevated temperatures in medical practice requires a comprehensive in-depth study of the characteristic features of thermal effects in healthy and affected tissues, which is a complicated task that requires creation of precise physical and mathematical models and the use of computer simulation.

Therefore, *the purpose of this paper* is to develop computer simulation method which will make it possible to predict the results of local thermal effect on biological tissue at the destruction of cancer tumours.

Physical, mathematical and computer models of local thermal effect on biological tissue

Prediction of thermal effect on biological tissue is an intricate multi-parameter task, which depends on the temperature and geometry of the work instrument, the cooling rate, the time of exposure, as well as the size and structure of biological tissue.

To solve this task, a method of analytical simulation of frozen tissue is generally used.

There is a fair amount of models describing the processes of freezing around cryotools which differ in complexity [14 – 17]. Analytical simulation for the estimation of the freezing area size is critical as a method for analysis and optimization of cryodestruction efficiency and as a basis for calculation of designs and systems of cryotools for deep cooling of cryosurgical equipment. Introduction of mathematical methods for prediction of thermal effect results will depend on the accuracy of description of thermal processes occurring during freezing of living tissues and accompanying phase transitions [18, 19].

In order to make preliminary prediction of the results of local thermal effects on biological tissue, physical (Fig. 1), mathematical and computer models have been developed.

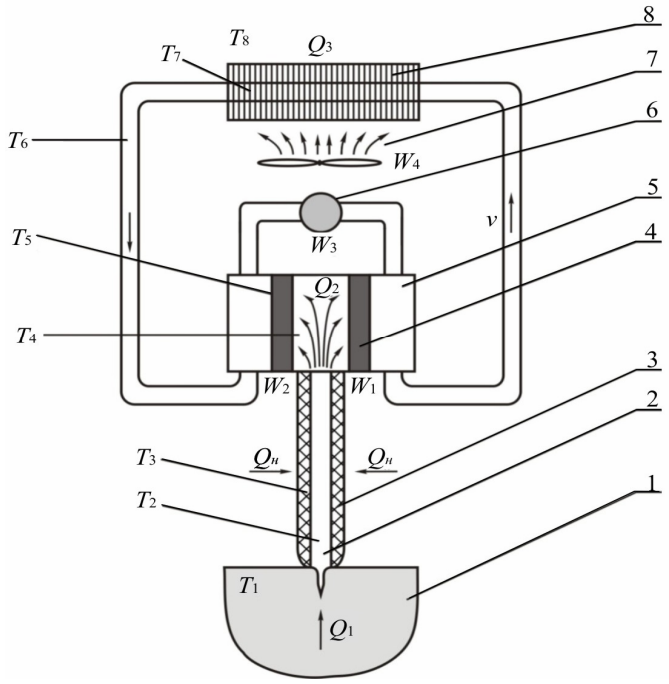

Fig. 1. A physical model of local thermal effect on biological tissue:
1 – biological tissue, 2 – work instrument, 3 - insulation,
4 - two-stage thermoelectric module, 5 - liquid heat exchanger,
6 - pump, 7 - fan, 8 - liquid-air heat exchanger.

Structurally, a model consists of a work instrument, thermal insulation of the work instrument lateral surface; 2 two-stage thermoelectric modules, on the hot sides of which liquid heat exchangers are mounted, a circulation pump, which pumps the water through the channels; a fan and a liquid-air heat exchanger, which cool the liquid pumped. Since it is necessary to achieve the lowest possible temperature values for the destruction, thermoelectric modules which are characterized by increased temperature difference ΔT_{max} are used.

The heat flow through the thermoelectric modules:

$$Q_2 = Q_1 + Q_H \,, \tag{1}$$

where Q_1 is the heat flow from the tumor, Q_{hg} is the heat inleak through the lateral surface of the work instrument.

The heat flow from the thermoelectric modules:

$$Q_3 = Q_2 + W\,, \tag{2}$$

where W is the power of thermoelectric modules.

The heat flux transferred to water from the hot side of the modules:

$$Q_4 = \alpha_4 S_4 (T_5 - T_6)\,. \tag{3}$$

The heat flux transferred to the liquid-air heat exchanger from water:

$$Q_5 = \alpha_5 S_5 (T_6 - T_7)\,. \tag{4}$$

The heat flux transferred to environment from the liquid-air heat exchanger:

$$Q_6 = \alpha_6 S_6 (T_7 - T_8)\,, \tag{5}$$

where α_4, α_5, α_6 are the heat transfer coefficients, S_4, S_5, S_6 are the heat exchange surface areas.

To determine the temperature distribution in the structural components of thermoelectric device for cancer tumours destruction in biological tissue (liver affected with cancer), Comsol Multiphysics software package is used [20, 21] which allows simulation of thermophysical processes in biological tissue with regard to blood circulation and metabolism. The heat transfer equation in biological tissue in this case will take on the form:

$$\rho C_p \frac{\partial T}{\partial t} + \nabla \cdot (-k \nabla T) = \rho_b C_b \omega_b (T_b - T) + Q_{met}\,, \tag{6}$$

where: ρ_b is blood density (kg/m^3), C_b is specific heat (J/kg*K), ωb is blood circulation rate (1/sec), T_b is arterial blood temperature (K), Q_{met} is the amount of heat due to metabolism (W/m^3).

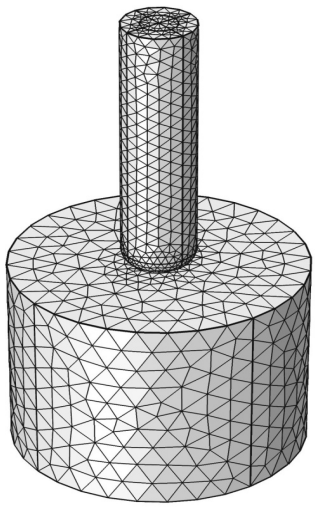

Fig. 2. Finite element method mesh.

Calculation of temperature and heat flux density distribution in biological tissue and work instrument is carried out by the finite element method [22] (Fig. 2).

Computer model is a bulk of the biological tissue with the isotropic thermal properties. A needle made of high thermal conductivity material fixed on the rod of the same material is placed inside the tissue. The rod, surrounded by thermal insulation, is in heat exchange state with the environment. The temperature at the end of the rod is preset and equals to -50 °C. The boundary condition in the area sufficiently distant from the probe, where the temperature should be equal to body temperature, is 37 °C. In the process of freezing, cells will be subject to phase change at freezing point. The tissue properties in frozen and unfrozen states are shown in Table 1. In the temperature range of -1 ÷ -8 °C, when the cells are frozen, the latent heat of the phase transition is absorbed and can be simulated by adding the corresponding value to specific heat [23].

Table 1.

The properties of biological tissue in frozen and unfrozen states [24]

	Unit	Value
Specific heat of frozen tissue	MJ/m^3 °C	1.8
Specific heat of unfrozen tissue	MJ/m^3 °C	3.6
Specific heat of blood	MJ/m^3 °C	3.6
Thermal conductivity of unfrozen tissue	W/ m °C	0.5
Thermal conductivity of frozen tissue	W/m °C	2
Latent heat	MJ/m^3	250
Body temperature	°C	37
Lower phase transition temperature	°C	-8
Upper transition temperature	°C	-1
Blood perfusion in healthy tissue	ml / s / ml	0.0005
Blood perfusion in tumour	ml/s/ml	0.002
Metabolism in normal tissue	W/m^3	4200
Metabolism in tumour	W/m^3	42000

Moreover, at freezing of biological tissue, blood vessels in capillaries are constricted to freezing of all the blood, the value ω_b tending to zero. In this case, the cells will not be able to generate metabolic heat, and Q_{met} will be equal to zero.

Work instrument optimization

Temperature distributions in the work instrument and tumor for heating and cooling modes were investigated, which allowed optimization of thermoelectric device work instrument for the destruction of oncologic neoplasms. Dependences of freezing depth and needle temperature on the diameter and length of work instrument and needle diameter were determined.

As an example, Fig. 3 shows a typical temperature distribution in the work instrument and biological tissue in cooling mode. For this case: rod diameter is 8 mm, rod length is 40 mm, insulation thickness is 5 mm, needle length is 7 mm, needle diameter is 2 mm. Curves 1, 2 are isotherms - 1°C and - 8 °C, respectively. Temperature distribution along half-sphere radius of the work instrument thermal effect (lines *R* in Fig. 3) is shown in Fig. 4.

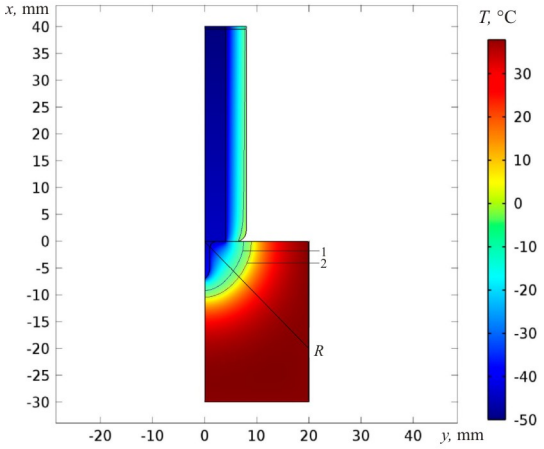

Fig. 3. Typical temperature distribution in the work instrument and biological tissue in cooling mode.

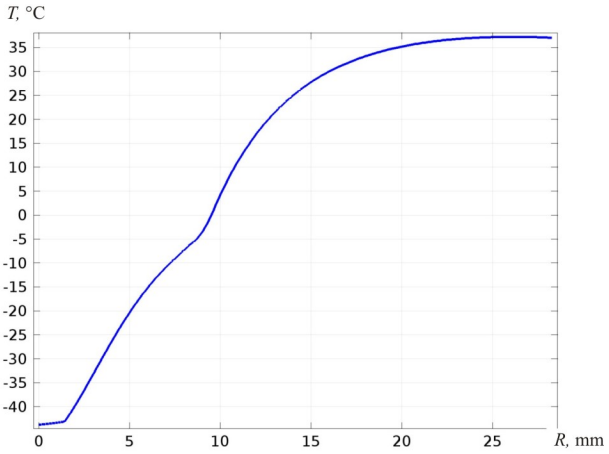

Fig. 4. Temperature distribution along half-sphere radius of device thermal effect for cooling mode.

Similar distributions for heating mode are shown in Figs. 5 – 6. Fig. 5 shows a typical temperature distribution in the work instrument and biological tissue, Fig. 6 – temperature distribution along line *R*.

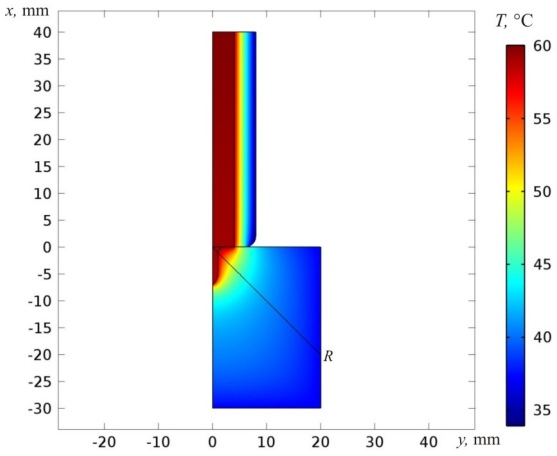

Fig. 5. Typical temperature distribution in the work instrument t and biological tissue in heating mode.

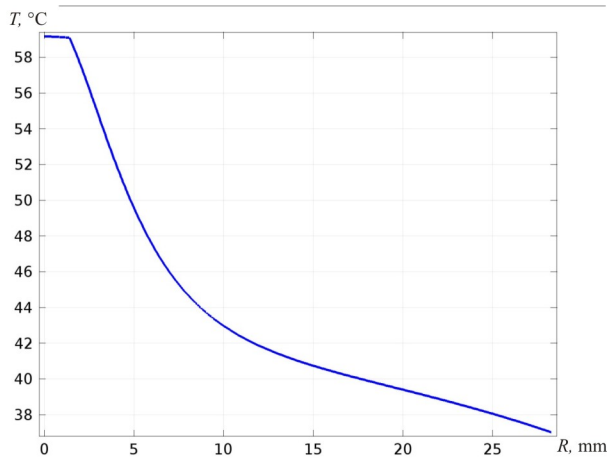

Fig. 6. Temperature distribution along half-sphere radius of device thermal effect for heating mode.

Figs. 7 – 11 show the dependences of needle temperature and freezing depth on the rod diameter at different rod lengths. Insulation thickness h_{is} = 5 mm, needle diameter d_n = 2 mm, needle length h_n = 7 mm.

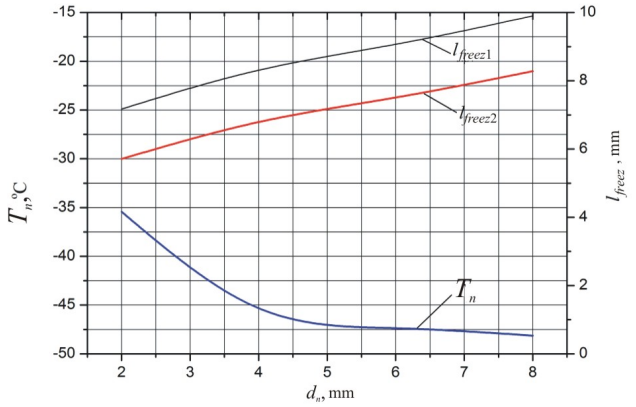

Fig. 7. Dependences of needle temperature (T_n) and freezing depth (l_{freez1} is the distance t o isotherm with temperature -1 ° C, l_{freez2} is the distance to isotherm with temperature -8 ° C) on rod diameter (rod length 10 mm).

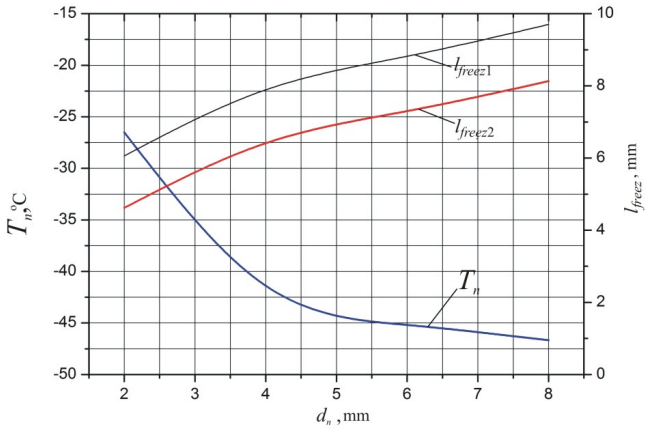

Fig. 8. Dependences of needle temperature (T_n) and freezing depth ($freez_1$ is the distance to isotherm with temperature -1 ° C, l_{freez2} is the distance to isotherm with temperature -8 ° C) on rod diameter (rod length 20 mm).

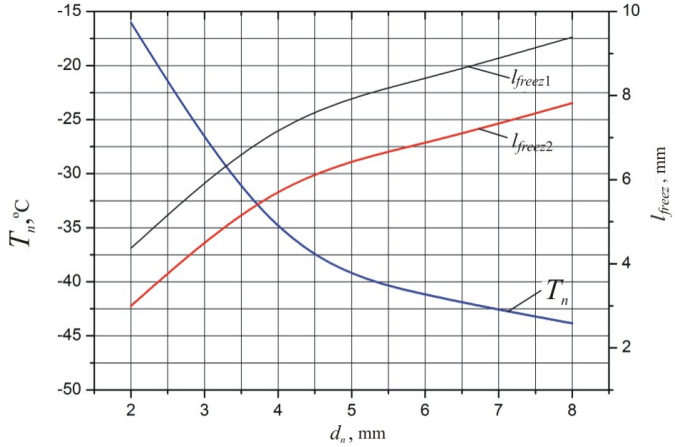

Fig. 9. Dependences of needle temperature (T_n) and freezing depth (l_{freez1} is the distance to isotherm with temperature -1 ° C, l_{freez2} is the distance to isotherm with temperature -8 ° C) on rod diameter (rod length 40 mm).

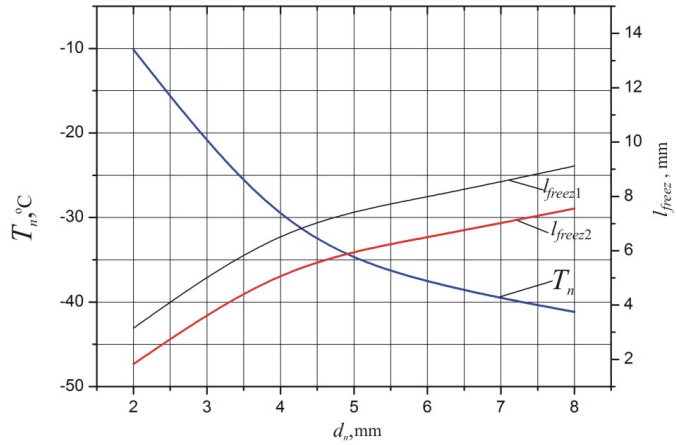

Fig. 10. Dependences of needle temperature (T_n) and freezing depth (l_{freez1} is the distance to isotherm with temperature -1 ° C, l_{freez2} is the distance to isotherm with temperature -8 ° C) on rod diameter (rod length 60 mm).

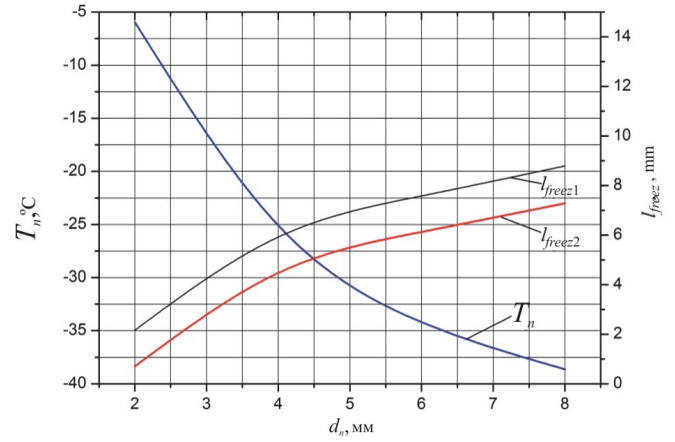

Fig. 11. Dependences of needle temperature (T_n) and freezing depth (l_{freez1} is the distance to isotherm at temperature -1 ° C, l_{freez2} – distance to isotherm with temperature -8 ° C) on rod diameter (rod length 80 mm).

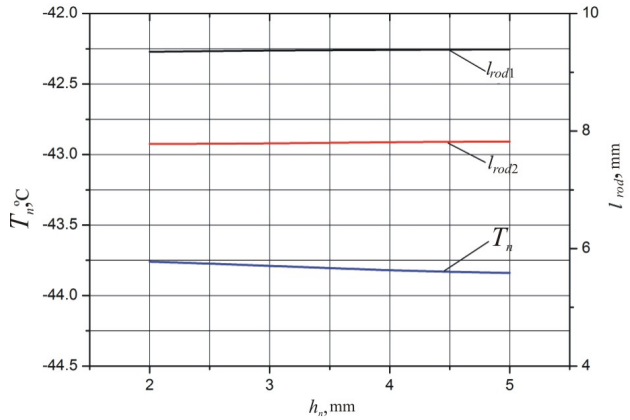

Fig. 12. Dependences of needle temperature (T_n) and freezing depth (h) on insulation thickness (d_n = 1 mm, h_n = 10mm, h_{rod} = 80 mm).

Dependences of needle temperature and freezing depth on insulation thickness are shown in Fig. 12. Rod diameter d_{rod} = 8 mm, rod length l_{rod} = 40 mm, needle diameter d_n = 2 mm, needle length h_n = 7 mm.

Dependences of needle temperature and freezing depth on needle diameter are shown in Fig. 13. Rod diameter d_{rod} = 8 mm, rod length l_{rod} = 40mm, insulation thickness h_{ins} = 5 mm, needle length h_n = 7 mm.

Dependences of needle temperature and freezing depth on needle length are shown in Fig.14. Rod diameter d_{rod} = 8 mm, rod length l_{rod} = 40 mm, insulation thickness h_{ins} = 5 mm, needle diameter d_n = 2 mm.

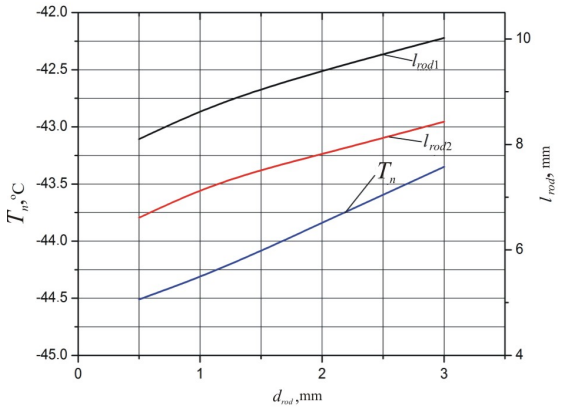

Fig. 13. Dependences of needle temperature (T_n) and freezing depth (h) on needle diameter (d_{rod} = 8, l_{rod} = 40, h_{ins} = 5, h_n = 7 mm).

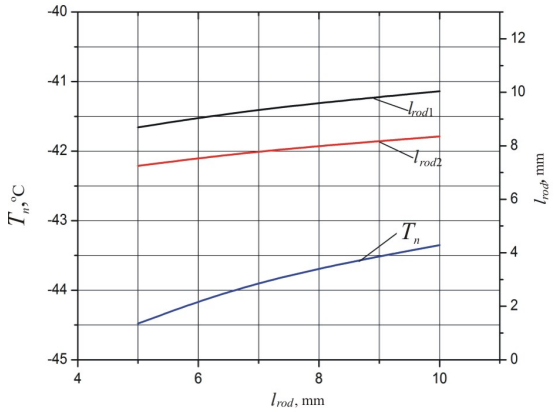

Fig. 14. Dependences of needle temperature (T_n) and freezing depth (h) on needle length (d_{rod} = 8, l_{rod} = 40, h_{ins} = 5, d_n = 2 mm).

The obtained results allow optimizing device design to achieve the required biological tissue freezing depth and maximum effect at destruction of oncologic neoplasms.

Conclusions

1. The physical, mathematical and computer models of local thermal effects on biological tissue have been constructed.
2. Computer simulation method has been developed, which allows predicting the results of local thermal effect on biological tissue at destruction of oncologic neoplasms.
3. Analysis of temperature distribution in biological tissue at cyclic cooling and heating effect has been performed. Optimal geometric size of work instrument to achieve maximum therapeutic effect has been determined.

References

1. E.A.Kolenko, *Thermoelectric Cooling Device, 2nd Ed*. (Leningrad: Nauka, 1967), 283 p.
2. N.N.Korpan, Cryosurgery in XXI Century, *In: Medical Cryology 2. Proceedings* (Nizhniy-Novgorod, 2001), p. 133 – 137.
3. *Cryosurgery*, Ed. by E.I.Kandel (Moscow, 1974).
4. V.I.Kochenov, Adhesive Effect in Cryosurgery, *Abstract in the International Abstract Journal*, section IV, 8 (1982).
5. V.V.Budrik, Physical Foundations of Cryomethods in Medicine, *Medical Cryology*, issue 5, 48 (2004).
6. S.D.Dorokhov, Achievements in Cryomedicine, *Proc. Intern.Symp*. (Saint-Petersburg, 2001), p.118.
7. M.P.Burykh, *Fundamentals of Surgical Operations Technology* (Kharkiv: Znaniye, 1998), 480p.
8. M.I.Kuzin, S.T.Kharkai, *Local Anaesthesia* (Moscow: Medicine, 1982), 140p.
9. S.A.Simbirtsev, *Fundamentals of Operative Surgery* (Saint-Petersburg: Hippocrates, 2002), 631p.
10. G.M.Semenov, *Modern Surgical Instruments* (Saint-Petersburg: Piter, 2006), 352p.
11. V.I.Bezak, *Medical Instruments and Equipment* (2nd Ed., revised and enlarged (Moscow: Medicine, 1969), 188p.
12. L.I.Anatychuk, O.J.Luste, and L.Ya.Kushneryk, Computer Control of Temperature Distribution in Tissues at Surgery and Cryotherapy, *J.Thermoelectricity* 4, 79 – 83 (2006).
13. L.A.Moskalyk, O.M.Manik, On the Use of Thermoelectric Cooling in Cryodestruction Practice, *J.Thermoelectricity* 6, 84 – 92 (2013).
14. A.A.Berezovsky, Yu.N.Muskin, *Mathematical Prediction of Plane Parallel Cryodestruction of Biological Tissue in vivo, Stefan's Problems with a Limit Steady State in Cryosurgery (*Kyiv: 1986; 17 – 36), Preprint of USSR AS, Institute of Mathematics; 86 – 37).
15. V.V.Budrik, Research on Heat-Exchange Processes in Cryosurgical Probes with Forced Cryoagent Circulation: *Synopsis of PhD Thesis* (Moscow: 1979), 21p.
16. L.L.Vasilyev, *Prospects of Using Heat Pipes and Porous Heat Exchangers in New Equipment. Heat and Mass Transfer of Cryogenic Liquids in Porous Heat Exchangers* (Minsk, 1974), P.3 – 23.
17. I.A.Drabkin, Z.M.Dashevsky, and V.B.Osvensky, Method for Calculation of Thermoelectric Cooling Devices, *Proc. of VIII Interstate Workshop "Thermoelectrics and Their Applications" (Saint-Petersburg, 2002).*
18. T.A.Ismailov, Development and Creation of Semiconductor Thermoelectric Devices for Medicine, Thesis of Report to All-Russia Scientific and Technical Conference "*"Status and Outlook for Progress in Medical Instruments Building"* (Makhachkala, DSU, 1996).
19. A.B.Sulin, Realization of Peltier Effect in Medical-Purpose Devices, *Proc. of Conference "Status and Outlook for Progress in Medical Instruments Building"* (Makhachkala, DSU, 1996).
20. W.Roger, *Pryor Multiphysics Modeling using Comsol: a First Principles Approach* (Jones and Bartlett Publishers London W6 7PA United Kingdom, 2011), 871p.
21. *COMSOL Multiphysics User's Guide*. COMSOL AB, 2010. – 804p.
22. V.A.Ovcharenko, S.V.Podlesny, and S.M.Zinchenko, *Fundamentals of Finite Element Method and its Application in Engineering Calculations* (Kramatorsk: Donbass State Machine Building Academy, 2008), 380 p.
23. Han Liang Lim, Venmathi Gunasekaran, *Mathematical Modeling of Heat Distribution during Cryosurgery.*
24. ZS Deng, J.Liu, *Cryobiology 50 Numerical Simulation of Selective Freezing of Target Biological Tissues Following Injection of Solutions with Specific Thermal Properties*, 2005, pp.183 – 192.

Submitted 27.07.2015.

T.A.Ismailov, O.V.Yevdulov, D.V.Yevdulov

Federal State Budgetary Educational Institution of Higher Professional Education
"Dagestan State Technical University", 70, Imam Shamil avenue,
Makhachkala, 367015, Russia

RESULTS OF THEORETICAL RESEARCH ON COOLING SYSTEM FOR RADIO ELECTRONIC EQUIPMENT ELEMENTS WORKING IN THE INTERMITTENT HEAT RELEASE MODE

The paper deals with cooling system for radio electronic equipment elements working in the intermittent heat release mode based on melting working agents with the additional heat removal via a thermopile. The basic design ratios for its theoretical study are given. Dependences of REE element stable operation time, as well as its temperature characteristics with provision of its thermal conditions by the system in question are represented.
***Key words**:* cooling system, REE element, heat exchange, melting working agent, melting, solidification, thermopile, simulation.

Introduction

In the design of radio electronic equipment (REE) intended for work in a wide range of thermal loads, one has to take into account the impact of temperature on its characteristics and parameters. If the latter go beyond the limits permissible for its normal operation, recourse is made to some or other cooling and temperature stabilization methods.

At the present time, in the practice of REE design, various methods are used for provision of its thermal conditions, among which special mention should go to air, liquid, conductive, evaporative, thermoelectric, and some special methods [1 – 3]. Each of the above methods has its strong and weak points. In particular, REE cooling on the basis of air and conductive methods is inefficient because of the low intensity of heat removal and temperature accuracy. Liquid and evaporative thermal stabilization system is difficult to make and requires bulky equipment of complicated design. Moreover, in this case a source of electric energy is needed for power supply to cooling systems.

A promising method for cooling REE working in the intermittent heat release mode is based on the use of melting working agents with a stable melting temperature [4]. Structurally, devices that implement this method have the form of a container filled with a melting working agent. A REE element is brought into direct contact with this container and can be arranged both inside the container and on its surface [5]. During operation, the basic part of heat dissipated by equipment element or unit is absorbed due to latent heat of agent melting. On termination of equipment operation, the agent is cooled down and solidified as a result of heat exchange with the environment.

The main disadvantage of such systems restricting their application for cooling REE with high heat flux densities is a need to maintain working agent in the state of phase transition during the entire operation period of electronic device. Since the element, while in operation, releases considerable powers, in many cases the heat storage capacity of working agent proves to be insufficient to provide for the required temperature mode during the entire operation period (working

agent will be clear-melted by the end of the element operation cycle).

In this context, on cooling of high-power radio electronic devices with the use of melting working agents it is worthwhile to use some additional cooling system for removal of excess heat from the working agent. As regards the energy and mass-dimensional parameters, good use can be made of a thermopile as such additional cooling system. A similar system was considered in [6], where its different embodiments are described, characterized in different ways of orientation of a container with melting working agent and a thermopile, as well as in different operation modes.

The purpose of this paper is development of a mathematical model and theoretical studies of the herein described system of heat removal from REE elements working in the intermittent heat release mode which is based on a joint use of working agents melting in given temperature range and thermoelectric cooling method.

Design of cooling system for radio electronic equipment elements working in the intermittent heat release mode

Fig. 1 represents structural schematic of system under consideration, and Fig. 2 – its appearance. Here, thermopile 1 is brought into good thermal contact with the end surface of a thin-walled metal container 2 filled with working agent 3, on the other surface of which a radio electronic equipment element 4 is mounted. The thermopile works in the intervals of heat release element operation.

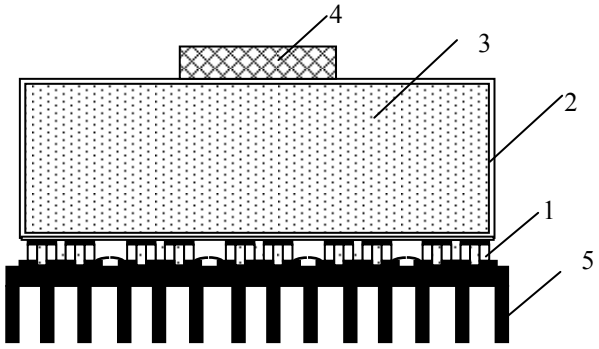

Fig. 1. Structural schematic of a system for cooling radio electronic equipment elements working in the intermittent heat release mode.

Fig. 2. Appearance of a system for cooling radio electronic equipment elements working in the intermittent heat release mode.

The operating principle of device is as follows. Heat coming from REE element 4 is passed to metal container 2 and through contact surface to working agent 3. Then there is a simultaneous warm up of working agent 3 to melting temperature, and melting process takes place accompanied by absorption of heat released by REE. On termination of operating cycle of REE element 4, the working agent 3 is cooled down and solidified due to heat removal by thermopile 1 working in cooling mode. Solidification time of working agent 3 in this case is attained by increasing the intensity of heat removal.

A mathematical model of cooling system for REE elements working in the intermittent heat release mode

Mathematical simulation of cooling system considered includes investigation of

thermophysical processes upon melting and solidification of working agent, as well as calculation of an appropriate thermopile.

Simulation of processes related to a change in the aggregate state of working agent was done by solving Stephan's problem with the use of Leybenzon's method [7]. The principle of the approximate solution method lies in the selection of such functions of the liquid and solid phase temperature variation that would meet the required initial and boundary conditions. The thus selected functions are substituted into phase matching condition at phase interface, and the resulting differential equation is solved for phase interface coordinate. For the case under consideration the temperature profiles in the solid and liquid phase are represented as a polynomial dependence in conformity with recommendations [4].

As a result, the following equation systems were obtained for research on the processes of melting and solidification of working agent with and without convective fluxes in the liquid substance phase:

1. For the case of working agent melting without a developed convection in the liquid phase of heat accumulator

$$\frac{dT_j}{d\tau}=\frac{1}{(c\rho\delta)_j}\left[q_{REE}+\alpha_{amb}\left(T_{amb}-T_{amb}\right)+\frac{\lambda_1}{\xi}\left(T_{cr}-T_j\right)\right], \tag{1}$$

$$\frac{d\xi}{d\tau}=\frac{\frac{1}{2}c_1\rho_1\xi\frac{dT_j}{d\tau}+\frac{\lambda_1}{\xi}\left(T_{cr}-T_j\right)}{c_1\rho_1\left(\frac{1}{2}T_{cr}-T_j\right)-c_2\rho_2\left(T_{cr}-T_{2R0}\right)\frac{\xi-R}{\xi_0-R}-\rho_2 r}. \tag{2}$$

2. For the case of working agent melting with a developed convection in the liquid phase of heat accumulator

$$(c\rho\delta)_j\frac{dT_j}{d\tau}=q_{PEA}+\alpha_{amb}\left(T_{amb}-T_{amb}\right)+\alpha_{cr}\left(T_1-T_j\right), \tag{3}$$

$$c_1\rho_1\xi\frac{dT_1}{d\tau}=\alpha_j\left(T_1-T_j\right)+\alpha_{cr}\left(T_{cr}-T_1\right), \tag{4}$$

$$\frac{d\xi}{d\tau}\left[c_2\rho_2\left(\frac{-2\cdot n\left(T_{cr}\cdot R-T_{2R0}\cdot R\right)+\xi\left(T_{2R0}-T_{cr}\right)}{(n+1)(\xi_0-R)}\right)+r\rho_2\right]=\alpha_{cr}\left(T_1-T_{cr}\right). \tag{5}$$

3. For the case of working agent solidification without a developed convection in the liquid phase of heat accumulator

$$\frac{dT_j}{d\tau}=\frac{1}{(c\rho\delta)_j}\left[\alpha_{amb}\left(T_{amb}-T_j\right)+\frac{\lambda_2\left(T_{cr}-T_j\right)}{\xi}\right], \tag{6}$$

$$\frac{d\xi}{d\tau}=\frac{\lambda_2\left(T_{cr}-T_j\right)-q_{TEB}\left(R-\xi\right)}{\rho_1 r-\frac{1}{2}c_2\rho_2\left(T_j-T_{cr}\right)-c_1\rho_1\left(T_{1R0}-T_{cr}\right)\frac{R-\xi}{\xi_0-R}}. \tag{7}$$

4. For the case of working agent solidification with a developed convection in the liquid phase of heat accumulator

$$(c\rho\delta)_j \frac{dT_j}{d\tau} = \alpha_{amb}\left(T_{amb} - T_j\right) + \alpha_{cr}\left(T_1 - T_j\right), \quad (8)$$

$$c_1\rho_1\xi\frac{dT_1}{d\tau} = \alpha_j\left(T_1 - T_j\right) + \alpha_{cr}\left(T_{cr} - T_1\right), \quad (9)$$

$$\frac{d\xi}{d\tau}\left[c_2\rho_2\left(\frac{-2\cdot n\left(T_{cr}\cdot R - T_{2R0}\cdot R\right) + \xi\left(T_{2R0} - T_{cr}\right)}{(n+1)(\xi_0 - R)}\right) + r\rho_1\right] = \alpha_{cr}\left(T_1 - T_{cr}\right) - q_{TEB}. \quad (10)$$

In relations (1) – (10), c_i, ρ_i, λ_i are heat capacity, density and thermal conductivity of the liquid and solid phase of working agent, where index 1 corresponds to the liquid phase, and index 2 – to the solid phase of working agent; τ is time; q_{REE} is the amount of heat released by REE element per unit time and falling at unit area of the end surface of a container with heat accumulator; α_{amb} is coefficient of heat transfer to the environment, T_j is the bulk temperature of device metal jacket (the heat spent on heating or cooling of REE element due to its small value as compared to the heat accumulated by working agent, is ignored or taken into account in total heat capacity of metal jacket; this assumption allows taking the value of T_{amb} as the temperature of REE element); T_{amb} is ambient temperature; r is working agent melting heat; R is working agent layer thickness; ξ is phase interface; α_j, α_{cr} are coefficients of heat transfer from the jacket to liquid and from the phase interface to liquid; T_1 is the average temperature of the liquid phase; τ_0, ξ_0 are the time and melt thickness whereby an intensive motion of convective currents starts, and temperature field in the liquid phase practically disappears; T_{2R}, T_{2R0} are temperatures at $x = R$ at any moment of time τ and at $\tau = \tau_0$, respectively, ξ_0 is melt thickness at $\tau = \tau_0$; τ_0 is time whereby a linear change in temperature T_{2R} with time starts to be observed; n is parameter determined experimentally [4]; $q_{THERMOPILE}$ is the amount of heat removed per unit time by thermopile and falling at unit area of the end surface of a container with heat accumulator.

Thermopile calculation was done on the basis of a standard procedure with the use of application software package "Thermoelectric system calculation" (manufacturer – OJSC Kryotherm, Saint-Petersburg) [8]. From the analysis of $q_{THERMOPILE}$ values equivalent to thermopile cooling capacity, the geometric dimensions of thermoelements contained in a thermopile, the value of supply current, and the electric power consumption were determined.

Results of a numerical experiment with cooling system for REE elements working in the intermittent heat release mode

Results of a numerical experiment with the developed model of cooling device are given in Figs.3 – 10. Here, we show the time dependences of jacket temperature variation upon melting of agent, as well as the time dependences of phase interface coordinate for different scattering powers of REE element (Fig. 3 – 4), different fillers (Fig. 6 – 7), and the duration of full melting of working agent versus heat release power of REE element (Fig. 8). Fig. 5 shows for comparison the temporal variation of jacket temperature with the use of melting agent and natural air heating. Similar data for cooling mode are given in Figs.11 – 16.

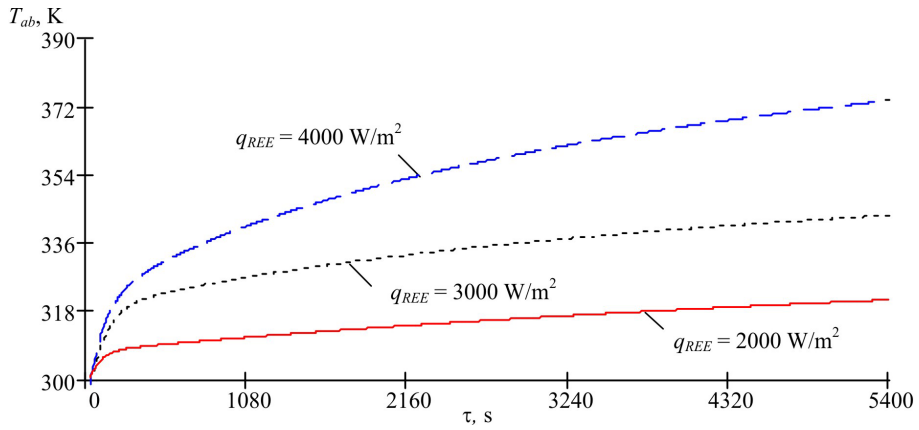

Fig. 3. Time dependence of jacket temperature upon melting of agent (paraffin) without liquid phase convection, $(c\rho\delta)_j = 2\cdot10^3$ J/(m^2·K) R = 0.03 m.

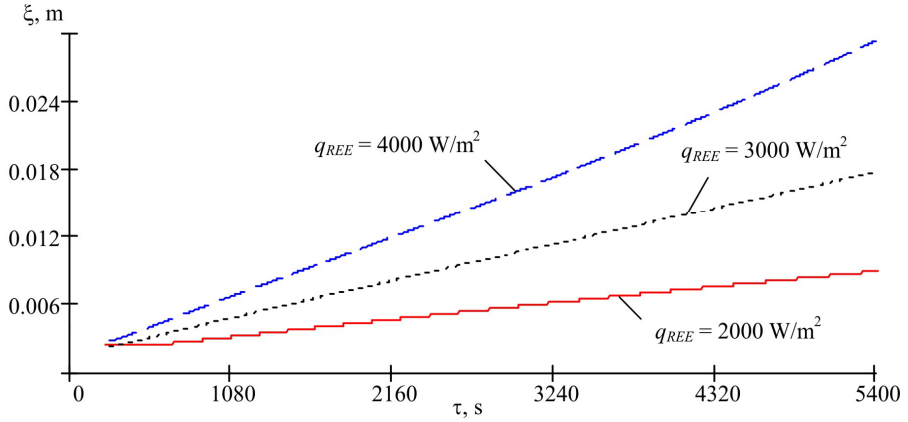

Fig. 4. Time dependence of phase interface coordinate upon melting of agent (paraffin) without liquid phase convection, $(c\rho\delta)_j = 2\cdot10^3$ J/(m^2·K); R = 0.03 m.

Calculations were made with the following input data: working agents – paraffin (ρ_1 = 760 kg/m^3, ρ_2 = 780 kg/m^3, c_1 = 2680 J/kg·K, c_2 = 2350 J/kg·K, λ = 0.27 W/m·K, $r = 156\cdot10^3$ J/kg, T_{cr} = 316 K), elaidic acid (ρ_1 = 850 kg/m^3, ρ_2 = 860 kg/m^3, c_1 = 2180 J/kg·K, c_2 = 1550 J/kg·K, λ = 0.16 W/m·K, $r = 214\cdot10^3$ J/kg, T_{cr} = 318 K), nickel nitrate (ρ_1 = 1980 kg/m^3, ρ_2 = 2050 kg/m^3, c_1 = 2140 J/kg·K, c_2 = 1800 J/kg·K, λ = 0.56 W/m·K, $r = 155\cdot10^3$ J/kg, T_{cr} = 329.7 K), T_{amb} = 293 K, α_{amb} = 10 W/K·m^2
(except for cases when the value of α_{amb} is indicated directly in captions to plots), ξ_0 = 0.001 m; τ_0 = 20 s, α_j = 20 W/K·m^2, α_{cr} = 20 W/K·m^2.

The calculated dependences define that jacket temperature and the time of working agent melting vary with the value of thermal load on cooling device (q_{REE}), the type of working agent, as well as the conditions of heat exchange with the environment. In the absence of convective fluxes in the liquid phase, the process of heat exchange is the nonsteady-state heat conduction, and the device jacket temperature is constantly increasing. The rate of its increase is a function of heat input (q_{REE}), layer thickness and agent thermal conductivity.

According to plots shown in Figs. 3 – 4, the increase in q_{REE} value increases considerably the temperature of the jacket and REE element, as well as agent melting rate (for instance, after 1.5 hours of REE element operation, with a change in its scattering power from 2000 to 4000 W/m^2, the jacket temperature rises from 320 to 372 K, and melting rate grows from $1.48\cdot10^{-6}$ m/s to $5.5\cdot10^{-6}$ m/s).

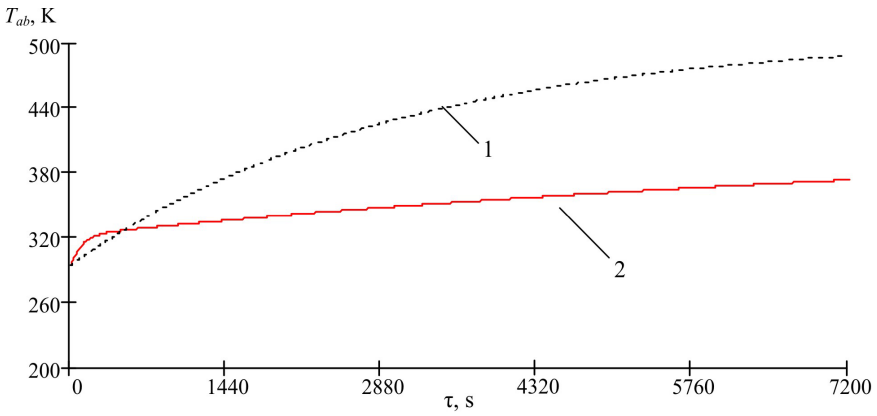

Fig. 5. Time dependence of jacket temperature upon melting of agent (paraffin) without liquid phase convection $(c\rho\delta)_j = 2\cdot10^3$ *J/(m²·K); R = 0.03 m,* $q_{REE} = 2000$ *W/m²,*
1 – use of natural air cooling with $\alpha_{amb} = 5$ *W/m²·K,*
2 – use of cooling system with working agent – nickel nitrate.

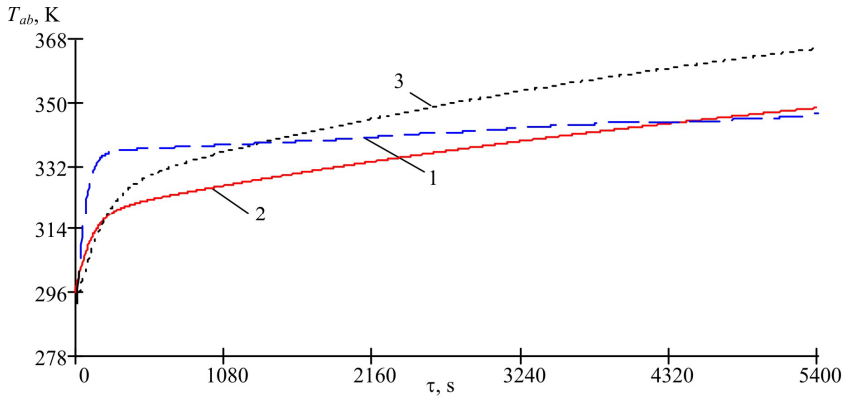

Fig. 6. Time dependence of jacket temperature upon melting of various heat accumulators without liquid phase convection, $(c\rho\delta)_j = 2.5\cdot10^3$ *J/(m²·K), R = 0.03 m,* $q_{REE} = 3500$ *W/m². 1 – nickel nitrate, 2 – paraffin, 3 – elaidic acid.*

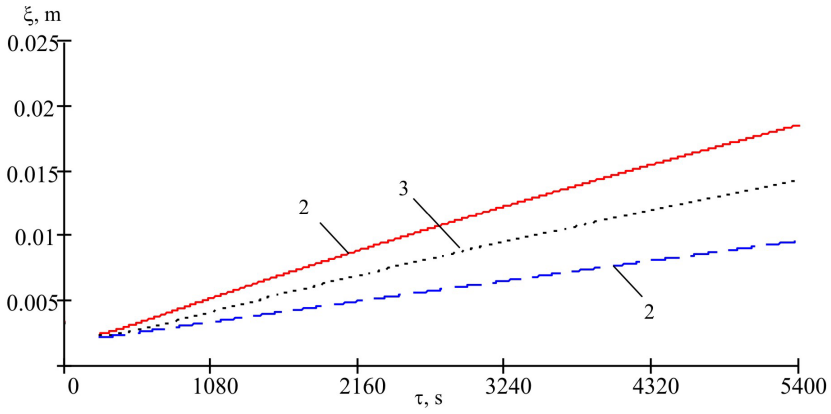

Fig. 7. Time dependence of phase interface coordinate upon melting of various heat accumulators without liquid phase convection, $(c\rho\delta)_j = 2.5\cdot10^3$ *J/(m²·K), R = 0.03 m,* $q_{REE} = 3500$ *W/m².1 – nickel nitrate, 2 – paraffin, 3 – elaidic acid.*

The rise in device jacket temperature is also related to increase in thermal resistance of working agent liquid phase, which grows with enlargement of melted layer. This proves the necessity of taking steps for reducing the layer of agent liquid phase between REE element and phase interface.

Also, the temperature of REE element while in operation will be affected by selection of suitable working filler. Calculations were made for the case of using as such nickel nitrate, paraffin and elaidic acid (Figs. 6 – 7).

According to research results, the best results for given conditions were obtained with the use of nickel nitrate as a filler. According to dependences shown in Fig. 6, for the case of using nickel nitrate as a working agent the temperature of device jacket is most stable, and melting rate is the lowest. First of all, it is due to its higher thermal conductivity which is almost twice that of paraffin and 3 fold that of elaidic acid. Thus, a reduction of temperature growth rate (i.e. its stabilization) can be achieved by increasing the effective thermal conductivity of agent. One of the methods for increasing the effective thermal conductivity of agent is the use of various fillers. Thus, for instance, one can use metal grit, various kinds of finning or porous structures.

Fig. 8 shows the plots of full melting time of various fillers versus the dissipation power of REE element, which corresponds to its stable operation time. Here, the longest-running melting in the range of powers 1000 to 5000 W/m^2 is inherent in nickel nitrate, which is accounted for by its higher temperature and heat of melting, as well as by the value of thermal conductivity coefficient.

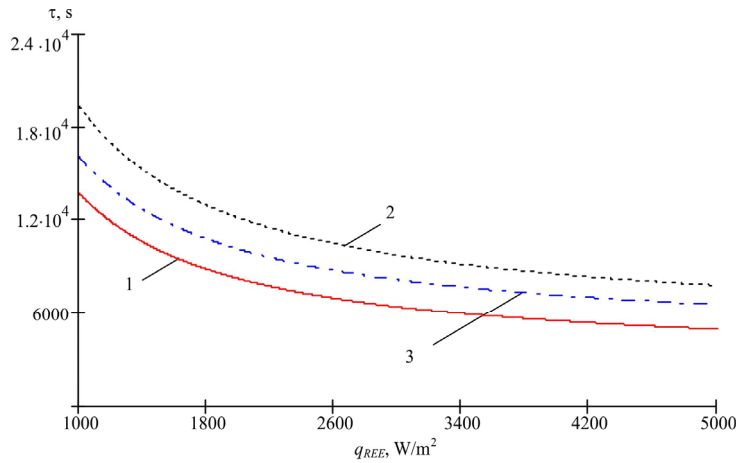

Fig. 8. Dependence of full melting time of various heat accumulators on heat release power of REE element per unit area without liquid phase convection, $(c\rho\delta)_j = 2.5\cdot10^3$ J/(m^2·K); R = 0.03 m.1 – paraffin, 2 – nickel nitrate, 3 – elaidic acid.

The process of agent melting is essentially affected by the presence of convective fluxes in its liquid phase. This case corresponds to arrangement of element on the lower end surface of a container with working agent and heat input from below with respect to heat accumulator. According to Figs. 9 – 10, for paraffin the convective fluxes start to have a considerable impact in 19 – 20 minutes after the start of melting process, which corresponds to melt thickness 0.009 – 0.01 m. From said moment for a developed convection in the agent liquid phase the process of melting is intensified. Consequently, the rate of travel of phase interface is increased, and temperature rise of cooling device jacket is retarded. As it follows from the plots in Fig. 9, in 1.5 hours after the beginning of melting process the temperature of device jacket with convection in the liquid phase of heat accumulator will be 12 K lower than without convective fluxes. At the same time, according to dependences represented in Fig. 10 the time of full melting of working agent with convection in the

liquid phase is somewhat lower than without. Under the above circumstances the time of full melting of agent in the former case is 78 min, and the latter case – 90 min. Said fact should be taken into account in the design of heat removal system in terms of increasing the amount of heat accumulator in a container when arranging REE element on its lower end surface.

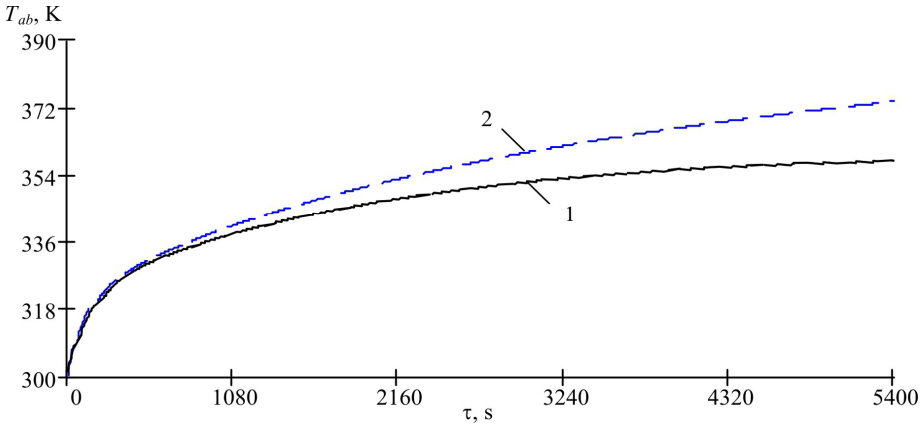

Fig. 9. Time dependence of jacket temperature upon melting of agent (paraffin) with (1) and without (2) liquid phase convection, $(c\rho\delta)_j = 2\cdot10^3$ J/(m^2·K) R = 0.025 m, $q_{REE} = 4000$ W/m^2.

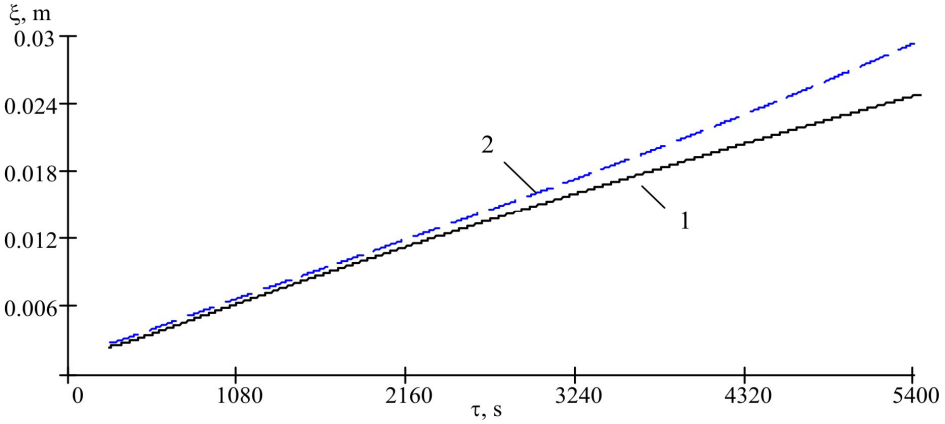

Fig. 10. Time dependence of phase interface coordinate upon melting of agent (paraffin) with (1) and without (2) liquid phase convection, $(c\rho\delta)_j = 2\cdot10^3$ J/(m^2·K), R = 0.025 m, $q_{REE} = 4000$ W/m^2.

Figs. 11 – 15 show dependences of jacket temperature from the side of a contact to thermopile and phase interface upon solidification of a filler for various values of thermopile cooling capacity, as well as for conditions when agent cooling and solidification is due to natural heat exchange with the environment. As can be seen from the plots, the time of cool down of working agent and device jacket with the use of a thermopile is several fold less than the time of their cool down with a natural heat exchange with the environment (for paraffin this ratio at $q_{THERMOPILE} = 2000$ W/m^2 and α_{amb}=10 W/(m^2·K) made 2 times). Hence it follows that the use of a thermopile relieves the existing restrictions to operating cycle duration of REE element and the duration of pause between its actuations. Therefore, whereas in case of natural heat exchange between cooling device jacket and the environment the operating period of REE element must have been considerably less than the "pause", with the use of a thermopile the time between two consecutive cycles of REE operation may be considerably reduced. In so doing, the quickest process of substance cooling and solidification

occurs with the use of paraffin and nickel nitrate as fillers (from Fig. 14 – 15, where studies were performed for paraffin, nickel nitrate, palmitinic and elaidic acides). The former is used due to the lowest temperature and melting heat, the latter – due to higher thermal conductivity coefficient.

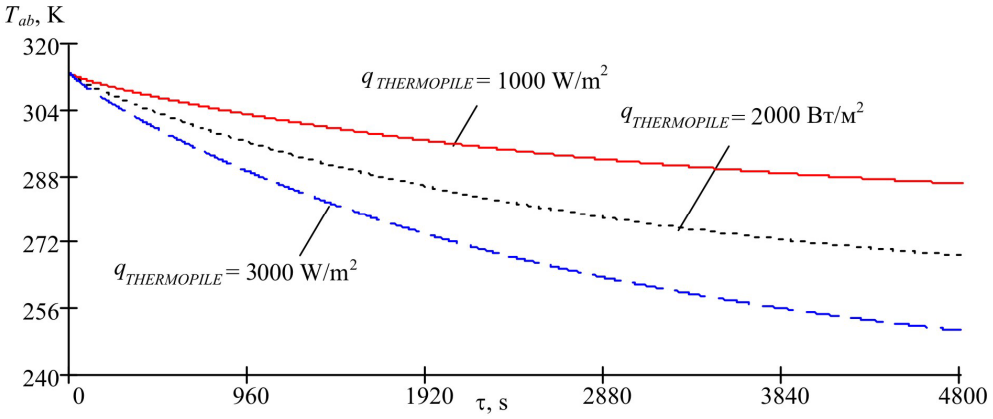

Fig. 12. Time dependence of phase interface coordinate upon solidification of agent (paraffin) $(c\rho\delta)_j = 6.5 \cdot 10^3$ J/(m^2·K); R = 0.025 m.

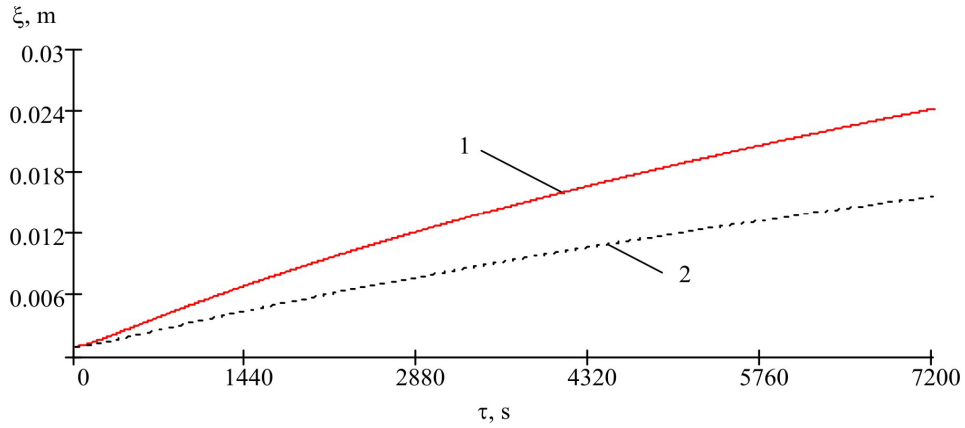

Fig. 13. Time dependence of phase interface coordinate upon solidification of agent (paraffin), $(c\rho\delta)_j = 6.5 \cdot 10^3$ J/(m^2·K); R = 0.025 m. 1 – with the use of thermopile with 2000 W/m^2 2 – with the use of natural air cooling due to heat exchange with environment (α_{amb} = 10 W/m^2·K).

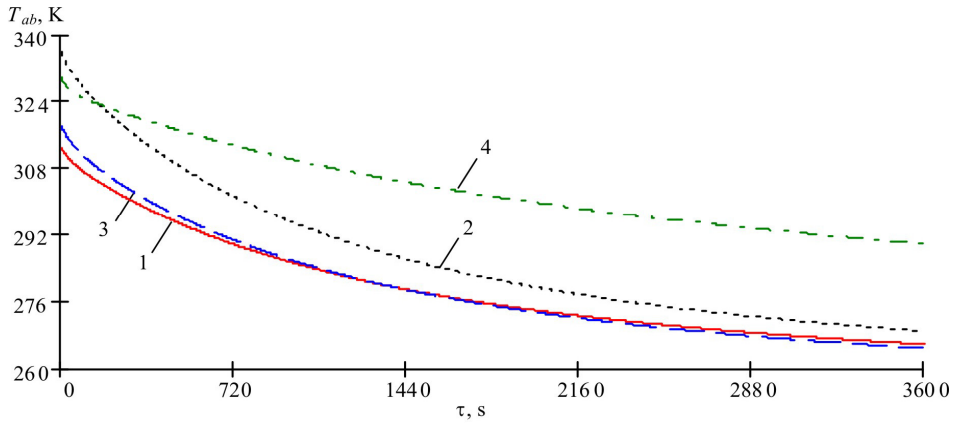

Fig. 14. Time dependence of jacket temperature upon solidification of various fillers, $(c\rho\delta)_j = 2.1 \cdot 10^3$ J/(m^2·K); R = 0.02 m, $q_{THERMOPILE}$ = 1500 W/m^2. 1 – paraffin, 2 – palmitinic acid, 3 – elaidic acid, 4 –nickel nitrate.

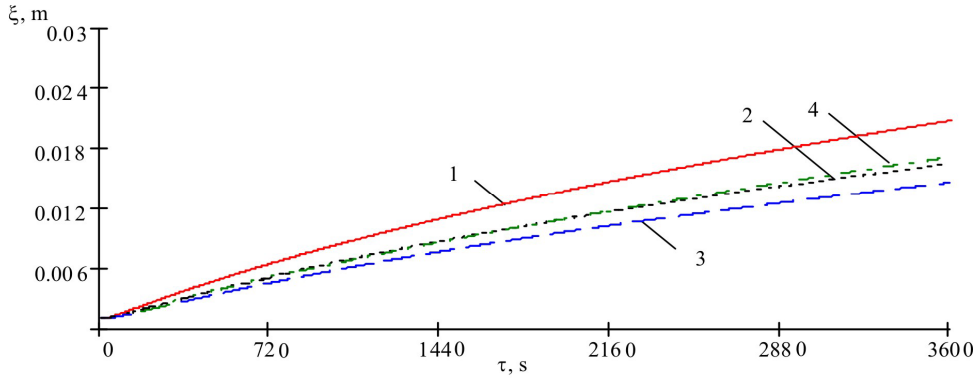

Fig. 15. Time dependence of phase interface coordinate upon solidification of various fillers, $(c\rho\delta)_j = 2.1\cdot10^3$ J/(m^2·K); R = 0.02 m, $q_{THERMOPILE} = 1500$ W/m^2. 1 – paraffin, 2 – palmitinic acid, 3 – elaidic acid, 4 – nickel nitrate.

The duration of agent solidification process can be reduced considerably with the use of the additional heat removal from the lateral surface of a container with the agent. According to calculated data (Fig. 1b), the use of the additional heat pickup with $q_{THERMOPILE} = 6000$ W/m^2 with the main $q_{THERMOPILE} = 1500$ W/m^2 will allow reducing the time of full solidification, for instance, for paraffin to 1200 s, nickel nitrate to 2000 s, palmitinic acid - to 2400 s. In so doing, in the case of the additional heat pickup from the lateral surface, when the values of thickness, length and width of sections with melting fillers are comparable, a direct calculation according to Eqs. (1) – (5), (6) – (10) is unacceptable. In this case, velocity addition principle is employed, which is stated, for instance, in [9].

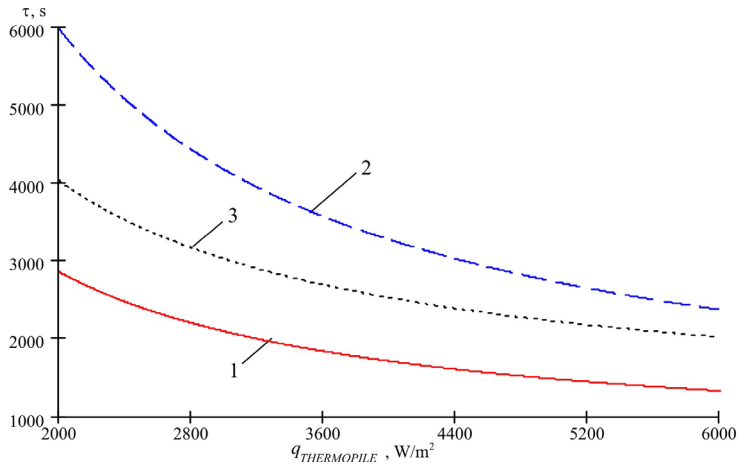

Fig.16. The time of full solidification of working agent with the use of the additional heat pickup from the lateral surface of a container versus thermopile power per unit area, $(c\rho\delta)_j = 2.5\cdot10^3$ J/(m^2·K); R = 0.02 m. 1 – paraffin, 2 – palmitinic acid, 3 – nickel nitrate.

According to this method, at first by means of one-dimensional solutions the thickness of working agent layer and the temperature of jacket in the directions of *x*, *y*, *z* are determined on condition that melting or solidification rates are independent of each other. Then the duration of melting or solidification of the whole mass in a container is calculated based on relationship

$$\frac{1}{\tau_n} = \frac{1}{\tau_x} + \frac{1}{\tau_y} + \frac{1}{\tau_z} \qquad (11)$$

where τ_n is duration of agent melting or solidification in a container; τ_x, τ_y, τ_z are durations of melting or
solidification in the direction of axes *x*, *y*, *z* in the absence of melting or solidification effect in the directions *y*, *z*; *x*, *z* and *x*, *y*, respectively.

By the known value of τ_n the temperature of device jacket is determined by means of one-dimensional solutions. As long as the influence of container size on the temperature of its jacket is less than on the thickness of melted layer, the resulting value of jacket temperature for a one-dimensional problem will allow estimating the limit temperature conditions of container jacket, hence, of cooled REE element.

Conclusions

As a result of investigations, the following conclusions can be made:

1. One of the efficient methods for heat removal from REE elements working in the intermittent heat release mode is a method based on the use of melting working agents. The main disadvantage of this method is a restriction related to the necessity of assuring melting process during the entire operation period of REE.
2. A cooling system for REE elements is proposed enabling one to expand the duration of their operation period due to the use of the additional heat removal from melting agents via a thermopile.
3. A mathematical model of cooling system is developed, realized by solving Stephan's problem with the use of Leybenzon' approximate method, the principle of which lies in selection of such functions of the liquid and solid phase temperature variation that would meet the initial and boundary conditions. The thus selected functions are substituted into phase matching condition, and the resulting differential equation is solved for phase interface coordinate.
4. As a result of solving the problem of melting (solidification) of agent, the time dependences of temperature variation of cooling system jacket, as well as phase interface coordinates were obtained. Said dependences strongly depend on heat scattering of REE element, the types of working fillers, thermopile cooling capacity, and the environmental conditions.
5. It was established that after 1.5 hours of REE element operation with a change in its scattering power
6. from 1000 to 3000 W/m^2 with the use of paraffin the jacket temperature is increased from 317 to 367 K, and melting rate – from 10^{-6} m/s to $3.7 \cdot 10^{-6}$ m/s.
7. The temperature of REE element while in operation is affected by selection of suitable working filler. The best agents in this respect will be those which, all other conditions being equal (melting temperature, melting heat, heat capacity, etc), have high values of thermal conductivity coefficient.
8. On of the methods for increasing the effective thermal conductivity coefficient can be the use in the working agent of various types of fillers (metal grit, various kinds of finning, porous structures).
9. On arrangement of REE element on the lower end surface of a container with working agent, melting process will be considerably affected by the presence of convective fluxes in its liquid phase. Under these conditions the temperature of REE element will be lower, but on the other hand the time of full melting of working agent will be reduced, which must be taken into account in the design of cooling system.

10. As a result of investigation of heat exchange at solidification of working agents it was established that the use of a thermopile reduces considerably the time of working agent solidification. For paraffin at $q_{THERMOPILE}$ = 2000 W/m^2 its value is almost half as much as in the case of natural heat exchange with the environment at α_{amb} = 10 W/(m^2·K).
11. For the intensification of the process of cooling and solidification of working agents it is worthwhile to realize heat pickup by the additional thermopiles arranged on the lateral surface of a container with working agent.
12. In the case of the additional heat pickup from the lateral surface, when the values of thickness, length and width of sections with melting fillers are comparable, a direct calculation according to Eqs. (1) – (5), (6) – (10) is unacceptable. In this case, velocity addition principle in conformity with Eq. (11) is employed.

References

1. L.I.Anatychuk, *Thermoelectricity. Thermoelectric Power Converters* (Kyiv, Chernivtsi: Institute of Thermoelectricity, 2003).
2. G.I.Dulnev, *Heat and Mass Exchange in Radioelectronic Equipment* (Moscow: Vysshaya Shkola, 1984).
3. V.Yu.Sushko, V.A.Korablev, and A.V.Sharkov, Method for Selection of Parameters of a Multilayer Protection of Electronic Device against Powerful Heat Effect, *Izvestia Vuzov. Priborostroyeniye* 49(3), (2006).
4. V.A.Alekseyev, V.F.Chukin, and A.V.Shishanov, Thermal Mode Prediction for Airborne Electronic Radio Equipment, *Systems Engineering* 2, (2004).
5. V.A.Alekseyev, *Cooling of Radioelectronic Equipment with the Use of Melting Substances* (Moscow, Energiya, 1975).
6. T.A.Ismailov, O.V.Yevdulov, M.M.Makhmudova, and D.V.Yevdulov, Research on Cooling System of Electronic Radio Equipment Elements Working in Intermittent Heat Release Mode, Izvestia Vuzov Rossii*, Radioelektronika* 5, (2008).
7. A.V.Lykov, *Theory of Thermal Conductivity* (Moscow: Vysshaya Shkola, 1967).
8. http://kryothermtec.com.
9. E.M.Goldfarb, *Heat Engineering of Metallurgical Processes* (Moscow: Metallurgiya, 1967).

Submitted 10.07.2015.

G. Gromov, S. Glyazer, Y. Zakhartsev

RMT Ltd, 46 Warshavskoe shosse, 115230, Moscow, Russia

THERMOELECTRIC HEAT FLUX SENSORS

Results of theoretical and experimental investigations of heat flux sensors based on the technology of thermoelectric micromodules are reported. Dependences of the main parameters of such sensors on the properties of thermoelectric materials and parameters of module design were investigated. On the basis of theoretical investigations a new method of self-calibrations of thermoelectric heat flux sensors using measurement of the module Figure-of-Merit Z and resistance ACR was developed. The technology of thermoelectric micromodules of the company RMT Ltd. allows designing miniature heat flux sensors with a wide range of performance parameters on demands of variety of applications. Advantages of thermoelectric heat flux sensors – high sensitivity, fast response, miniature design, variable performance parameters, scalability, and some others were confirmed.

Keywords: thermoelectric, module, heat, flux, sensor.

Introduction

Heat fluxes accompany most of physical-chemical transformations that occur in nature, industrial processes, as a result of human activity. Measurement of heat fluxes and temperature allows us to control these processes. Heat fluxes are measured by heat flux sensors [1]. Measurement of heat fluxes is required in various areas: scientific investigations, agriculture, climatology, building construction, solar energy, industrial applications, housing and communal services, safety and security, etc. Heat flux and temperature sensors occupy a significant niche in the market of modern sensors.

Units of heat flux and characteristics of sensors

The heat flux *Pe* is measured in Watts per unit of area *S* perpendicular to its direction – W/m^2. Or it is measured in units of total heat flux *P* – Watts. Heat flux sensors are also characterized by sensitivity to the heat flux, which is also measured in two types of corresponding units.

The sensitivity *Se* to heat flux density is the ratio of the electric signal *E* to the heat flux density *Pe*. The units are $\mu V/(W/m^2)$.

$$S_e = \frac{E}{P_e}. \tag{1}$$

The integral sensitivity *Sa* is the ratio of the electric signal to the total heat flux *P* incident on the sensor. The units are V/W.

$$S_a = \frac{E}{S \times P_e} = \frac{S_e}{S}. \tag{2}$$

The concept of the integral sensitivity makes heat flux sensors similar to photodetectors. It is true, because the radiation is also an energy flux. Heat flux sensors are used to measure thermal radiation.

State-of-the-Art heat flux sensors

The majority of the heat flux sensors are based on the method of "additional wall" [1]. The "additional wall" with a known thermal conductivity K is placed in the way of a heat flux P that is to be measured. The temperature gradient ΔT between the wall sides is proportional to the amount of the heat flux. The thermal resistance R_T of the wall is the reciprocal value of the thermal conductance K:

$$\Delta T = R_T \times P \,. \tag{3}$$

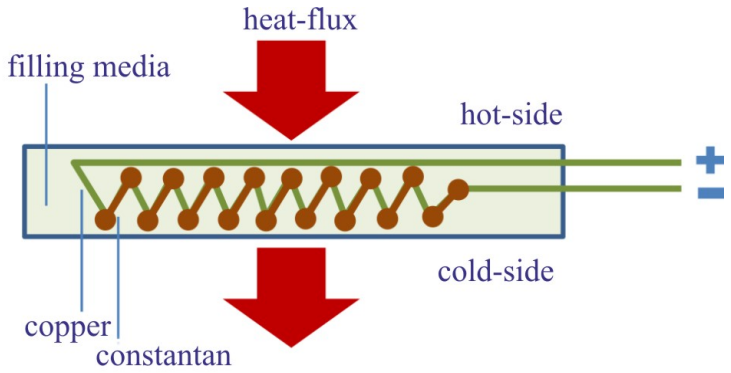

Fig.1 Schematic view of heat flux sensor of differential thermocouples.

Most of state-of-the-art heat flux sensors are made on the basis of differential thermocouples (Fig. 1) [2]. They involve the Seebeck effect in metals. Absolute values of electromotive force (the Seebeck coefficient) of metals are low - tens of μV/°C maximum. Therefore, series connection of many thermocouples is used to increase the sensitivity (Fig. 1) [3, 4]. The density of the thermocouples can reach up to 1000 – 2000 thermocouples per square centimeter. This assures multiple (of the number N of thermocouples) thermopower increase.

$$E = N \times \alpha \times \Delta T \,, \tag{4}$$

where α – the Seebeck coefficient of each thermocouple.

Thermoelectric heat flux sensors

In recent years, the interest in the use of thermoelectric modules as heat flux sensors has grown [5, 6]. Thermoelectric modules are widely used for cooling (the Peltier effect) or generation of energy (the Peltier and Seebeck effects). In heat flux sensors the thermoelectric effect – the Seebeck effect is also used, which is the physical basis for the differential thermocouple sensors, too. The construction of thermoelectric modules is similar to that of an array of thermocouples. Only here a "couple" is a pair of semiconductor thermoelements with different conductivity (*n*- and *p*-types), and in a thermocouple it is a junction of dissimilar metals. The Seebeck effect in semiconductors is many times higher than in metals. For example, in a copper-constantan thermocouple the Seebeck coefficient of a couple is about 38 μV/°C. In a thermoelectric module for one *p*-*n* pair it is more than 400 μV/°C.

While thermoelectric modules have long been used as generators and coolers, this advantage for the sensors applications has not been realized for a long time. The key reason is a low degree of integration of thermoelements. For a long time it was at the level of 100 – 150 pellets per 1 cm^2. With such a low elements density, thermoelectric modules used as heat flux sensors are inferior to

arrays of differential thermocouples [4]. However, the modern trend to miniaturization of thermoelectric modules (Fig. 2), mainly because of the needs of optoelectronics, where thermoelectric cooling is widely used, has led to significant progress in the construction of thermoelectric micromodules – extremely miniature design and dense packing.

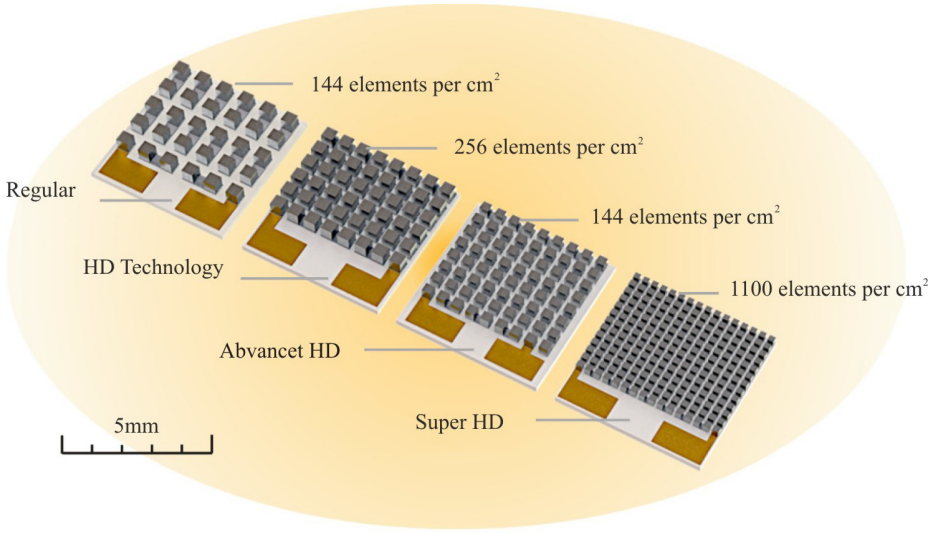

Fig. 2. Advances in miniaturization of thermoelectric modules - example of RMT micromodules technology development.

Advanced thermoelectric micromodules are comparable with sensors based on differential thermocouples in dimensions and dense integration, which enables us to use them as heat flux sensors. Miniature and high-density packaged modules are manufactured by two technologies: thin film (new) and bulk (conventional) technology (Fig. 3).

Each technology has its advantages and limits of use, but both provide the ability to produce miniature modules undreamed of quite recently (down to the level of 1 mm^2 and less) and high density of their packing.

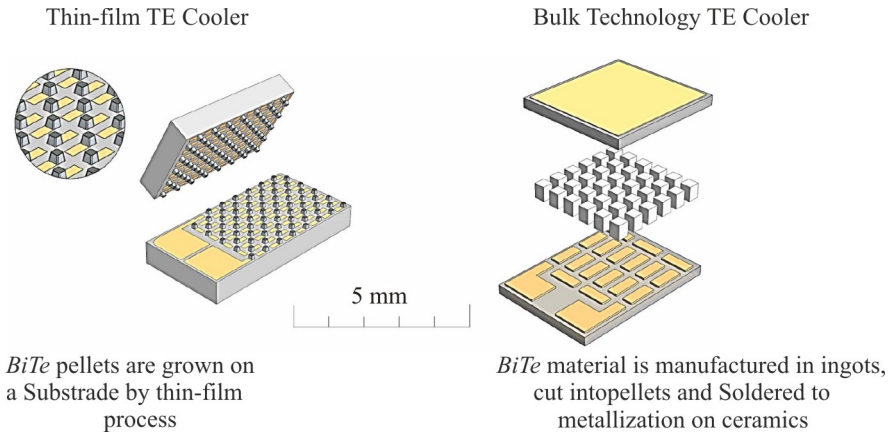

Fig. 3 Comparison of designs of thermoelectric modules: thin-film and bulk.

Parameters of thermoelectric heat flux sensors

Integral sensitivity *Sa*

The electrical signal E of the thermoelectric heat flux sensor is the following.

$$E = 2N \times a \times \Delta T, \tag{5}$$

where α – the average Seebeck coefficient for a *p-n* pair; $2N$ – the number of thermoelements.

Where at given ΔT (3) the absolute sensitivity sensor *Sa*

$$E = 2N \times a \times \Delta T . \tag{5}$$

In the ideal case (heat flows only through the thermoelements):

$$R_T = \frac{1}{K_T} = \frac{1}{2N \times k \times \frac{s}{h}}, \tag{7}$$

where K_T – thermal conductance of the sensor; k – the average thermal conductivity for thermoelement; $\frac{s}{h}$ – ratio of cross-section (s) of the element to its height (h), which is the form factor (f) of a thermoelement.

Thus, the sensor sensitivity

$$S_a = \frac{1}{f} \times \frac{\alpha}{k} . \tag{8}$$

The thermoelectric heat flux sensor sensitivity is determined by the ratio of the Seebeck coefficient α to thermal conductivity k and is inversely proportional to the form factor f of the thermoelement (pellet). The important consequence of expression (8): the sensitivity does not depend on the number of the thermoelements in the sensor. The inverse proportionality to the thermoelement's form factor works instead. The sensitivity can be increased by smaller cross-sections of thermoelements at a relatively large height.

Sensitivity *Se*

The sensitivity *Se* to the density of heat flux is derived from the integral sensitivity *Sa*, if you multiply it by the area of the sensitive surface of the sensor *S* (2).

Thermal Resistance R_T

The value of the thermal resistance of the thermoelectric heat flux sensor is crucial. On the one hand it is the thermal resistance that gives a temperature difference (3) which causes the signal. High thermal resistance means high sensitivity of the sensor. On the other hand the effect of the presence of the measuring sensor (the "additional wall"), i.e. its thermal resistance, should be preferably minimized.

Time constant τ

The expression of the time constant of thermoelectric microcoolers is applicable for such heat flux sensors, too:

$$\tau = \frac{C_c}{f \times k \times 2N}, \tag{9}$$

where *Cc* – heat capacity of side of thermoelectric module or the sensor cover.

Calibration method of thermoelectric heat flux sensors

The sensor calibration is required to ensure the high accuracy for applications. The calibration allows getting the coefficient of the output signal proportionality to the heat flux. For the calibration two methods are known.

One method is to use an external heat flux reference source [7, 8]. This calibration is carried out with the use of special equipment and in the laboratory. It is available only in periodical maintenance of the sensor. So it is time-consuming, expensive and limited in application.

Another method is to embed a reference heat source into the sensor [9, 10]. For example, it is a vacuum deposition of a resistive heater to one of the sensor side [10]. When electric power is applied to the embedded heater, it produces the heat of a known value. It results in a signal of the sensor. With this calibration method the sensor is called self-calibrating. It is possible to calibrate it at any time without external hardware. The downside is that the reference heat source should be integrated in the sensor. This complicates the design and production costs.

Thermoelectric modules have long been widely used for cooling and power generation. In these applications a number of measurement parameters of the modules are used to determine their quality and performance properties. These parameters are: thermoelectric Figure-of-Merit Z, internal electrical resistance ACR and, less commonly, time constant τ. The use of these parameters to specify the basic properties of thermoelectric heat flux sensors is also attractive.

The formula for the sensitivity (6) shows its dependence on the ratio $a \times R_T$. It is possible to express it by the parameters Z and ACR of a thermoelectric module.

$$Z = \frac{(2N \times a)^2 \times R_T}{ACR}. \tag{10}$$

Thus

$$\alpha \times R_T = \frac{1}{(2N)^2 \times a} Z \times ACR. \tag{11}$$

Then equation (6) is finally converted to the following

$$S_a = \frac{1}{a \times 2N} Z \times ACR. \tag{12}$$

Formula (12) is a basis of the new method of calibrating of the thermoelectric heat flux sensors. The design of a thermoelectric module (the number of pellets is $2N$) is known in advance. The Seebeck coefficient of thermoelectric material α used for manufacturing of sensors can be controlled. At a given area of the sensitive surface S, the number of the thermoelements in the sensors $2N$ and known Seebeck coefficient of the thermoelectric material α, it is easy to determine the sensitivity (Sa and Se) by equations (12) and (2) respectively, by measuring the thermoelectric Figure-of-Merit Z and the resistance ACR of the sensor.

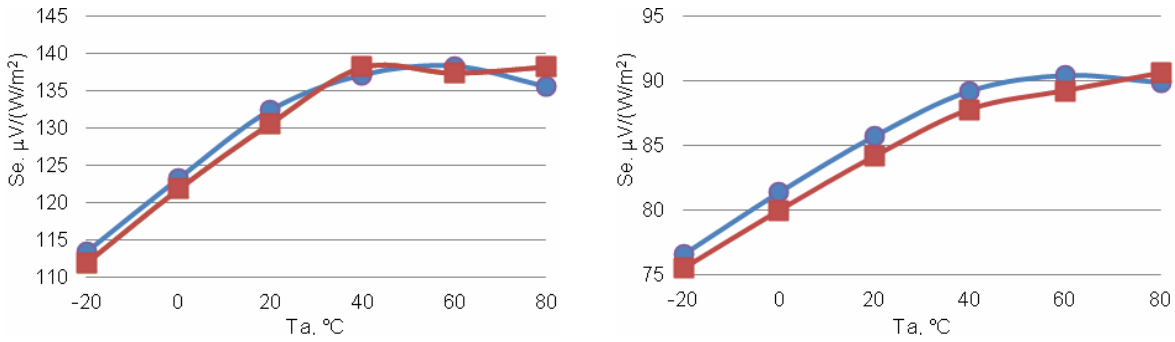

Sample 1 *Sample 2*

Fig. 4. Comparison of calibrations by the method with external heat flux reference source (red) and the proposed method (blue) in a range of ambient temperatures Ta.

The calibration by the new method is no more than 2% different from the results of the calibration with a reference source (Fig. 4). This is a good result for the practical use of the new method. It does not require applying reference thermal sources, does not need maintenance of sensors for the calibration procedure, and can be performed with any periodicity in a field.

Optimal design of RMT heat flux sensors

As seen from expressions (8), (2), the key parameters of thermoelectric heat flux sensors depend on the design features:

- properties of thermoelectric material – α, k.
- design parameters of thermoelectric module and its thermoelements – f.
- sensitive surface area S.

RMT technology allows producing miniature thermoelectric modules in wide ranges of dimensions, degree of miniaturization, thermoelements form-factors, etc. (Fig. 2). This makes it possible to develop both individual sensors and their series optimized for different applications. This practice is applied by the company in the design and manufacture of micromodules for cooling and generation. The approach is applicable to the heat flux sensors.

Properties of thermoelectric material

The properties of thermoelectric material are specified by its manufacturing technology. These parameters can hardly be varied significantly for the optimization of sensors. The only important thing is to select material with a maximum Seebeck coefficient α, typically at the level of the average values of 200 – 240 μV/K.

Thermoelectric module design

The design parameters of thermoelectric module can be controlled. RMT technologies allow producing modules of pellets in wide ranges of cross-sections and heights, packing densities and elements numbers (Fig. 2).

Form factor of thermoelements

The dependence of the sensitivity Sa of thermoelectric heat flux sensors on form factor (8) is shown in Fig. 5. The Table 1 shows the values of the form-factor of pellets of RMT thermoelectric modules. Respectively, in Fig. 5 the available range of sensitivities of heat flux sensors based on RMT modules is marked by color.

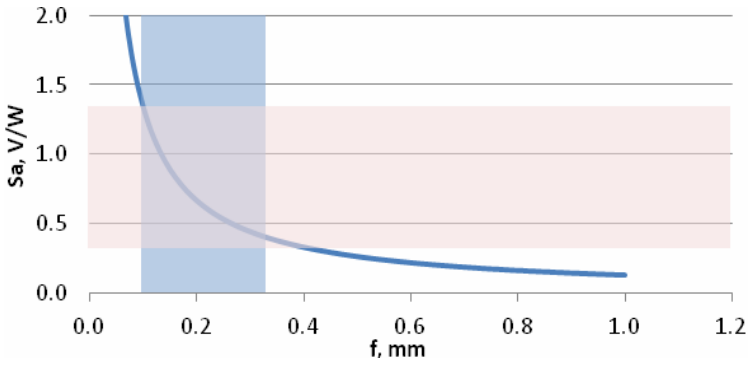

Fig. 5. Dependence of thermoelectric heat flux sensor sensitivity on the pellet form factor.

Table

Value of form-factors of the thermoelectric pellets of RMT

Height *h*, mm	*f*, mm (at given cross-section *axb*)		
	0.2 × 0.2 mm^2	0.3 × 0.3 mm^2	0.4 × 0.4 mm^2
0.3	0.133	-	-
0.4	0.100	0.225	-
0.5	0.080	0.180	0.320
0.8	-	0.113	0.200
1.0	-	-	0.160
1.2	-	-	0.133
1.5	-	-	0.107

Height of thermoelements

From expression (5) and determination of form-factor it follows that at a given value of thermoelement cross-section *axb* the sensor sensitivity will increase with the growth of the thermoelement height. However, with increasing the thermoelement height, the sensor time constant will also grow in conformity with (9). Therefore, obtaining the highly sensitive sensor together with high-speed performance is the optimization task for particular applications (Fig. 6).

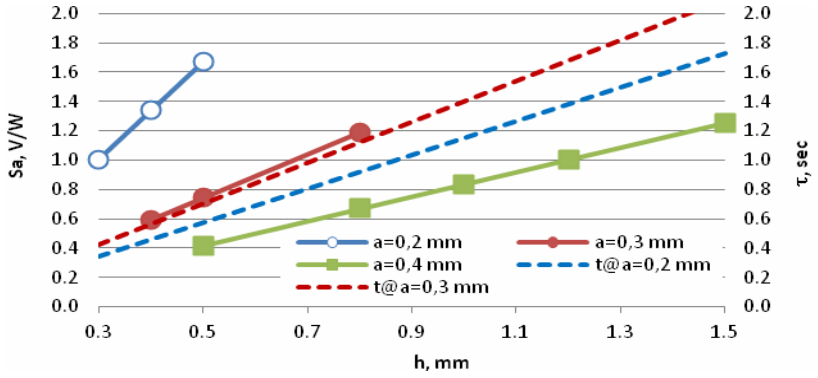

Fig. 6. Estimated dependences of the sensitivity Sa and the time constant τ of the sensor on thermoelements height h for their different widths: 0.2; 0.3 and 0.4 mm.

The most fast and sensitive sensors have thermocouples with a minimum cross-section 0.2 mm. A high sensitivity is attainable for large elements cross-sections, but this reduces performance due to larger thermoelement height of such sensors.

Sensor dimensions

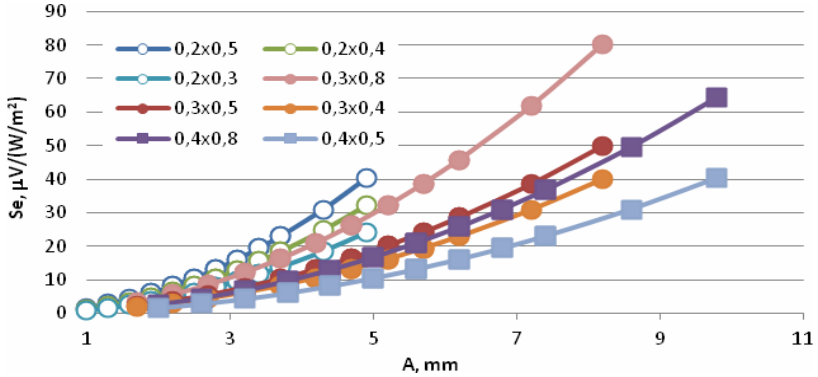

Fig. 7. Dependence of sensitivity of thermoelectric sensors Se on their linear size A.

The sensitivity to heat flux density *Se* depends on the heat absorption side area of the sensor (2). The thermoelectric module size is determined by the number of elements, their cross-section and density of packing.

Experimental family of heat flux sensors

Based on the above analysis the experimental family of heat flux sensors consisting of three subseries was developed in RMT.

HTX heat flux and temperature sensors (HT – Heat flux & Temperature). The sensors contain thermoelectric heat flux sensor and embedded Pt1000 thermistor. They have a round shape, external aluminum sides with black finish. The sensors are potted by a silicone compound.

HFX heat flux sensors without temperature (HF – Heat Flux). Their features are a square shape, external sides AlN ceramics with black paint finish. The sensors are potted by a silicone compound.

HRX sensors IR radiative heat flux (HR – Heat flux Radiation). These are miniature thermoelectric heat flux sensors. They are made as SMD style components suitable for flip-chip mounting. They have a square shape, and external sides of AlN ceramics. The radiation absorption surface has a black finish with high emissivity.

Comparison of heat flux sensors

In Fig. 8 the sensitivity of the heat flux sensors of RMT experimental family is compared with the sensitivity of heat flux sensors of well-known manufacturers at the market.

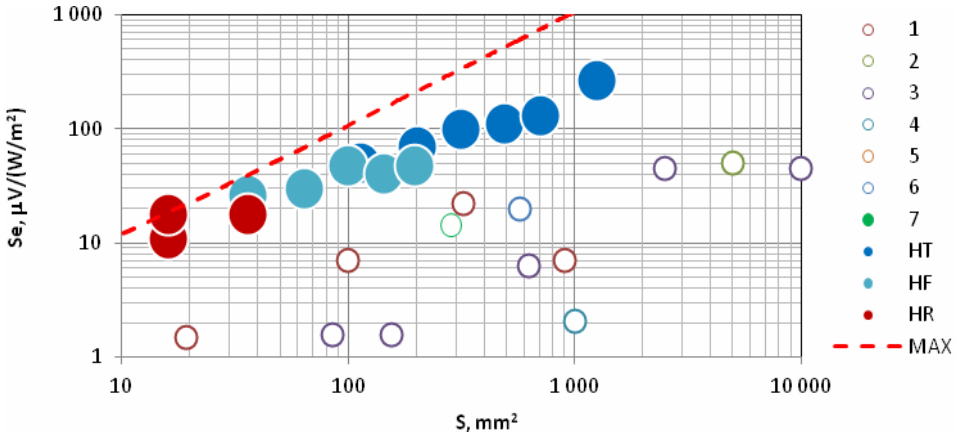

Fig. 8 Sensitivity Se of heat flux sensors of different producers (1 - 7) and experimental series of RMT (HT, HF, HR), depending on the sensor area. Dotted line – maximum available sensitivity of RMT technology.

The sensors of the developed experimental series have significant advantages over heat flux sensors that are present at the market now:

1) Sensitivity is significantly higher than that for the sensors based on differential thermocouples.
2) Miniature design due to a high packing density of elements in thermoelectric micromodules.
3) Variable thermal resistance due to the flexibility in the design of the micromodules.
4) High-speed performance.

The conclusions

1. Thermoelectric micromodules have three major areas of the market and applications perspectives: cooling, generation and heat flux sensors.
2. The Seebeck effect in semiconductors is considerably higher than that in metals. This makes the use of thermoelectric micromodules heat flux sensors promising, able to compete with the differential thermocouple sensors.
3. The sensitivity does not depend on the number of thermoelements. It is determined by the ratio of the Seebeck coefficient and thermal conductivity and is inversely proportional to the form factor of the thermoelement.
4. The highly accurate self-calibration method of thermoelectric heat flux sensors by *Z* and ACR does not require the use of reference thermal sources or maintenance of sensors for the calibration procedure and can be performed with any periodicity.

References

1. T.E. Diller, Heat Flux (Copyright 2000 CRC Press LLC).
2. D.J. Ortolano, F. F. Hines, Advances in Instrumentation 38, Part II, 1449 – 1456(1983).
3. J. M. Hager, S. Onishi, L.W. Langley, and T.E. Diller, AIAA J. Thermophysics Heat Transfer 7, 531 – 534 (1993).
4. J.P. Terrell, Proc. 42nd Int. Instrum. Symp. (Research Triangle Park, NC: ISA, 1996, 235 – 249).
5. T. Leephakpreeda, ISA Transactions 51, 345 – 350 (2012).
6. C. McKinnon, R.R. Bernardini, W. Thresher. S.L. Ruis, and D.W. Yarbrough, Ecolibrium 32 – 36 (May 2010).
7. United States Patent 4812050, Method for Calibrating a Heat Flux Gauge, 1987
8. ASTM C177 – 13. Standard Test Method for Steady-State Heat Flux Measurements and Thermal Transmission Properties by Means of the Guarded-Hot-Plate Apparatus.
9. United States Patent 3599474, Self-Calibrating Heat Flux Transducer, 1969.
10. HFP01SC, Self-Calibrating Heat Flux Sensor (Version 1003. Hukseflux. Page 1). http://www.hukseflux.com/sites/default/files/product_brochure/HFP01SC%20v1003.pdf

Submitted 22.12.2015.

ARTICLE PREPARATION RULES

The article shall conform to the journal profile. The article content shall be legible, concise and have no repetitions.

The article shall be submitted to the editorial board in electronic version.

The text shall be typed in text editor not lower than MS Word 6.0/7.0.

Page setup: "mirror margins"- top margin – 2.5 cm, bottom margin – 2.0 cm, inside – 2.0 cm, outside– 3.0 cm, from the edge to page header – 1.27 cm, page footer – 1.27 cm.

Graphic materials, pictures shall be submitted in color or, as an exception, black and white, in .opj or .cdr formats, .jpg or .tif formats being also permissible. According to author's choice, the tables and partially the text can be also in color.

The article shall be submitted in English on A4 paper sheets; the number of pages shall not exceed 12. By agreement with the editorial board, the number of pages can be increased.

To accelerate publication of the article, please adhere to the following rules:

- the authors' initials and names are arranged in the centre of the first page at the distance of 1 cm from the page header, font Times New Roman, size 12 pt, line spacing 1.2;
- the name of organization, address (street, city, postal code, country) – indent 1 cm below the authors' initials and names, font Times New Roman, size 11 pt, line spacing 1.2, center alignment;
- the title of the article is arranged 1 cm below the name of organization, in capital letters, semi-bold, font New Roman, size 12 pt, line spacing 1.2, center alignment. The title of the article shall be concrete and possibly concise;
- the abstract is arranged 1 cm below the title of the article, font Times New Roman, size 10 pt, in italics, line spacing 1.2 ,center alignment;
- key words are arranged below the abstract, font Times New Roman, size 10 pt, line spacing 1.2, justified alignment. The title "Key words" – font Times New Roman, size 10 pt, semi-bold;
- the main text of the article is arranged 1 cm below the abstract, indent 1 cm, font Times New Roman. size 11 pt, line spacing 1.2, justified alignment;
- formulae are typed in formula editor, fonts Symbol, Times New Roman. Font size is "normal" – 12 pt, "large index" – 7 pt, "small index" – 5 pt, "large symbol" – 18 pt, "small symbol" – 12 pt). The formula is arranged in the text, centre aligned and shall not occupy more than 5/6 of the line width, formulae are numbered in round brackets right;
- dimensions of all quantities used in the article are represented in the International System of Units (SI) with the explication of the symbols employed;
- figures are arranged in the text. The figures and pictures shall be clear and contrast; the plot axes – parallel to sheet edges, thus eliminating possible displacement of angles in scaling;
- tables are arranged in the text. The width of the table shall be 1 cm less than the line width. Above the table its ordinary number is indicated, right alignment. Continuous table numbering throughout the text. The title of the table is arranged below its number, center alignment;
- references should appear at the end of the manuscript. References within the text should be enclosed in square brackets. References should be numbered in order of first appearance in the text. Examples of various reference types are given below.

– L.I. Anatychuk, *Thermoelements and Thermoelectric Devices: Handbook* (Kyiv: Naukova Dumka, 1979), p.766. (Book)
– T.M. Tritt, Thermoelectric Phenomena, Materials, and Applications, *Annual Review of Materials Research* **41**, 433 (2011). (Journal paper)
– U. Ghoshal, *Proceedings of the XXI International Conference on Thermoelectrics* (N.Y., USA, 2002), p. 540. (Proceedings Conference)

The article should be supplemented by:

• letter from the organization where the work was performed or from the authors of the work applying for the publication of the article;

• information on the author (authors): last name and initials; full name and postal address of the institution where the author works; academic degree; position; telephone number; E-mail;

• author's (authors') photo in color or, as an exception, in black and white. With the number of authors more than two their photos are not given;

• author's application to the following effect:

We, the undersigned authors, … transfer to the founders and editors of "Journal of Thermoelectricity" the right to publish the article…in Ukrainian, Russian and English. This is to confirm that the present publication does not violate the copyright of other persons or organizations.

Date Signatures